RESISTIVE SWITCHING IN TiO_2 FOR MEMORY APPLICATIONS

DU YUANMIN

NATIONAL UNIVERSITY OF SINGAPORE

2013

RESISTIVE SWITCHING IN TiO_2 FOR MEMORY APPLICATIONS

DU YUANMIN

(BSc. Nanjing University)

A DISSERTATION SUBMITTED IN PARTIAL FULFILLMENT OF THE REQUIREMENTS FOR THE DEGREE OF DOCTOR OF PHILOSOPHY TO THE DEPARTMENT OF PHYSICS OF THE NATIONAL UNIVERSITY OF SINGAPORE

Acknowledgements

In the first place, I would like to thank my advisor Prof. Andrew Thye Shen Wee for his supervision and guidance of this research. His advice and encouragement showed me paths to many problems I confronted in the research. He provided me support in various ways and gave me the freedom to explore different ideas of research. It has been a great life experience to study under his guidance.

I would like to thank my co-advisor Dr. Shijie Wang for his guidance and support throughout the work. He taught me many about the research, and also shared his insight and humor during these years. His enthusiasm to work inspired me in my research.

I would also show my appreciation to my co-advisor Dr. Hui Pan for his advice and support to my research. He not only taught me about first-principles calculations but also shared his wisdom in research and life. I am truly grateful for all the help and encouragement he has given to me in the work.

Special thanks to Dr. Zheng Zhang, Mr. Liang Cao, Dr. Sheh Lit Chang, Dr. Amit Kumar, Dr. Ping Yang, Dr. Jisheng Pan, Mr. Haiyang Peng, Dr. Tom Wu, Prof. Kaiyang Zeng and Prof. Yuanping Feng for their supports in my experiments, and also for their valuable discussions and suggestions.

I acknowledge the National University of Singapore-Nanoscience and Nanotechnology Initiative for the research scholarship, which enables me to conduct my research and finish this thesis.

Finally, I would like to express my deep appreciation to my parents for their unselfish love and support throughout my life. I also would like to thank to my wife, Yan Liu, for her endless love and consistent support.

Abstract

With the rapid advances in information technology, FET (Field Effect Transistor) based semiconductor electronics face a number of fundamental and practical issues. In terms of nonvolatile memory, it is expected that conventional memory scaling will approach both technical and physical limits in the near future. As a result, new functional devices are being explored to advance the development of memory technology. One emerging non-volatile memory is the resistance random access memory (RRAM). Due to its simple structure, low operating power, high switching speed and compatibility with conventional CMOS (Complementary Metal-Oxide-Semiconductor) processes, RRAM has attracted significant attention in recent years, and is considered as a promising candidate for the next generation non-volatile memory device.

Resistive switching refers to the electrically stimulated change of resistance under the action of an electrical field or current. Among many resistance switching materials, TiO_2 has drawn widespread attention. Studies into TiO_2 have greatly helped understanding of resistive switching mechanisms, as well as the development of RRAM technology. However, there are many unsolved issues on the switching mechanism. As the system is complex, there are many experimental and theoretical challenges in exploring the underlying mechanisms.

It has been proposed that the resistance switching mechanisms can be categorized into the filamentary type and the interfacial type. Both types of mechanisms have been reported in different material systems. In this dissertation, we propose an integrated model, and perform supporting experimental and theoretical studies. The main experimental techniques include conductive atomic force microscopy (CAFM), Kelvin probe force microscopy (KPFM), current-voltage (I-V) measurements,

ultraviolet photoelectron spectroscopy (UPS) and x-ray photoelectron spectroscopy (XPS). First-principles calculations based on density functional theory (DFT) are used for theoretical modeling.

In many reports, the oxide between the two electrodes is strongly insulating and an initial electroforming process comprising of a high electrical field soft breakdown is needed to the virgin sample. In this study, we focus on the deposition of TiO_2 thin films with enhanced conductivity, and investigate the underlying resistive switching mechanism. We report the observation of high density filaments in the oxide thin films, which shows good potential for RRAM device scaling. Multiple filamentary characteristics and their switching mechanisms are investigated.

Negative differential resistance (NDR) behavior is sometimes observed in resistive switching. We report the observation of symmetrical NDR characteristic with high repeatability in a switching device. Based on first-principles modeling and experimental measurements, we propose a new understanding of the Simmons and Verderber (SV) mechanism for charge storage, incorporating oxygen molecular ions into the model. We further extend the SV mechanism to a filament-interface model system.

List of Figures

Chapter 1

Introduction

1.1 Background

Over the last decades, the semiconductor industry has experienced rapid technological change and declining costs of final products. This improvement is primarily achieved by means of the scaling of semiconductor devices to smaller and smaller dimensions. Named after Intel co-founder Gordon E. Moore, Moore's law postulates that the number of components on integrated circuits doubles

approximately every eighteen months [1]. This trend has continued for more than half a century. However, as the FET (field effect transistor) size enters the sub 100 nm regime, the continued success of semiconductor devices now faces a number of fundamental and practical issues. In terms of memory applications, the transistor based Flash memory will face technical and physical limits in the near future, based on the projections of the International Technology Roadmap of Semiconductors (ITRS) [2]. To overcome this problem, new memory technologies introducing new materials and/or structures are needed.

Non-FET based devices and architectures which do not suffer the same problems associated with transistor scaling have become to emerge. The ideal nonvolatile memory (NVM) should have high density, low cost, low energy consumption and high performances for potential applications. Different types of non-volatile memory devices such as Ferroelectric RAM (FeRAM) [3], which uses electrical polarization in a ferroelectric layer, Magneto-resistive RAM (MRAM) [4], which uses resistance changes in magnetic tunnel junctions, phase change RAM (PCRAM) [5], in which thermal processes control a phase transition between crystalline and amorphous states of a chalcogenide compound, have been proposed. Unfortunately, none of the above approaches satisfy the requirements as an ideal NVM candidate. For example, even though FeRAM and MRAM use much less power and switch significantly faster (< 20 ns) than a Flash memory, these devices are large (>> 10 F^2, where F is the smallest feature size in the device structure) and expensive. For PCRAM, the fast switching time and inherent scalability makes it appealing. Nevertheless, the fact that phase-change is a thermally driven process rather than an electronic process raises the challenge of long-time resistance and threshold voltage drift. Furthermore, the volume

effect during a phase change may cause significant contact issues in ultimately scaled devices.

In this chapter, we will discuss another type of NVM device – resistive random access memory (RRAM) [6-12], which is a potential front-runner in future memory applications. During the last decades, RRAM has received increasing interest from both academia and industry.

1.2 Resistive random access memory (RRAM)

The RRAM memory cell has a capacitor structure with the switching medium sandwiched between two terminal electrodes (Fig 1.1). The resistance change of the switching medium can be achieved by current or voltage pulse applied to the electrodes. Starting in the 1960's [13-15], various materials in a metal-insulator-metal (MIM) structure have been reported to show resistance switching.

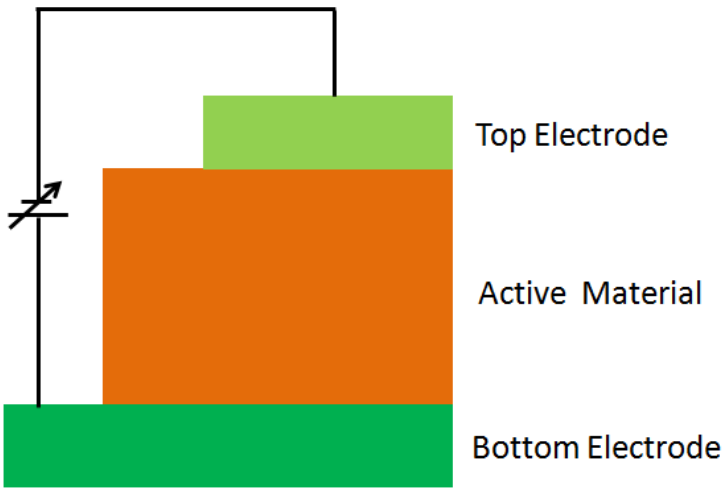

Figure 1.1: Diagram of a two terminal RRAM memory cell. The switching medium sandwiched between the two electrodes determines the resistance state of the device.

Resistance switching typically exhibits a hysteretic current-voltage characteristic with a change in resistance between a low resistance state (LRS) and a high resistance state (HRS). The switching process from HRS to LRS is achieved by the set operation,

whereas the reverse transition is obtained by the reset operation. In general, the operation of resistance switching can be divided into two different schemes depending on the electrical polarity, as shown in Fig 1.2.

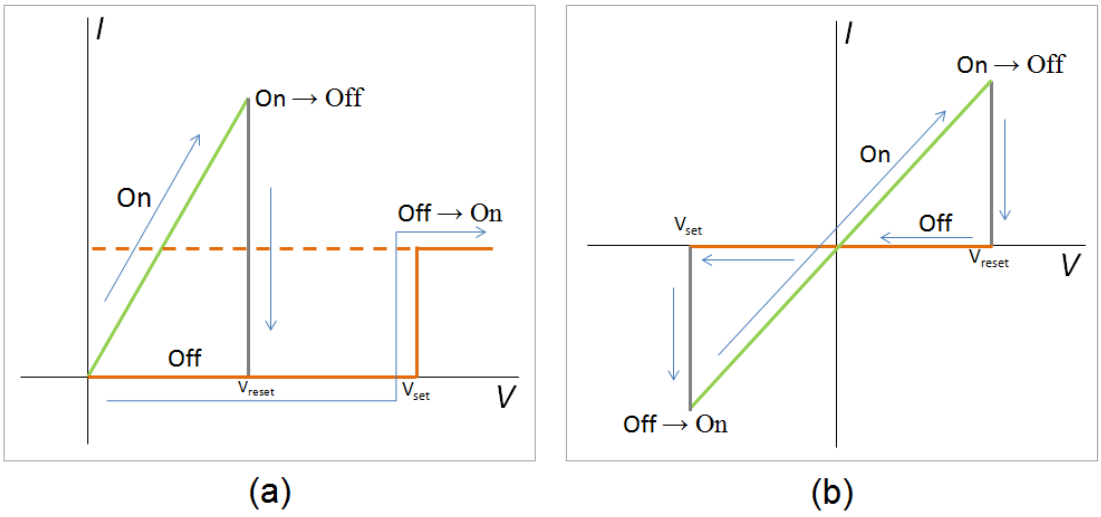

Figure 1.2: Schematic diagram of two types of resistance switching modes. (a) unipolar switching, and (b) bipolar switching.

When both set and reset switching take place at the same polarity of voltage (or current), the switching behavior is called unipolar switching (Fig 1.2(a)). The switching only depends on the magnitude of the applied bias. In the set process, a current compliance is required. The set switching is achieved by applying a threshold voltage that is larger than the reset voltage.

In the case of the bipolar switching, the resistance switching depends on the polarity and magnitude of the applied bias. Fig 1.2(b) shows a clockwise type switching, that is, the set switching is achieved by a negative voltage while the reset by a positive voltage. In contrast to clockwise switching, counter clockwise type switching requires a positive set voltage and a negative reset voltage. Both types of bipolar switching can be observed in the same material system [16, 17].

Once the RRAM memory cell is set to a specific resistance state, the device can retain the information for a certain period, which is termed the retention time. The resistance state is read out at a small voltage. RRAM can operate at a time scale less than 10 ns, and the data storage can be kept more than 10 years [9]. Its ability to run at lower voltages suggests the energy consumption can be significantly reduced. Furthermore, RRAM has a simple two-terminal MIM structure, which allows the use of crossbar memory architecture. As a result, RRAM has emerged as one of the most promising candidates for next generation memory technologies.

1.3 The resistance switching mechanisms

One of the most challenging issues in the development of RRAM is that the resistive switching mechanism is still a matter of debate [8-10]. Since the first report by Hickmott in 1962 [13], the resistive switching phenomenon has been reported in a wide variety of materials. Up to now, different models have been reported. This uncertainty comes from the difficulty in characterizing the physical changes responsible for a switching process. Conceivable mechanisms for resistive switching could come from a physical effect such as a thermal effect and an electronic effect, or a chemical effect, or a combination of both.

Different mechanisms could be dominant in different materials systems. It is also possible that several different mechanisms may co-exist in the same system. In this section, several important models proposed for resistive switching will be discussed.

1.3.1 The ECM effect

The electrochemical metallization (ECM) effect is induced by electrochemical metallization and dissolution in a solid electrolyte system [9]. The ECM memory cell consists of one electrode from an electrochemically active metal such as Ag, Cu and

Hg, a counter electrode from a noble metal such as Pt, Au and W, and a thin film of a solid electrolyte sandwiched between two metal electrodes [18-21]. A typical resistive switching process is demonstrated in Fig 1.3. The electrolytes normally have a high resistance initially and exist in an insulating state (Fig 1.3(a)). When a positive voltage is applied to the active electrode, the electrochemically active metal is oxidized at the interface, and the process can be described as $M \rightarrow M^{z+} + ze^{-}$, where M^{z+} represents the metal ion. The mobile metal ions migrate through the electrolyte layer toward the electrochemically inert electrode and are reduced there ($M^{z+} + ze^{-} \rightarrow M$). The protrusion of metal ions results into a conductive filament formed within the electrolyte, and switches the device to an ON state. When a negative voltage is applied to the active electrode, electrochemical dissolution takes place at the edge of the metal filament and eventually breaks the filament, and the device is reset into an OFF state.

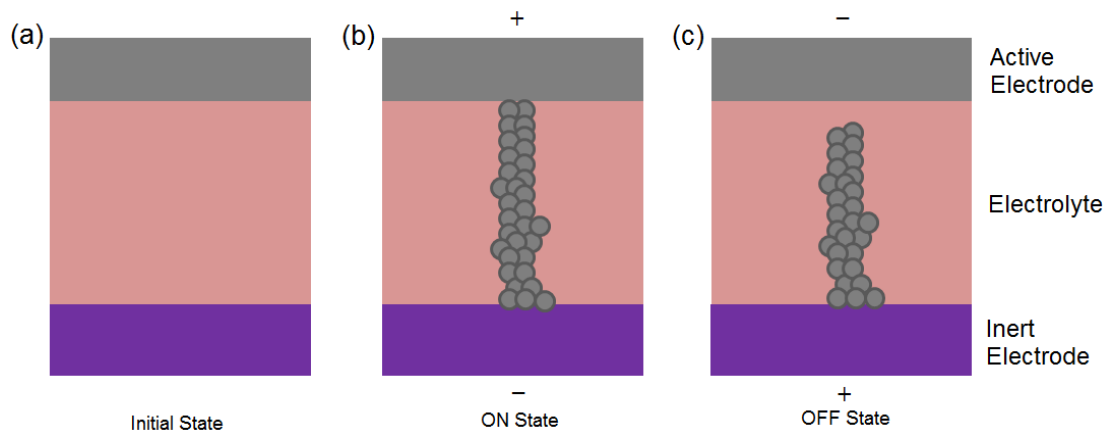

Figure 1.3: A schematic diagram for mechanism of resistive switching in ECM cells. (a) The electrolyte is initially in an insulating state; (b) Migration of active metal atoms forms a highly conductive filament in the cell; (c) Change of the polarity of the applied voltage results into an electrochemical dissolution of the filament.

The ECM memory systems are widely reported in selenides and sulphides, as well as in some oxides. It is difficult to observe the growth of filament(s) in a vertical

system. Fig 1.4 shows the formation of a Ag dendrite filament in a lateral system Ag/Ag-As_2S_3/Au [20]. The silver dendrite filament bridges the two electrodes and reduces the resistance dramatically. Rupture of the filament switches the system to a high resistance state.

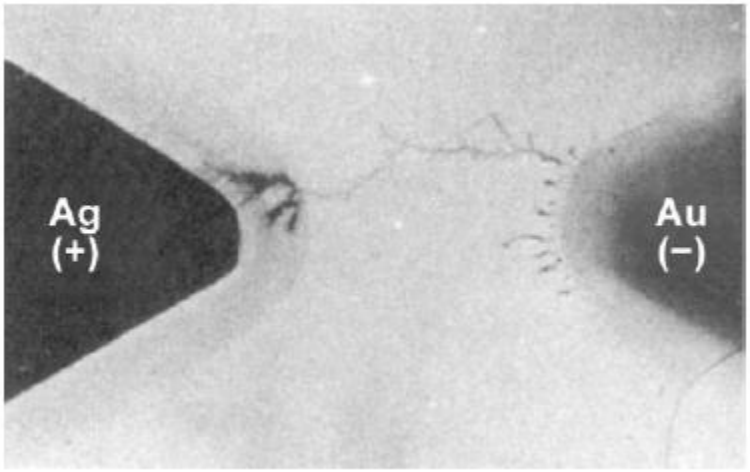

Figure 1.4: Growth of a Ag dendrite in a Ag/Ag-As_2S_3/Au system [9] [20].

1.3.2 The role of oxygen ions

The migration of oxygen ions is widely reported to play a key role in resistive switching [22-30], for oxide based non-ECM systems. The oxygen ions could come from the atmosphere or from an electrical reduction process of the bulk oxide. The existence of non-lattice oxygen ions was also reported by Yang *et al* [26]. Based on a Pt/TiO_2/Pt structure, Jeong *et al*. described the electroforming effects on the composition, structure, and electrical resistance of the system [28]. By applying a positive voltage/current to the TE, the growth of an oxygen-vacancy-enriched phase results in the formation of a conduction path in the bulk oxide; by applying a negative voltage/current to the TE, chemical oxidation reactions take place, and as a result the growth of conduction path is then retarded. Negative charged oxygen ions and

positively oxygen vacancies are two ion sources often discussed in oxide-based switching devices. The migration of oxygen ions leads to the formation of oxygen vacancies in the oxide, and the diffusion of oxygen vacancies could be regarded as a result of oxygen ion migration in the opposite direction. In contrast to the migration of oxygen ions through defect sites, the diffusion of oxygen vacancies is another source frequently discussed for resistive switching in the literature, for which a localized high temperature is needed, to overcome the high energy barrier [31].

The high switching speed in a switching device could be due to a short-range migration effect of oxygen ions. The direct evidence for the electro-migration of oxygen ions in a resistive switching is confirmed by Yoshida *et al*. They used ^{18}O tracer gas to analyze the oxygen migration in a NiO-based device [29]. A combined study using CAFM and time-of-flight secondary ion mass spectroscopy (TOF-SIMS) was performed in their study. Figs 1.5(a)(b) show that under a positive voltage, oxygen ions will move to the TE; while under a negative voltage, oxygen ions will move to the BE. This is confirmed by the TOF-SIMS depth profiles of ^{18}O ions in the region with/without writing, as shown in Fig 1.5(c). This work provided a microscopic description of the electro-migration of oxygen ions in a switching process.

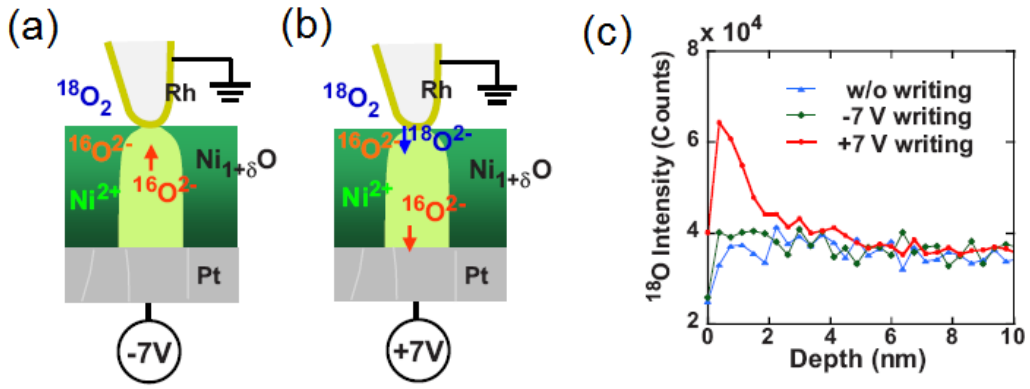

Figure 1.5: Schematic of oxygen movement under different polarity voltage biases: (a) a negative bias (-7 V); (b) a positive bias (+7 V). (c) TOF-SIMS depth profile of ^{18}O ions [29].

1.3.3 The filament and interface effects

Based on the type of conducting path, the mechanism of resistive switching can be divided into two groups: the filament type and the interface type [10]. In the filament resistive switching, current in LRS flows through the conductive filament in the insulating matrix. As a result of the filament rupture, current is significantly reduced in HRS. Based on the single-filament model, the resistance in LRS is independent of the electrode area, while the resistance in HRS increases as the electrode area decreases. This method is widely used to distinguish filament switching from interface switching in many reports. But for a multiple-filament system, this method cannot be applied. The filamentary mechanism specifies a direction for device scaling, and the size of the filament determines the ultimate scaling limit.

Open questions remain on the details of the filament formation and rupture in a switching system. Many reports are in favor of a single-filament switching model [32-38]. In contrast, multiple filament switching is also reported, but limited to a few material systems [39-41]. Using a mercury (Hg) probe system, Son and Shin studied the resistive switching with Hg as the top electrode to a NiO film (Fig 1.6) [41]. In the

experiment, they used local current atomic force microscopy (LCAFM) to switch the device to ON and OFF state respectively. From the high-resolution current image, a leakage current was found along the grain boundary regions. A large number of filaments were populated randomly in the oxide thin film.

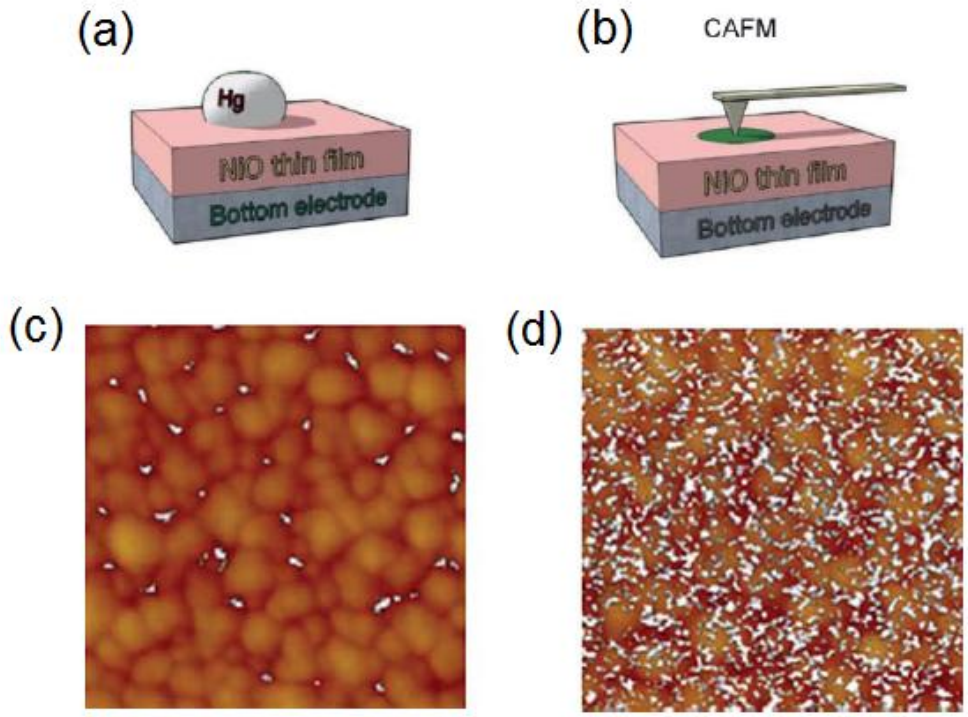

Figure 1.6: Conductivity mapping of the ON and OFF state of a NiO thin film. (a) and (b) sketch of the device with a removable Hg top electrode and of the LCAFM study; (c) and (d) LCAFM images of the NiO film recorded at OFF and ON states respectively [41].

There are many challenges in characterizing the filaments directly in an oxide-based non-ECM system. The nanofilaments are buried in the oxide matrix and very difficult to detect. Scanning electron microscopy (SEM) equipped with photoemission electron microscopy (PEEM) has been used to investigate the morphology and the chemical state of the μm size filament in CuO film [38]. In comparison, CAFM is a powerful tool to probe the conducting filaments, and most frequently used for resistive switching study [24, 29, 30, 32, 33, 41-43]. The CAFM studies under

atmosphere and high-vacuum conditions by Choi *et al*. [43] showed the resistance switching is closely related to the formation and elimination of conducting spots.

The as-prepared memory cell is always in a highly insulating state, for which an electroforming step is prerequisite to induce reliable resistive switching. By applying a (soft) breakdown electric field, the conductivity of the oxide film can be greatly reduced. The drift and diffusion of oxygen ions leads to the formation of oxygen deficient conductive filaments. A recent work by Kwon *et al*. showed the formation of conductive nanofilments of Magnéli phase after an electroforming process (Fig 1.7) [30]. The Magnéli phase is oxygen deficient, and known to have an ordering of oxygen vacancies. They applied a high electrical field to the pristine TiO_2 thin film, observed the conical shaped conductive filament through HRTEM, and measured the current-voltage characteristics using an *in situ* CAFM system.

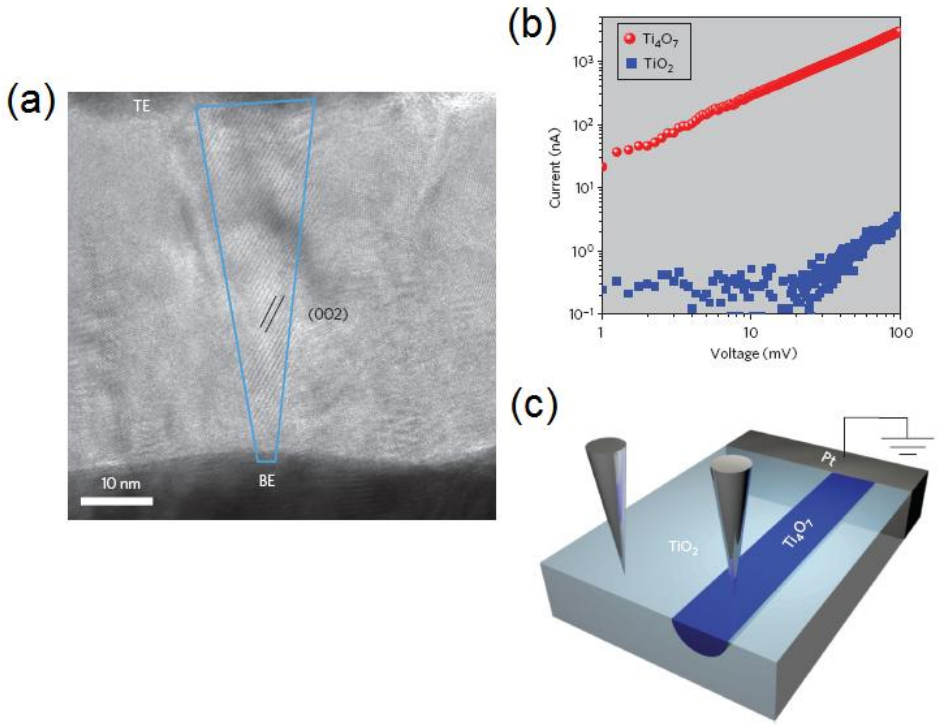

Figure 1.7: (a) High resolution TEM image of a Ti_4O_7 nanofilament in bulk TiO_2; (b) local I-V curves measured on the nanofilament and the background TiO_2; (c) schematic of the *in situ* I-V scan setup [30].

In the interface type resistive switching, the switching takes place at the interface between the metal electrode and the oxide [8-10]. Contact resistance at the interface controls the switching characteristics of the device. Using a Ti/PCMO junction, Sawa *et al*. demonstrated an interface model shown in Fig 1.8 [10, 44]. In the LRS electrons tunnel through the thin Schottky-like barrier, whereas in the HRS the thick barrier significantly decreases the tunneling current. The current through the junction is determined by the interface barrier, which is modified by the electrical field. With one interface ohmic-like and the other interface Schottky-like, change of the barrier (height and/or width) of the Schottky-like interface leads to the switching device at different resistance levels. The interface switching mechanism was also discussed by Kim *et al*. based on a $Pt/TiO_2/Pt$ structure [45].

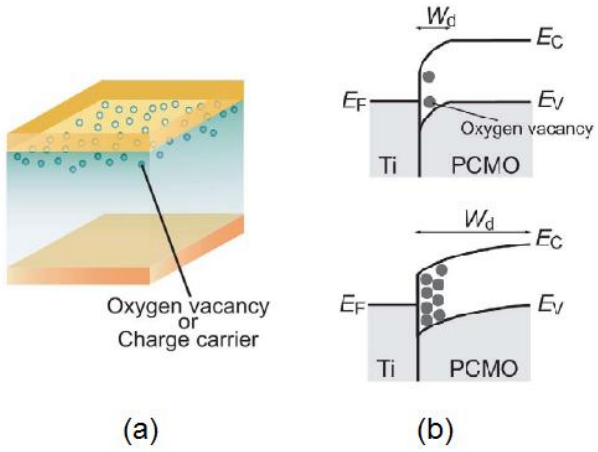

Figure 1.8: (a) A schematic model of the interface modification-induced resistive switching; (b) Change of the depletion layer width at the Ti/PCMO interface by applying an electric field [10, 44].

1.4 Resistive switching in TiO_2 thin films

To date, the resistance switching effect has been observed in a variety of material systems that include binary metal oxide (e.g. TiO_2, ZnO, NiO, CuO, ZrO_2, Fe_2O_3, Ta_2O_5), multinary metal oxide (e.g. $SrTiO_3$, $SrZrO_3$, $LiNbO_3$), SiO, solid-state electrolytes (e.g. Ag_2S, AgGeSe) and organic materials [6-30, 32-60]. There have

been a large number of experimental and theoretical studies on the development of switching devices.

Among the various oxide materials demonstrating switching behavior, TiO_2 appears to be one of the most studied materials for RRAM. Besides memory applications, TiO_2 is also widely used in applications such as photocatalyst, solar cells, waste remediation and gas sensors. In its stoichiometric form, TiO_2 is a wide-band gap insulator. By excess electrons originating from the defect state of reduced TiO_2, its conductivity can be greatly enhanced and show semiconducting (or conducting) electrical behavior. Hermes *et al*. recently successfully fabricated TiO_2-based nanocrossbar devices, for which transient currents for switching in the range of 200 μA and fast pulses as small as 5 ns were realized [59]. This shows TiO_2 to be a promising device material for nonvolatile-memory application.

Based on HRTEM studies, Fujimoto *et al*. showed that the high-speed resistive change was due to a TiO_2 nanolayer (~ 2.5 nm) formed on TiN [60]. They proposed that the electron injection accompanied by oxygen vacancy formation and annihilation leads to the resistance switching. The recent work by Kwon *et al*. on the direct observation of nanofilaments in TiO_2 thin films confirmed the existence of conductive filaments in the bulk oxide [30]. On the base of a 50 nm × 50 nm crossbar of Pt/TiO_2/Pt MIM structure, one group from HP (Hewlett Packard) demonstrated the so-called "memristive" switching behavior, predicted as the fourth basic circuit element by Chua in 1970s [11, 12, 61].

TiO_2 has turned out to be a very attractive material for the next generation of non-volatile memories. Studies into TiO_2 have greatly enhanced our understanding of the switching mechanisms. In this regard, TiO_2 is chosen as the resistance switching material in this study.

1.5 Motivation and outline of dissertation

Although intensive studies have been carried out on the understanding of the mechanisms of resistive switching in various materials, there are still many debates and unsolved problems. Besides the experimental challenges, understanding resistive switching at the microscopic level is also lacking. The main purpose of this thesis is to study resistive switching in TiO_2 based devices using both experimental and theoretical methods. It is hoped that this work will enhance our comprehension of the resistive switching mechanism, and accelerate the development of RRAM memory devices.

This dissertation consists of both the experimental and theoretical investigations of resistive switching mechanism in TiO_2. Prior to the main work, the main experimental and theoretical methods in this study are introduced in chapter 2. In chapter 3, studies on TiO_2 thin films using scanning probe microscopy techniques are presented. An integrated model combining both interfacial and filamentary effects is introduced. Chapter 4 investigates the negative differential resistance behavior in a resistive switching device. Chapter 5 studies the various filamentary characteristics in resistive switching and the integrated model will further be discussed. Finally, Chapter 6 concludes the dissertation and future works are suggested.

References

[1] G. E. Moore, “Progress in digital integrated electronics,” *IEEE. IEDM Tech. Dig.*, 11-13, (1975).

[2] The international technology roadmap for semiconductors (ITRS) 2007.

[3] J. T. Evans and R. Womack, “An experimental 512-bit nonvolatile memory with ferroelectric storage cell,” *IEEE J Solid-State Circuits* **23**,1171-1175 (1988).

[4] S. S. P. Parkin, C. Kaiser, A. Panchula, P. M. Rice, B. Hughes, M. Samant and S. H. Yang, “Giant tunnelling magnetoresistance at room temperature with MgO (100) tunnel barriers,” *Nat. Mater.* **3**, 862-867 (2004).

[5] A. Pirovano, A. L. Lacaita, A. Benvenuti, F. Pellizzer and R. Bez, "Electronic switching in phase-change memories," *IEEE Trans. Electr. Devices* **51**, 452-459 (2004).

[6] G. I. Meijer, “Who wins the nonvolatile memory race?” *Science* **319**, 1625-1626 (2008).

[7] I. G. Baek, M. S. Lee, S. Seo, M. J. Lee, D. H. Seo, D. -S. Suh, J. C. Park, S. O. Park, H. S. Kim, I. K. Yoo, U. -In. Chung and J. T. Moon, “Highly scalable non-volatile resistive memory using simple binary oxide driven by asymmetric unipolar voltage pulses,” *IEDM Tech. Dig.*, 587-590 (2004).

[8] R. Waser and M. Aono, “Nanoionics-based resistive switching memories,” *Nat. Mater.* **6**, 833-840 (2007).

[9] R. Waser, R. Dittmann, G. Staikov and K. Szot, “Redox-based resistive switching memories – nanoionic mechanisms, prospects, and challenges,” *Adv. Mater.* **21**, 2632-2663 (2009).

[10] A. Sawa, "Resistive switching in transition metal oxides," *Mater. Today* **11**, 28-36 (2008).

[11] J. J. Yang, M. D. Pickett, X. Li, D. A. A. Ohlberg, D. R. Stewart and R. S. Williams, "Memristive switching mechanism for metal/oxide/metal nanodevices," *Nat. Nanotechnol.* **3**, 429-433 (2008).

[12] D. B. Strukov, G. S. Snider, D. R. Stewart and R. S. Williams, "The missing memristor found," *Nature* **453**, 80-83 (2008).

[13] T. W. Hickmott, "Low-frequency negative resistance in thin anodic oxide films," *J. Appl. Phys.* **33,** 2669-2682 (1962).

[14] J. F. Gibbons and W. E. Beadle, "Switching properties of thin NiO films," *Solid-state Electr.* **7**, 785-797 (1964).

[15] J. G. Simmons and R. R. Verderber, "New conduction and reversible memory phenomena in thin insulating films," *Proc. R. Soc. Lond. A* **301,** 77–102 (1967).

[16] D. S. Jeong, H. Schroeder and R. Waser, "Coexistence of bipolar and unipolar resistive switching behaviors in a Pt/TiO_2/Pt stack," *Electrochem. Solid-State Lett*. **10**, G51-G53 (2007).

[17] L. Goux, J. G. Lisoni, M. Jurczak, D. J. Wouters, L. Courtade and Ch. Muller, "Coexistence of the bipolar and unipolar resistive-switching modes in NiO cells made by thermal oxidation of Ni layers," *J. Appl. Phys*. **107**, 024512 (2010).

[18] K. Terabe, T. Hasegawa, T. Nakayama and M. Aono, "Quantized conductance atomic switch," *Nature* **433,** 47–50 (2005).

[19] M. N. Kozicki, M. Park and M. Mitkova, "Nanoscale memory elements based on solid-state electrolytes," *IEEE Trans. Nanotechnol.* **4**, 331-338 (2005).

[20] Y. Hirose and H. Hirose, "Polarity-dependent memory switching and behavior of Ag dendrite in Ag-photodoped amorphous As_2S_3 films," *J. Appl. Phys.* **47**, 2767-2772 (1976).

[21] M. N. Kozicki, M. Mitkova, M. Park, M. Balakrishnan and C. Gopalan, "Information storage using nanoscale electrodeposition of metal in solid electrolytes," *Superlattices Microstruct.* **34**, 459-465 (2003).

[22] Y. B. Nian, J. Strozier, N. J. Wu, X. Chen and A. Ignatiev, "Evidence for an oxygen diffusion model for the electric pulse induced resistance change effect in transition-metal oxides," *Phys. Rev. Lett*. **98**, 146403 (2007).

[23] J. P. Shi, Y. G. Zhao, H. J. Zhang, H. F. Tian and X. P. Zhang, "Oxygen electromigration induced nonvolatile resistance switching at Ag/La_2CuO_{4+x} interface," *Appl. Phys. Lett.* **94**, 192103 (2009).

[24] K. Szot, W. Speier, G. Bihlmayer and R. Waser, "Switching the electrical resistance of individual dislocations in single-crystalline $SrTiO_3$," *Nat. Mater*. **5**, 312-320 (2006).

[25] Y. H. Do, J. S. Kwak, Y. C. Bae, K. Jung, H. Im and J. P. Hong, "Hysteretic bipolar resistive switching characteristics in TiO_2/TiO_{2-x} multilayer homojunctions," *Appl. Phys. Lett*. **95**, 093507 (2009).

[26] M. K. Yang, J. W. Park, T. K. Ko and J. K. Lee, "Bipolar resistive switching behaviour in $Ti/MnO_2/Pt$ structure for non-volatile memory devices," *Appl. Phys. Lett*. **95**, 042105 (2009).

[27] C. Chen, C. Song, J. Yang, F. Zeng and F. Pan, "Oxygen migration induced resistive switching effect and its thermal stability in $W/TaO_x/Pt$ structure," *Appl. Phys. Lett.* **100**, 253509 (2012).

[28] D. S. Jeong, H. Schroeder, U. Breuer and R. Waser, "Characteristic electroforming behavior in Pt/TiO_2/Pt resistive switching cells depending on atmosphere," *J. Appl. Phys.* **104**, 123716 (2008).

[29] C. Yoshida, K. Kinoshita, T. Yamasaki and Y. Sugiyama, "Direct observation of oxygen movement during resistance switching in NiO/Pt film," *Appl. Phys. Lett*. **93**, 042106 (2008).

[30] D. H. Kwon, K. M. Kim, J. H. Jang, J. M. Jeon, M. H. Lee, G. H. Kim, X. S. Li, G. S. Park, B. Lee, S. Han, M. Kim and C. S. Hwang, "Atomic structure of conducting nanofilaments in TiO_2 resistive switching memory," *Nat. Nanotechnol.* **5**, 148-153 (2010).

[31] I. Denk, W. Munch and J. Maier, "Partial conductivities in $SrTiO_3$: Bulk polarization experiments, oxygen concentration cell measurements, and defect-chemical modeling," *J. Am. Cer. Soc*. **78**, 3265-3269 (1995).

[32] K. Szot, R. Dittmann, W. Speier and R. Waser, "Nanoscale resistive switching in $SrTiO_3$ thin films,"*Phys. Status Solidi* **1**, R86-R88 (2007).

[33] R. Muenstermann, T. Menke, R. Dittmann and R. Waser, "Coexistence of filamentary and homogeneous resistive switching in Fe-doped $SrTiO_3$ thin-film memristive devices," *Adv. Mater*. **22**, 4819-4822 (2010).

[34] J. J. Yang, F. Miao, M. D. Pickett, D. A. A. Ohlberg, D. R. Stewart, C. N. Lau and R. S. Williams, "The mechanism of electroforming of metal oxide memristive switches," *Nanotechnology* **20**, 215201 (2009).

[35] W. Shen, R. Dittmann and R. Waser, "Reversible alternation between bipolar and unipolar resistive switching in polycrystalline barium strontium titanate thin films," *J. Appl. Phys.* **107**, 094506 (2010).

[36] D. Ielmini, S. Spiga, F. Nardi, C. Cagli, A. Lamperti, E. Cianci and M. Fanciulli, "Scaling analysis of submicrometer nickel-oxide-based resistive switching memory devices," *J. Appl. Phys.* **109**, 034506 (2011).

[37] K. Fujiwara, T. Nemoto, M. J. Rozenberg, Y. Nakamura and H.Takagi, "Resistance switching and formation of a conductive bridge in metal/binary oxide/metal structure for memory devices," *Jpn. J. Appl. Phys*. **47**, 6266-6271 (2008).

[38] R. Yasuhara, K. Fujiwara, K. Horiba, H. Kumigashira, M. Kotsugi, M. Oshima and H. Takagi, "Inhomogeneous chemical states in resistance-switching devices with a planar-type Pt/CuO/Pt structure," *Appl. Phys. Lett*. **95**, 012110 (2009).

[39] K. Kinoshita, T. Tamura, M. Aoki, Y. Sugiyama and H. Tanaka, "Lowering the switching current of resistance random access memory using a hetero junction structure consisting of transition metal oxides," *Jpn. J. Appl. Phys*. **45**, L991–L994 (2006).

[40] Q. L. Hu, S. M. Jung, H. H. Lee, Y. –S. Kim, Y. J. Choi, D. –H. Kang, K. –B. Kim and T. –S. Yoon, "Resistive switching characteristics of maghemite nanoparticle assembly," *J. Phys. D: Appl. Phys*. **44**, 085403 (2011).

[41] J. Y. Son and Y. -H. Shin, "Direct observation of conducting filaments on resistive switching of NiO thin films," *Appl. Phys. Lett*. **92**, 222106 (2008).

[42] M. H. Lee and C. S. Hwang, " Resistive switching memory: observations with scanning probe microscopy," *Nanoscale* **3**, 490-502 (2011).

[43] B. J. Choi, D. S. Jeong, S. K. Kim, C. Rohde, S. Choi, J. H. Oh, H. J. Kim, C. S. Hwang, K. Szot, R. Waser, B. Reichenberg and S. Tiedke, "Resistive switching

mechanism of TiO_2 thin films grown by atomic-layer deposition," *J. Appl. Phys*. **98**, 033715 (2005).

[44] A. Sawa, T. Fujii, M. Kawasaki and Y. Tokura, "Interface transport properties and resistance switching in perovskite-oxide heterojunctions," *Proc. SPIE* 5932 (2005).

[45] K. M. Kim, B. J. Choi, Y. C. Shin, S. Choi and C. S. Hwang, "Anode-interface localized filamentary mechanism in resistive switching of TiO_2 thin films," *Appl. Phys. Lett*. **91**, 012907 (2007).

[46] J. Qi, M. Olmedo, J. J. Ren, N. Zhan, J. Z. Zhao, J. G. Zheng and J. L. Liu, "Resistive switching in single epitaxial ZnO nanoislands," *ACS Nano* **6**, 1051–1058 (2012).

[47] D. Y. Lee and T. Y. Tseng, "Unipolar resistive switching characteristics of a ZrO_2 memory device with oxygen ion conductor buffer layer," *IEEE Electron Device Lett* **33**, 803-805 (2012).

[48] M. J. Lee, C. B. Lee, D. Lee, S. R. Lee, M. Chang, J. H. Hur, Y. B. Kim, C. J. Kim, D. H. Seo, S. Seo, U. I. Chung, I. K. Yoo and K. Kim, "A fast, high-endurance and scalable non-volatile memory device made from asymmetric Ta_2O_{5-x}/TaO_{2-x} bilayer structures," *Nat. Mater*. **10**, 625-630 (2011).

[49] W. Lee, J. Park, S. Kim, J. Woo, J. Shin, G. Choi, S. Park, D. Lee, E. Cha, B. H. Lee and H. Hwang, "High current density and nonlinearity combination of selection device based on $TaO_x/TiO_2/TaO_x$ structure for one selector - one resistor arrays," *ACS Nano* **6**, 8166-8172 (2012).

[50] J. Yao, Z. Jin, L. Zhong, D. Natelson and J. M. Tour, "Two-terminal nonvolatile memories based on single-walled carbon nanotubes," *ACS Nano* **3**, 4122-4126 (2009).

[51] Y. Watanabe, J. G. Bednorz, A. Bietsch, Ch. Gerber, D. Widmer, A. Beck and S. J. Wind, "Current-driven insulator–conductor transition and nonvolatile memory in chromium-doped $SrTiO_3$ single crystals," *Appl. Phys. Lett.* **78,** 3738-3740 (2001).

[52] C. Y. Liu, P. H. Wu, A. Wang, W. Y. Jang, J. C. Young, K. Y. Chiu and T. Y. Tseng, "Bistable resistive switching of a sputter-deposited Cr-doped $SrZrO_3$ memory film," *IEEE Electron Device Lett.* **26,** 351-353 (2005).

[53] H. Akazawa, "Observation of both potential barrier-type and filament-type resistance switching with sputtered $LiNbO_3$ thin films," *Jpn. J. Appl. Phys.* **46**, L848-L850 (2007).

[54] Z. M. Liao, C. Hou, H. Z. Zhang, D. S. Wang and D. P. Yu, "Evolution of resistive switching over bias duration of single Ag_2S nanowires," *Appl. Phys. Lett*. **96**, 203109 (2010).

[55] C. Schindler, M. Meier, R. Waser and M. N. Kozicki, "Resistive switching in Ag-Ge-Se with extremely low write currents," Non-Volatile Memory Technology Symposium, 82-85 (2007).

[56] R. S. Potember, T. O. Poehler and D. O. Cowan, "Electrical switching and memory phenomena in Cu-TCNQ thin films," *Appl. Phys. Lett.* **34,** 405–407 (1979).

[57] Y. Yang, J. Ouyang, L. Ma, R. J. –H. Tseng and C. –W. Chu, "Electrical switching and bistability in organic/polymeric thin films and memory devices," *Adv. Funct. Mater.***16**, 1001-1014 (2006).

[58] J. C. Scott and L. D. Bozano, "Nonvolatile memory elements based on organic materials," *Adv. Mater.* **19,** 1452–1463 (2007).

[59] C. Hermes, M. Wimmer, S. Menzel, K. Fleck, G. Bruns, M. Salinga, U. Böttger, R. Bruchhaus, T. Schmitz-Kempen, M. Wuttig and R. Waser, "Analysis of transient currents during ultrafast switching of TiO_2 nanocrossbar devices," *IEEE Electron Device Lett*. **32**, 1116-1118 (2011).

[60] M. Fujimoto, H. Koyama, M. Konagai, Y. Hosoi, K. Ishihara, S. Ohnishi, and N. Awaya, "TiO_2 anatase nanolayer on TiN thin film exhibiting high-speed bipolar resistive switching," *Appl. Phys. Lett*. **89**, 223509 (2006).

[61] L. O. Chua, "Memristor – the missing circuit element," *IEEE Trans. Circuit Theory* **CT-18**, 507-519 (1971).

Chapter 2

Experimental Techniques and Modeling Methods

2.1 Sputtering and sputter deposition

Sputtering and sputtering deposition are widely used for erosion of surfaces and deposition of films [1-5]. Sputtering is a process whereby atoms are ejected from a

target surface through momentum exchange by bombardment, which is widely used for depth profiling, surface patterning and cleaning. Sputter deposition is the accumulation of the sputtered atoms on to a sample surface, and widely used for film deposition and surface coating.

The sputtering process is shown schematically in Fig 2.1. The yield for sputtering relies on the transfer of physical momentum and kinetic energy from the incident particle to the surface atoms. The particle strikes the surface with enough energy to break bonds and dislodge the surface or near-surface atoms. The knock-on collisions result in a number of atoms at or near the surface being ejected from the solid. The low energy sputtering can be used for ultra thin film (monolayers) deposition. Increasing the incident ion energy leads to higher yields. An increase in the ion flux results in an increase in the number of sputtered atoms.

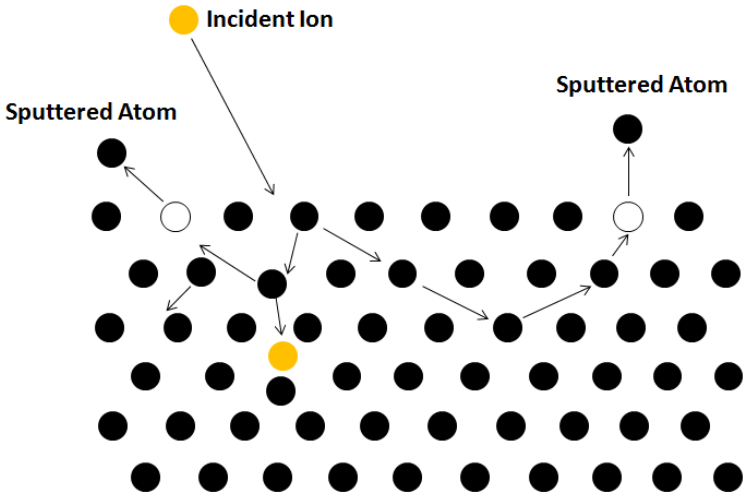

Figure 2.1: Schematic representation of physical sputtering process.

2.1.1 Plasma and sputtering systems

An acceleration voltage within a vacuum chamber results in incident ions with energies in the hundreds of eV energy range. There are two categories of systems

used to generate ions: ion beams and plasma. In the ion beam case, an ion beam is extracted from the ion source to bombard the target. In the plasma source, the target to be bombarded is immersed in the plasma. Most of the discussions focus on plasma sources, which are widely used for industrial applications.

The plasma can be easily generated by a glow discharge. A glow discharge typically consists of several different dark and glowing regions, as shown in Fig 2.2.

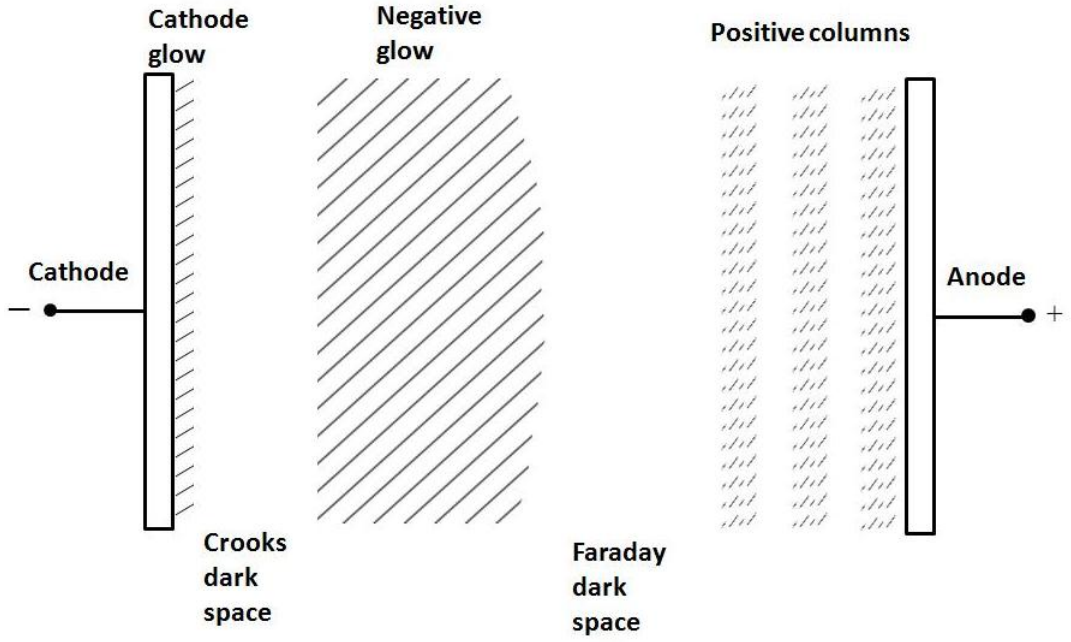

Figure 2.2: Characteristic regions of a glow discharge for a sputtering process [3].

Near the cathode is a very thin layer of ion space charge, followed by a dark space region, where most of the potential between the cathode and the anode drops. At the negative glow discharge region, the plasma is sustained by the secondary electrons generated from ion bombardment of the target (cathode). These electrons are accelerated away from the cathode. After collisions with gas atoms, the electrons lose their energy and continue to drift toward the cathode. After the Faraday dark space

region, the electrons are accelerated again by the anode, creating columns of alternating faintly glowing and dark regions (positive columns).

In the cathode sheath region, the evaporation or sputtering of the target material takes place. The emitted light from the cathode glow is the characteristic of the gas and the target material used. The secondary electrons are the primary source of energy to the plasma discharge. With adequate voltage across the electrodes inside a vacuum system, the gas will breakdown into a plasma discharge.

Due to the build-up of positive charges on the insulating targets, DC sputtering has great difficulties in sputtering an insulator material. For this purpose, a RF field source is applied. In a high frequency RF field, both electrons and ions receive an AC field, but only electrons can respond to the RF field. The electrons oscillate with the field, and charge accumulation at the target is avoided. Most manufacturing systems use 13.56 MHz or simple multiples (2× or 3×). The oscillation of fields in the plasma results in additional electron motion within the plasma, and an increase in the plasma density compared to a DC sputtering system. The density increase leads to a faster sputtering process.

The sputtering yield from the target varies with the materials, and the incident ions energy. To increase the secondary electron production, as well as the efficiency of ionization, a cathode design using a magnetic field called magnetron is utilized. The function of the magnetic field is to increase the confinement of secondary electrons near the cathode surface, and as a result the plasma density is increased. By applying a magnetron source, the sputtering can operate in a significantly lower pressure, with increased deposition rate. Magnetron sputtering sources are widely used for sputtering applications. Fig 2.3 shows the configuration for a circular planar magnetron cathode. A region of dense plasma typically extends from the cathode

surface. The improved magnetron cathode is the basis for industrial high-rate, single-wafer deposition systems.

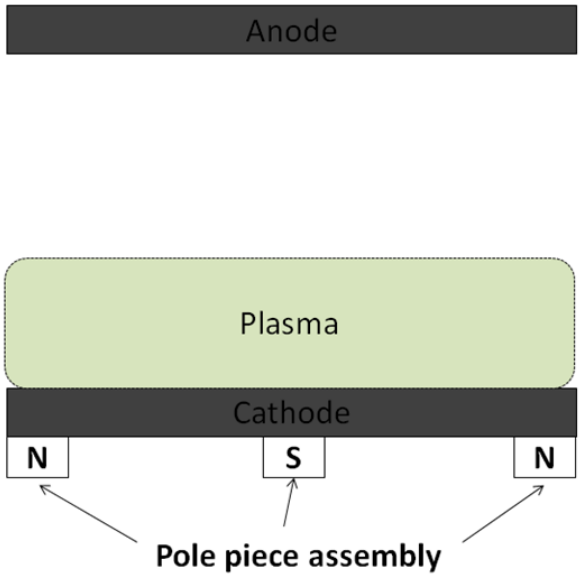

Figure 2.3: Schematic representation of the plasma confinement for a circular planar magnetron cathode.

Unlike the DC and RF sputtering systems, the secondary electrons are essentially trapped within a region close to the target (Fig 2.3). Eventually they lose their kinetic energy due to frequent collisions. Ions in the drift region have a probability of hitting the target which is close by. This results in more secondary electrons and eventually extremely dense plasma is then formed.

The application of magnetron greatly enhances the discharge current. Magnetrons operate with a current-voltage relation:

$$I = kV^n, \tag{2.1}$$

where I is the discharge current, V is the voltage, and k and n are constants. It is an empirical equation. Much effort has been put into calibrating the various constants for

different systems. A high value of *n* means that small voltage increases could result in large current increases. Typical magnetron systems operate with *n* of 5-10.

2.1.2 Reactive sputtering deposition

The number of atoms emitted from the cathode could be simply treated as a function of the discharge current, the sputter yield and the deposition time. Deposition probability alters with the target material, the gas species and the system parameters. The highest probability occurs for low pressure, short throw distance (substrate-target gap), and a gas specie which is lighter than the sputtered species. Sputtering with a heavy gas (for example, Kr to Ar), is often counterproductive. The probability of an atom getting to the solid is significantly reduced, although the sputter yield may be slightly increased.

Most of the atoms emitted from a target are emitted as atoms rather than molecules or clusters. Chemical reactions of these atoms in flight are rare, but it is possible that the freshly deposited atoms on the substrate surface can react with gas atoms that impinge on the surface to form a compound. This is known as the reactive sputtering.

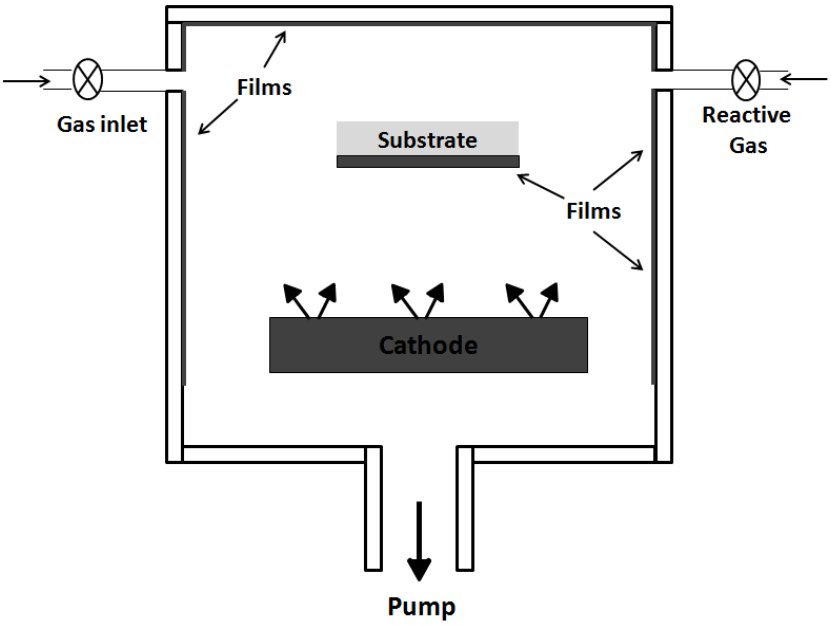

Figure 2.4: A typical reactive sputtering deposition system.

Reactive sputtering is commonly used for oxide and nitride thin films deposition. A typical reactive sputtering deposition system is shown in Fig 2.4. Besides the sample, films will also be deposited to the chamber walls. A schedule preventive maintenance is required for the system. With some partial pressure of an inert gas, such as Ar, and a partial pressure of a reactive species such as O_2 or N_2, the reactive sputtering occurs.

When using reactive sputtering, one problem frequently encountered is the poisoning of the target by the reactive gas. As the flow rate reaches a critical point, a compound layer consisting of oxide, nitride or other materials will be formed on the target surface. This compound layer usually exhibits a much lower sputtering yield than that of the purely metallic target. A dramatic drop in the sputtering rate occurs. This turns off the supply of metallic atoms to the film surface, and more of the reactive gas is unused. Further oxidation of the target leads to further reduction of the

metal flux. The dropping of the deposition rate is always accompanied with significant changes in the discharge voltage.

2.1.3 Sputtering instrumentation in this study

The sputtering deposition experiments were done at the Silicon Nano Device Lab (SNDL)-NUS and the Institute of Materials Research and Engineering (IMRE). Fig 2.5 shows the sputtering facility used in this study. The system consists of a main cylindrical chamber and different units such as vacuum, gas controlling, magnetron and RF coils. A loadlock chamber is used for sample transfer. The vacuum system includes a turbo molecular pump (TMP) backed by a roughing pump. The gases are injected through needle valves and the flow rates are controlled by mass flow controllers (MFC).

Figure 2.5: Overview of a Denton sputtering system.

2.2 Scanning probe/atomic force microscopy

Since its introduction in1986 [6], the atomic force microscopy (AFM) has widely been used for surface investigations of metals, oxides and semiconductors. Through the development of the past decades, AFM can work with different functions and provide a range of morphological, electrical, ferroelectric, and mechanical information of a sample [7, 8]. The convenience and usefulness of this technique has made it one of the most frequently employed techniques in nano-scale characterization.

AFM can operate on conducting and nonconducting surfaces, and image virtually any flat solid surface without the need for surface preparation. A cantilever with a small tip scans the solid surface, and the deflection of the cantilever is detected by the reflection of a laser beam. Fig 2.6 shows schematically an AFM setup. When the tip is brought close to a sample surface, forces between the tip and the sample lead to a deflection of the cantilever. The deflection is typically measured using a laser spot reflected from the cantilever into an array of photodiodes. AFM is based on the existence of a separation-dependent force between two bodies. A feedback system is employed to adjust the tip-to-sample distance, so that a constant force between the tip and the sample can be maintained. The sample is mounted on a piezoelectric tube that can move the sample in the x, y and z directions. The resulting map of the scanned area represents the topography of the sample.

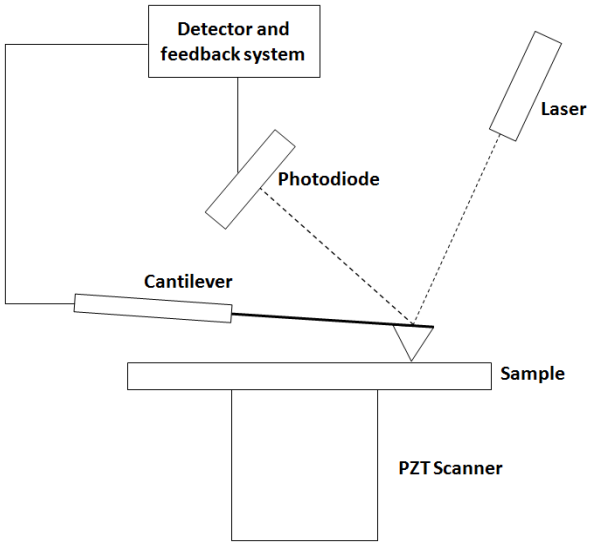

Figure 2.6: Schematic diagram of atomic force microscope.

Based on the different force regimes of tip-sample interaction, there are three operating modes for image acquisition: contact mode, tapping mode and non-contact mode. In contact mode, the probe is in constant contact with the sample surface. The repulsive contact forces between the probe and the sample cause the cantilever to bend. The z-feedback loop monitors the cantilever deflection and constantly adjusts to maintain a constant force on the sample. In tapping mode, the AFM is operating in both the repulsive and attractive regions of the tip-sample interaction, with the cantilever oscillating at or near its resonance frequency. Variations in the topography of the sample surface result in the oscillation amplitude changes of the cantilever. In non-contact mode, the oscillating tip is kept at a distance above the sample surface within the long-range van der Waals attractive forces of the tip-sample interaction. The major advantage of non-contact AFM is that the technique is non-destructive to the sample. Since the attractive forces involved are very small and less sensitive to the tip-sample separation, the images generated generally have a lower spatial resolution. Fig 2.7 shows the force and the tip-to-sample separation relationship working at

different distance regimes.

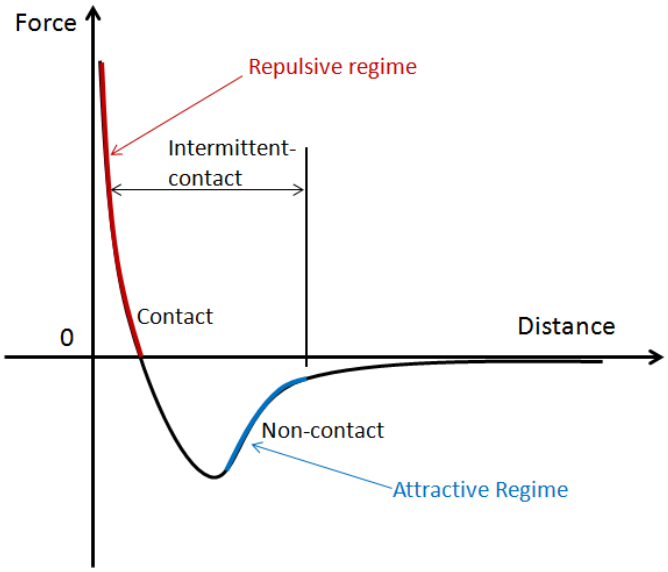

Figure 2.7: Force versus tip-to-sample distance curve.

2.2.1 Conductive atomic force microscopy

Conductive atomic force microscopy (CAFM) is a variation of AFM, which uses electrical current to construct the surface profile of the studied sample [9, 10]. With CAFM, local electrical properties can be studied with the conductive tip being in contact or in close proximity with a sample surface. The current flowing between the tip and the sample is measured as a voltage is applied. When the tip is scanning over the surface, a simultaneous mapping of the local leakage currents and the topography is obtained.

The CAFM operates mainly in two different modes: the spectroscopic mode and the imaging mode. In the spectroscopic mode, the tip is fixed at a specific position, while the voltage is being swept. As such, the current-voltage characteristic from local areas of the sample is recorded. The electrical field imposes electrical stresses, for which defects may be created and charges may be trapped during the measurement.

The ramping speed may affect the current-voltage characteristic in a scan process. In the imaging mode, the tip scans the surface with a constant force, while a constant voltage is applied between the tip and the sample. The tunneling current and surface morphology are measured simultaneously, which allows investigating the link between the localized morphological features and the current-voltage characteristics.

2.2.2 Kelvin probe force microscopy

Kelvin probe force microscopy (KPFM) was introduced as a tool to measure the local contact potential between a conducing tip and the sample, by Nonnenmacher *et al*. in 1991 [11]. KPFM is based on the instrumentation of an AFM system. It has been extensively used to characterize the nano-scale electrical properties of various material surfaces [12, 13]. By using this technique, mapping of work function or surface potential distributions of a sample with high spatial resolution can be obtained.

The contact potential difference (CPD) between the tip and the sample is defined as,

$$\Delta\Phi = \frac{\phi_{tip} - \phi_{sample}}{-e}, \tag{2.2}$$

where e is the electron charge, ϕ_{sample} and ϕ_{tip} are the work functions of the sample and the tip respectively. By applying a voltage to the tip, KPFM measures the work function of the sample. With a given voltage $U_{bias} = V_{DC} + V_{AC}\sin(\omega t)$, the potential difference between the tip and the sample will be:

$$\Delta V = (V_{DC} + \Delta\Phi) + V_{AC}\sin(\omega t). \tag{2.3}$$

The electrostatic force is the rate of change of the energy with respect to the tip sample separation *z*,

$$F_{es}(z) = -\frac{1}{2}\Delta V^2 \frac{dC(z)}{dz}. \tag{2.4}$$

Substituting Eq. (2.3) to Eq. (2.4) gives the expression:

$$F_{es}(z,t) = -\frac{1}{2}\frac{\partial C(z)}{\partial z}[(V_{DC} + \Delta\Phi) + V_{AC}\sin(\omega t)]^2. \quad (2.5)$$

This equation can be divided into three parts:

$$F_{DC} = -\frac{1}{2}\frac{\partial C(z)}{\partial z}[(V_{DC} + \Delta\Phi)^2], \quad (2.6)$$

$$F_{\omega} = -\frac{\partial C(z)}{\partial z}(V_{DC} + \Delta\Phi)V_{AC}\sin(\omega t), \quad (2.7)$$

$$F_{2\omega} = \frac{1}{4}\frac{\partial C(z)}{\partial z}{V_{AC}}^2[\cos(2\omega t) - 1]. \quad (2.8)$$

In all KPM variants the force component at the excitation frequency is nullified by adjusting the bias voltage V_{DC} to $\Delta\Phi$, and the value of V_{DC} is acquired for each point on the sample surface, composing a map of surface potential of the whole surface area. The electrostatic force F_{ω} can be detected either under AM (amplitude modulation) mode or FM (frequency modulation) mode. In AM mode, the force is directly measured from the amplitude of the cantilever oscillation, and the Kelvin controller maintains zero oscillation amplitude by adjusting V_{DC}. In FM mode, the frequency of the Kelvin modulation is usually off-resonance and sensitive to the force gradient. For the Kelvin feedback, the frequency shift is demodulated, and V_{DC} is adjusted. Generally, FM-KPFM has a higher spatial resolution of measuring the contact potential difference than in AM-KPFM, while a lower energy resolution in measurements.

2.3 Photoelectron spectroscopy

2.3.1 Basic principles

Photoelectron spectroscopy utilizes the photoelectric effect to characterize the kinetic energy distribution of the emitted photoelectrons to study the composition and electronic state of the surface region of a sample [14, 15]. According to the excitation source, the technique can be classified as: (i) X-ray photoemission spectroscopy

(XPS), using soft X-rays to examine the core electron core levels; and (ii) ultraviolet photoelectron spectroscopy (UPS), using ultraviolet photons radiation to examine the valence electron levels.

The photoelectric effect was discovered by Heinrich Hertz in 1887 [16] who observed that electrodes illuminated with ultraviolet light create electric sparks more easily. In 1905, Albert Einstein proposed the photoelectric law [17].

The energy of a photon is given by the Einstein relation,

$$E = hv, \tag{2.9}$$

where h is Plank's constant, v is the frequency of the light source. Conservation of energy requires that,

$$E(A) + hv = E(A^+) + E(e^-), \tag{2.10}$$

where $E(A)$ and $E(A^+)$ stand for the initial and final state energy respectively. This equation can be rearranged to give the following expression for the kinetic energy of the photoelectron:

$$E_{kin} = hv - [E(A^+) - E(A)]. \tag{2.11}$$

The term $[E(A^+) - E(A)]$ is generally called the binding energy (E_B) of the electrons.

In practice, a photoelectron spectrum can be obtained by measuring the kinetic energy distribution of the emitted electrons using an appropriate electron analyzer,

$$E_{kin} = hv - E_B - \phi + \delta, \tag{2.12}$$

where ϕ is the electron spectrometer work function, and δ is the energy shift contributed by net surface charges.

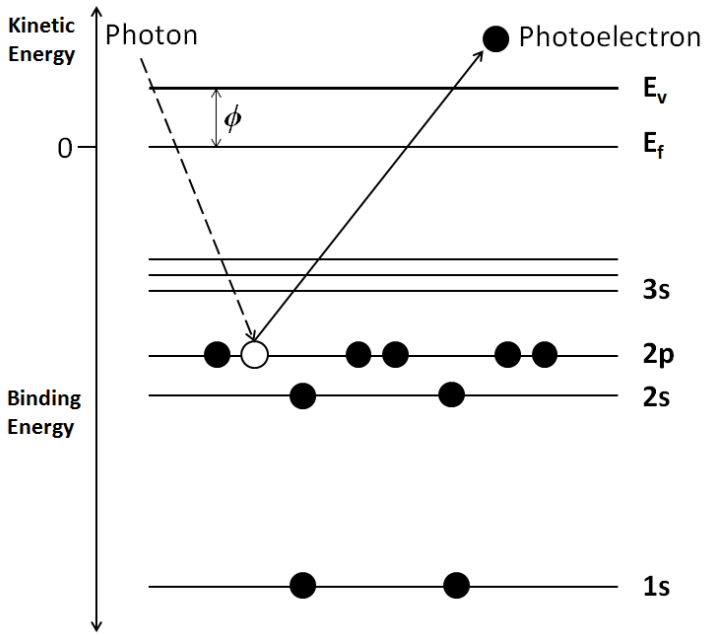

Figure 2.8: Schematic diagram of the photoemission process.

Fig 2.8 shows schematically a photoemission process. The Fermi energy E_f is at the top of the valence band and the energy difference between E_f and vacuum level E_v is the work function ϕ. If photoemission takes place at a core level with binding energy E_B (at E_f, E_B=0), the photoelectrons with kinetic energy $E_{kin} = hv - E_B - \phi$ can be detected.

In chemistry, the binding energy is related to the charge state of an atom and different atoms in different structures have their unique binding energies. Photoemission spectroscopy can be used to provide the information such as elemental identification, chemical states of the elements, relative composition of the constituents in the surface regions and the valence band structure of the sample.

2.3.2 Important parameters

Photoemission can be thought of as three steps: (i) photon absorption and ionization (initial state effects); (ii) response of atom and creation of photoelectrons

(final state effects); (iii) transport of electrons to surface. Mg Kα (1253.6 eV) or Al Kα (1486.6 eV) are usually used as the X-ray source. The X-ray penetrates into the sample to a distance of several μm. However, the depth related to the emission and detection of photoelectrons is much less, due to the small escape length of ejected photoelectrons. Only those electrons originated within tens of angstroms below the solid surface can escape the surface. The probability that electron of kinetic energy E_{kin} will arrive at surface without energy loss is strongly dependent on the inelastic mean free path (IMFP), a measure of the average distance traveled by an electron before it is inelastically scattered,

$$I = I_0 exp\left(-\frac{d}{\lambda cos(\theta)}\right), \tag{2.13}$$

where θ is the takeoff angle. For $cos(\theta) = 1$, it is estimated that 63.3% of the photoelectrons are originated from within 1λ of surface. Virtually most (~ 95%) of the electrons detected come from with 3λ of the surface.

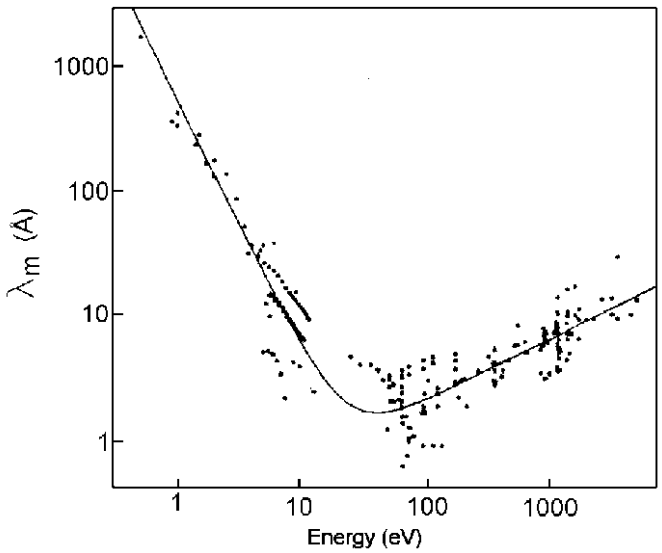

Figure 2.9: The inelastic mean free path (IMFP) as a function of kinetic energy for various solid elements [18].

The IMFP depends on two factors: the kinetic energy of the electron and the nature of the sample. Fig 2.9 shows λ as a function of electron kinetic energy for various elements [18]. The full line is a result of an empirical least squares fit. The IMFP can be very high for kinetic energies below 50 eV, and a strong dependence on material and geometry in this range is shown. Above 100 eV the IMPF increases steadily as a function of electron kinetic energy. For energies above 150 eV, the IMFP is given approximately by $\lambda \sim 0.522\sqrt{E_{kin}}$.

XPS measurement gives a relative quantification of surface concentration. The detection limitation of XPS for a specific element with an atomic number (Z > 2) in the sample is at the range of 0.1% - 1%. Different elements have different detection sensitivity. The number of photoelectrons in a spectra peak for an element is given by:

$$I = nf\sigma\theta y\lambda AT, \tag{2.14}$$

where n is the average atomic concentration of the element in the surface under analysis, f is the X-ray flux, σ is the photoelectron cross-section, θ is the angular efficiency factor based the angle between the photon path and the detected electron, y is the efficiency for the formation of photoelectrons of the normal photoelectron energy, λ is the inelastic mean free path, A is the analysis area, and T is the detection efficiency for electrons emitted from the sample. A general expression for determining the atom fraction of any constituent in the scanned region of a sample can be expressed as

$$C_x = \left(\frac{I_x}{S_x}\right) / \left(\sum \frac{I_i}{S_i}\right), \tag{2.15}$$

where I_x and S_x are the peak area and the atomic sensitivity factor of element x, respsectively.

In XPS, the energy resolution ΔE is related to both the electron energy analyzer and the X-ray source, apart from the intrinsic contribution from each element. The energy resolution of certain peaks can be expressed as

$$\Delta E = \left(\Delta {E_n}^2 + \Delta {E_p}^2 + \Delta {E_a}^2\right)^{1/2}, \quad (2.16)$$

where ΔE_n is the intrinsic line width of the orbital of the atom, ΔE_p is the line width of the X-ray source, and ΔE_a is the width of the energy analyzer window. ΔE_n is fixed and ΔE_a can be adjusted. In most cases, the resolution is controlled by the line width of the X-ray line ΔE_p. The efficient way to narrow down the width is to use a monochromator. Another way to achieve better resolution is to replace the conventional sources with the synchrotron X-ray sources.

There are several kinds of feature peaks in XPS spectra. In this section, three types of main feature lines in XPS spectra will be briefly introduced.

(a) Photoelectron lines: the most intense peaks observed are photoelectron lines, including the core-level lines and the valence-band lines.

(b) Auger lines: these peaks are from X-ray induced Auger electron emission. Four main Auger lines observed in XPS spectra are: *KLL*, *LMM*, *MNN*, and *NOO*.

(c) Shake-Up/Shake-Off lines: There is a finite probability that an ion will be left in a specific excited state with a few eV above the ground sate, in a photoionization process. The kinetic energy of the emitted photoelectron is reduced. This results in the formation of a satellite peak with a few eV higher binding energy than the main line. These satellite lines are denoted as shake-up or shake-off lines, representing the excitation of electrons to bound or unbound states, respectively.

From the photoelectron binding energy, XPS can identify almost all the elements in the periodic table, except H and He. For a compound material, the binding energy of an electron depends on the local chemical and physical state of the atom.

2.3.3 XPS and UPS instrumentation in this study

The XPS system used in this study is VG ESCALAB 220i-XL, the photo of which is shown in Fig 2.10. It consists of an X-ray gun in the UHV chamber, a monochromator, an ion sputtering gun, a flood electron gun, and an energy analyzer. The XPS spectrometer was calibrated with pure nickel, gold silver and copper by setting Fermi edge. The best energy resolution of this XPS system is about 0.45 eV, and the accuracy of the observed binding energies on an absolute scale is within 0.02-0.03 eV after careful calibration.

The UPS system used is in the SSLS (Singapore Synchrotron Light Source), NUS. The synchrotron radiation at the SSLS is provided from the compact storage ring Helios 2 built by Oxford Instruments. The UPS experiments are performed in an UHV end-station (base pressure 1×10^{-10} torr). Valence spectra are acquired with photon energy of 60 eV. E_f is determined by a Fermi edge cut-off from a multilayer Au film. In this thesis, UPS is used to determine the band gap state and study surface point defects interaction with O_2 gas.

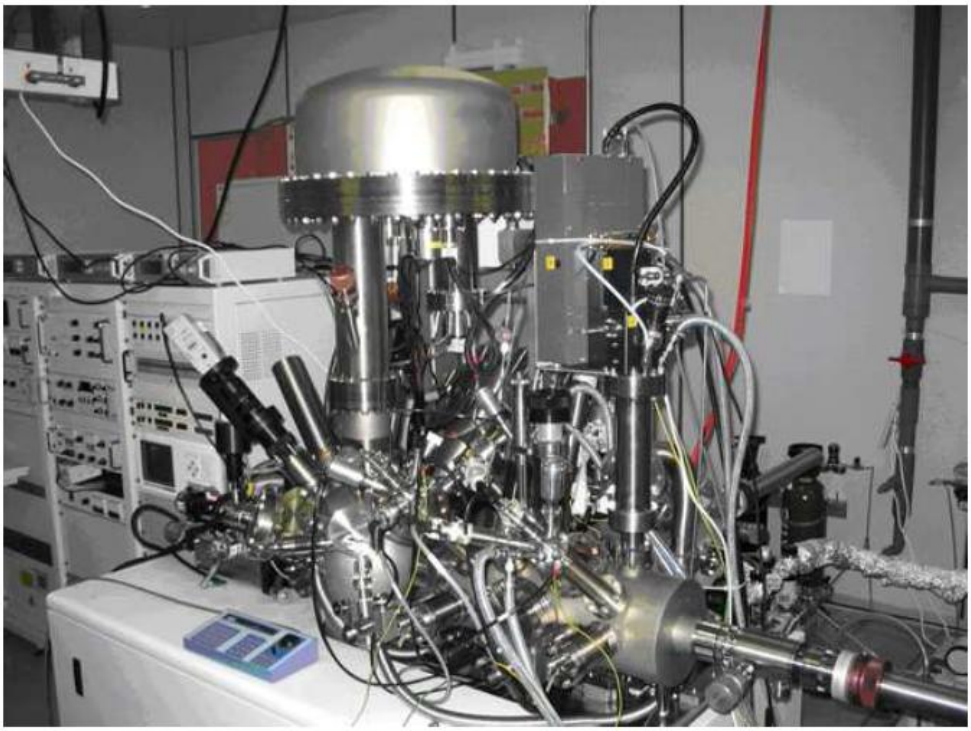

Figure 2.10: Photograph of the VG ESCALAB 220i-XL XPS system.

2.4 First-principles calculation methods

2.4.1 Density functional theory

Besides experimental works, we study the material properties using *ab initio* techniques. We used density functional theory (DFT) in all calculations described in this work.

DFT is based on the well known Hohenberg-Kohn theorem [19] that the total energy of a system can be viewed as a functional of its ground state density. This theory allows for the description of the many-body problem of interacting electrons in a static external potential, in terms of electron density as the basis variable. Since its

introduction in the mid 1960s and early 1970s, it has been extensively used in physics and chemistry for various calculations [20-22].

Hohenberg-Kohn theorem states that there exist a universal functional of the density, independent of the external potential, such that the global minimum value of the energy functional is the exact ground state energy of the system and the exact ground state density minimizes this functional. The ground state energy is determined by the ground state density $n_o(\vec{r})$, which is described as,

$$E[(n(\vec{r})] \equiv < \Psi[n_0(\vec{r})]\left|\hat{H}\right|\Psi[n_o(\vec{r})] >$$

$$= < \Psi[n_0(\vec{r})]|T + V_{ext} + V|\Psi[n_o(\vec{r})] > , \qquad (2.17)$$

where T is the kinetic energy, V_{ext} is the external potential, and V is related to the two-body electron-electron interaction. By minimizing the total energy functional with respect to variations in the density, the ground sate density and energy can be found.

It is the Kohn and Sham who put Hohenberg-Kohn theorem into practical use. Kohn was honored with the Nobel Prize in chemistry in 1998. The Kohn-Sham ansatz is to replace the many-electron problem by an exactly equivalent set of self-consistent one electron equations [23]. For a set of doubly occupied electronic states Ψ_i, the Kohn-sham total energy functional can be written as,

$$E[\{\Psi_i\}] = 2\sum_i \Psi_i \left[-\frac{\hbar^2}{2m}\right]\nabla^2\Psi_i d^3\vec{r} + V_{ion}(\vec{r})n(\vec{r})d^3\vec{r}$$

$$+\frac{e^2}{2}\int\frac{n(\vec{r})n(\vec{r}')}{|\vec{r}-\vec{r}'|}d^3\vec{r}d^3\vec{r}' + E_{xc}[n(\vec{r})] + E_{ion}(\{\vec{R}_I\}), \qquad (2.18)$$

where V_{ion} is the static total electron-ion potential, $E_{xc}[n(\vec{r})]$ is the exchange-correlation functional, E_{ion} is the Coulomb energy associated with the nuclei (or ions) at positions $\{\vec{R}_I\}$, and $n(\vec{r})$ is the electron density,

$$n(\vec{r}) = 2\sum_{i=1}|\Psi_i(\vec{r})|^2, \qquad (2.19)$$

which is subject to the conservation condition:

$$\int n(\vec{r})d\vec{r} = N. \tag{2.20}$$

At the minimum, the Kohn-sham energy functional is equal to the ground-state energy of the system. The set of wave functions that minimize the Kohn-Sham energy functional needs to be determined. For a system with N independent electrons, the ground state is obtained by solving the Kohn-Sham equations [23]:

$$\left[-\frac{\hbar^2}{2m}\nabla^2 + V_{KS}(\vec{r})\right]\Psi_i(\vec{r}) = \mathcal{E}_i\Psi_i(\vec{r}), \tag{2.21}$$

where $\Psi_i(\vec{r})$ is the wave function of each electronic state, and $\mathcal{E}_i$ is the Kohn-Sham eigenvalue.

$$V_{KS}(\vec{r}) = V_{ion}(\vec{r}) + V_H(\vec{r}) + V_{xc}(\vec{r}), \tag{2.22}$$

where $V_H(\vec{r})$ is the Hartree-Fock potential, given by

$$V_H(\vec{r}) = e^2 \int \frac{n(\vec{r}')}{|\vec{r}-\vec{r}'|} d^3\vec{r}', \tag{2.23}$$

and $V_{xc}(\vec{r})$is the exchange-correlation potential, which is given by the derivative

$$V_{xc}(\vec{r}) = \frac{\delta E_{xc}[n(\vec{r})]}{\delta n(\vec{r})}. \tag{2.24}$$

The Kohn-Sham ansatz successfully maps the interacting many-body system onto a set of independent single-particle equations. The Kohn-Sham equations must be solved self-consistently. The process starts with an initial electron density, then the effective potential is calculated. At each step, the solution gives the wave functions, from which one can calculate the electron density. Based on the new electron density, the effective potential is updated. Such process is repeated until the desired accuracy is reached.

2.4.2 Local density approximation

Although exact in principle, the Kohn-Sham theory is approximate in practice because it is impossible to calculate the exact exchange-correlation potential by

solving the many-body problem exactly. It is crucial to have accurate exchange-correlation energy functional or potential, for the purpose to obtain a satisfactory description of a realistic system.

In the local density approximation (LDA), the exchange-correlation energy per electron is the same as that for a homogeneous electron gas (HEG) that has the same electron density. The total exchange-correlation energy $E_{xc}[n(\vec{r})]$ can be written as,

$$E_{xc}^{LDA}[n(\vec{r})] = \int n(\vec{r})\varepsilon_{xc}^{hom}(n(\vec{r}))d\vec{r}, \tag{2.25}$$

where the exchange-correlation energy density ε_{xc}^{hom} is a function of the electron density alone, which can be decomposed into the exchange energy density and the correlation energy density separately. The exchange energy density of the unpolarized HEG was introduced by Dirac [24],

$$\varepsilon_X^{hom}\big(n(\vec{r})\big) = -\frac{3}{4}\left(\frac{3}{\pi}\right)^{1/3} n(\vec{r})^{1/3}. \tag{2.26}$$

Analytic expressions for the correlation energy of the HEG are sophisticated. Corrections to the exchange-correlation energy due to the inhomogeneity in the electronic density are ignored. However, LDA is proved to work reasonably well, even in the systems where the electron density is rapidly varying. In the mean time, it tends to underestimate ground state energies and ionization energies, while overestimating binding energies. The energy gaps within LDA show a large discrepancy with experiments for some semiconductors.

The inhomogeneous charge density needs to be considered in obtaining the exchange-correlation energy. This leads to the development of various generalized-gradient approximations (GGAs). The gradient corrected exchange-correlation energy is described as,

$$E_{xc}^{GGA} = \int n\,(\vec{r})\varepsilon_{xc}\big(n(\vec{r}), \nabla n(\vec{r})\big)d\vec{r}, \tag{2.27}$$

where ε_{xc} at $\vec{r}$ depends on the density and its gradient at positions $\vec{r}$.

GGA provides a better description of the electronic subsystem, which makes it generally works better than LDA, in predicting bond length, binding energy of molecules, lattice constants and so on. Three most widely used GGAs are the forms proposed by Perdew *et al*. [25], Becke (B88) [26], and Perdew, Burke and Enzerhof (PBE) [27].

Both LDA and GGA do not perform well in materials where electrons tend to be localized and strongly correlated. such as transition metal oxides, and rare-earth elements and compounds, with partially filled *d* or *f* shells. For example, LDA predicts transition metal oxides to be metallic, but instead, these transition metal oxides are Mott insulators. In order to properly describe these strongly correlated systems, orbital-dependent potentials should be used. For the purpose to incorporate the strong electron-electron correlations, there are several approaches developed, among which the LDA (and GGA) +*U* method is the most widely used.

In the LDA+*U* method, the electrons are separated into two classes: the delocalized *s*, *p* electrons, and the localized *d* or *f* electrons for which an orbital-dependent term $\frac{1}{2}U\sum_{i\neq j} n_i n_j$ should be used to describe Coulomb interaction, where n_i are orbital occupancies [28].

As a simple approximation, the total energy in LDA+*U* method is given as:

$$E_{tot}^{LDA+U} = E_{LDA} + \frac{1}{2}U\sum_{i\neq j} n_i n_j - \frac{1}{2}UN(N-1), \tag{2.28}$$

where *U* is screened Coulomb on-site parameter. The orbital energies are the derivatives of (eq. 2.28) with respect to the orbital occupations n_i:

$$\varepsilon_i = \frac{\partial E}{\partial n_i} = \varepsilon_{LDA} + U(\frac{1}{2} - n_i). \tag{2.29}$$

For occupied orbitals $(n_i = 1)$, the orbital energies are shifted by –*U*/2, and for unoccupied orbitals ($n_i = 0$), the shift is +*U*/2, resulting in lower and upper Hubbard

bands separated by *U*, which opens a gap at the Fermi energy. To construct a quantitatively sound calculation scheme, one needs to take into account properly the direct and exchange Coulomb interactions inside a partially filled atomic shell.

When applied to the transition metal and rare-earth metal compounds, the LDA+*U* method has provided descriptions in a reasonable agreement with experiments, not only for excited-state properties such as energy gaps, but also for ground-state properties. The main limitation of this method is that the *U* parameter is species and environment dependent. In calculations, it is varied until convergence with the experimental results.

The first-principles calculations based on DFT methods in this study is implemented in VASP (Vienna Ab-initio Simulation Package) [29-31] and CASTEP [32] (Cambridge Serial Total Energy Package) simulation programs. They perform *ab-initio* quantum-mechanical molecular dynamics (MD) simulations using Vanderbilt pseudopotentials [33] (or the projector augmented wave method [34]), and a plain wave basis set [35].

References

[1] L. I. Maissel, "Application of sputtering to the deposition of films," in L. I. Maissel and R. Glang (eds.), *Handbook of Thin film technology*, pp. 4-44, McGraw-Hill, New York (1970).

[2] S. Rossnagel, "Sputtering and sputtering deposition," in K. Seshan (eds.), *Handbook of thin film deposition processes and technologies*, pp. 319-348, McGraw-Hill, New York (2002).

[3] R. Liu, "Metallization," in C. Y. Chang and S. M. Sze (eds.), *ULSI technology*, pp. 371-471, McGraw-Hill, New York (1996).

[4] R. Messier, A. P. Giri and R. A. Roy, "Revised structure zone model for thin-film physical structure," *J. Vac. Sci. Technol. A* **2**, 500-503 (1984).

[5] P. J. Kelly and R. D. Arnell, "Magnetron sputtering: A review of recent developments and applications," *Vacuum* **56**, 159-172 (2000).

[6] G. Binnig, C. F. Quate and C. Gerber, "Atomic force microscope," *Phys. Rev. Lett*. **56**, 930-933 (1986).

[7] R. V. Lapshin, "Automatic lateral calibration of tunneling microscope scanners," *Review of Scientific Instruments* **69**, 3268–3276 (1998).

[8] F.J. Giessibl, "Advances in atomic force microscopy," *Rev. Modern Phys.* **75**, 949-983 (2003).

[9] R. Berger, H. -J. Butt, M. B. Retschke and S. A. L. Weber, "Electrical modes in scanning probe microscopy," *Macromol. Rapid Commun*. **30**, 1167-1178 (2009).

[10] M. A. Lantz, S. J. O'Shea and M. E. Welland, "Characterization of tips for conducting atomic force microscopy in ultrahigh vacuum," *Rev. Sci. Instrum*. **69**, 1757-1764 (1998).

[11] M. Nonnemmacher, M. P. O'Boyle and H. K. Wickramasinghe, “Kelvin probe force microscopy,” *Appl. Phys. Lett*. **58**, 2921-2923 (1991).

[12] W. Melitz, J. Shen, A. C. Kummel and S. Lee, “Kelvin probe force microscopy and its application,” *Surf. Sci. Rep*. **66**, 1-27 (2011).

[13] S. Sadewasser and T. Glatzel (eds.), *Kelvin probe force microscopy: Measuring and compensating electrostatic forces*, Springer, Berlin (2012).

[14] B. Feuerbacher, B. Fitton and R.F. Willis (Eds.), *Photoemission and the electronic properties of surfaces*, Wiley, New York (1978).

[15] C. Westphal, “The study of the local atomic structure by means of X-ray photoelectron diffraction,” *Surf. Sci. Rep*. **50** 1-106 (2003).

[16] H. R. Hertz, "Ultra-violet light and electric discharge," *Ann. Physik* **31**, 983-1000 (1887).

[17] A. Einstein, “On a heuristic viewpoint concerning the production and transformation of light," *Ann. Physik* **17**, 132-148 (1905).

[18] M.P. Seah and W.A. Dench, “Quantitative electron spectroscopy of surfaces: A standard data base for electron inelastic mean free paths in solids,” *Surf. Interf. Anal.* **1**, 2-11 (1979).

[19] P. Hohenberg and W. Kohn, “Inhomogeneous electron gas,” *Phys. Rev.* **136,** B864-B871 (1964).

[20] M. C. Payne, M. P. Teter, D. C. Allan, T. A. Arias and J. D. Joannopoulos, “Iterative minimization techniques for *ab initio* total-energy calculations: molecular dynamics and conjugate gradients,” *Rev. Mod. Phys.* **64**, 1045-1097 (1992).

[21] P. L. Taylaor and O. Heinonen, *A quantum approach to condensed matter physics*, Cambridge University Press, Cambridge (2002).

[22] R. M. Martin, *Electronic structure - basic theory and practical methods*, Cambridge University Press, Cambridge (2004).

[23] W. Kohn and L. J. Sham, "Self-consistent equations including exchange and correlation effects," *Phys. Rev.* **140,** A1133-A1138 (1965).

[24] P. A. M. Dirac, "Note on exchange phenomena in the Thomas-Fermi atom," *Proc. Cambridge Phil. Roy. Soc*. **26**, 376-385 (1930).

[25] J. P. Perdew, J. A. Chevary, S. H. Vosko, K. A. Jackson, M. R. Pederson and C. Fiolhais, "Atoms, molecules, solids, and surfaces: Applications of the generalized gradient approximation for exchange and correlation," *Phys. Rev. B* **46**, 6671-6687 (1992).

[26] A. D. Becke, "Density-functional exchange-energy approximation with correct asymptotic behavior," *Phys. Rev. A* **38**, 3098-3100 (1988).

[27] J. P. Perdew, K. Burke and M. Ernzerhof, "Generalized gradient approximation made simple," *Phys. Rev. Lett*. **77**, 3865-3868 (1996).

[28] V. I. Anisimov, F. Aryasetiawan and A. I. Lichtenstein, "First-principles calculations of the electronic structure and spectra of strongly correlated systems: The LDA+*U* method," *J. Phys. Condens. Matter* **9**, 767-808 (1997).

[29] G. Kresse and J. Hafner, "*Ab initio* molecular dynamics for open-shell transition metals," *Phys. Rev. B* **48,** 13115-13118 (1993).

[30] G. Kresse and D. Joubert, "From ultrasoft pseudopotentials to the projector augmented-wave method," *Phys. Rev. B* **59**, 1758-1775 (1999).

[31] G. Kresse and J. Furthmuller, "Efficiency of *ab-initio* total energy calculations for metals and semiconductors using a plane-wave basis set," *J. Comput. Mater. Sci*. **6,** 15-50 (1996).

[32] M. D. Segall, P.L. D. Lindan, M. J. Probert, C. J. Pickard, P. J. Hasnip, S. J. Clark and M. C. Payne, "First-principles simulation: ideas, illustrations and the CASTEP code," *J. Phys.: Condens. Matter* **14,** 2717-2744 (2002).

[33] D. Vanderbilt, "Soft self-consistent pseudopotentials in a generalized eigenvalue formalism," *Phys. Rev. B* **41**, 7892-7895 (1990).

[34] P. E. BlÖchl, "Projector augmented-wave method," *Phys. Rev. B* **50**, 17953-17979 (1994).

[35] http://cms.mpi.univie.ac.at/vasp/

Chapter 3

The Resistive Switching in TiO_2 Films Studied by CAFM and KPFM

3.1 Introduction

Since the invention of scanning probe microscopy (SPM), scanning-probe based measurements have been widely used for nano-scale surface investigations. Using

SPM, a range of morphological, electrical and mechanical information of a sample can be obtained. This convenience has made SPM one of the most frequently employed techniques in nano-scale characterizations. Conductive atomic force microscopy (CAFM) [1-7] and Kelvin probe force microscopy (KPFM) [8, 9] are two SPM techniques that are frequently used for filamentary and interfacial studies in resistive switching.

As a widely used technique in characterizing the local electrical properties across the surface, CAFM has been frequently adopted for localized conductivity study. Using CAFM, Muenstermann *et al*. studied a Pt/Fe:$SrTiO_3$/Nb:$SrTiO_3$ MIM structure [6]. They electroformed the device with a high electric breakdown process, due to the high insulating property of the as-deposited oxide thin film. They removed the top electrode through a delamination process before a CAFM measurement. After the electroforming process, a crater-like area a few μm wide was observed, with the remaining interface area smooth and not structurally altered. A much higher current is shown in the crater area, compared with the low current in the surrounding area. They proposed a single-filament model to explain what they have observed.

Similarly, Choi *et al*. studied high insulating TiO_2 thin films using two AFM systems operated under atmospheric pressure and high vacuum respectively [7]. They firstly fabricated Al/TiO_2/Ru sandwiched structures, then switched the devices to high and low resistance states after an initial electroforming process. Then the top electrode was etched away for the following AFM measurements. Conducting spots attributed to conductive filaments formed were observed. Through formation and elimination of conducting spots, the device worked at different resistance states. In their report, a few filaments were found to be randomly distributed.

KPFM is a widely used tool to measure the local contact potential difference between AFM tip and the sample [8-11]. Mapping of the work function or surface potential of the sample with high spatial resolution can be achieved by this technique. As one of the frequently discussed switching mechanisms in the literature, the charging effect in a switching process may result in different resistance states due to a change of potential barrier for current flow. Using KPFM, Chen *et al*. studied an Ag–PCMO–Ag surface [8]. Based on the surface potential map, they concluded that 98% of the resistance switching occurred in the interface regions within the metal/oxide contact.

The filament model suggests that the filament size determines the ultimate scaling limit, and a high density of filaments is necessary for integrated memory devices. For this purpose, the fabrication of an insulating film followed by a high electrical field breakdown process has great limitations. The metal/oxide interface damages (and residues) produced through an etching removal process makes it difficult in a CAFM analysis. It is possible to deposit oxide thin films with enhanced conductivity by changing the deposition conditions. In comparison to insulating films, the study of resistive switching in an oxide thin film with good conductivity is rarely reported. With oxide thin films deposited on a metal, the metallic SPM tip serves as a nano-size electrode in the switching MIM structure, and a surface area comparable with the tip size can be studied.

Although the microscopic mechanisms in resistive switching are still under intensive debate, the migration of oxygen ions under an electrical field is widely accepted to play a key role [5, 12-18]. Electro-migration of oxygen ions leads to oxidation and redox reactions in the oxide matrix, and different resistance states are then formed. The so-called filament model can be simply treated as a filament

formation and rupture process. On the other hand, the interface between metal and oxide is also extensively investigated, and frequently attributed to perform a critical function in the switching process [8, 16-21].

In this chapter, TiO_2 thin films with enhanced conductivity were successfully fabricated and high density nano-size filaments were achieved. The resistive switching characteristics are investigated using CAFM and KPFM techniques. We used CAFM to write and read a local TiO_2/Pt surface and analyzed the switching mechanism involved. KPFM was used to probe the sample surface potential after an electrical writing process. Finally, an integrated model combined with both filamentary and interfacial effects was proposed to elucidate the observed phenomenon.

3.2 CAFM modification of the thin film conductivity

The 20 nm thick TiO_2 films were deposited on a Pt/Ti/SiO_2/Si substrate by RF magnetron sputtering from a TiO_2 target, with Ar flow rate at 30 sccm (standard cubic centimeters per minute), RF power at 250 W. The as-deposited films illustrate good conductivity and an initial high voltage breakdown step is not needed. A commercial atomic force microscope operated in ambient air, with a Pt coated silicon cantilever (radius of 15 nm, with a spring constant of 2 N/m, and a resonant frequency of 70 kHz) is used for measurements. A sketch of the thin film stack structure and the CAFM measurement setup is shown in Fig 3.1. Figs 3.2 (a) and (b) show the XRD spectrum and the cross-sectional HRTEM image of the stacked structure respectively. The TiO_2 thin films are in an amorphous state as only the peaks of the Si substrate and the Pt layer can be seen in the XRD pattern.

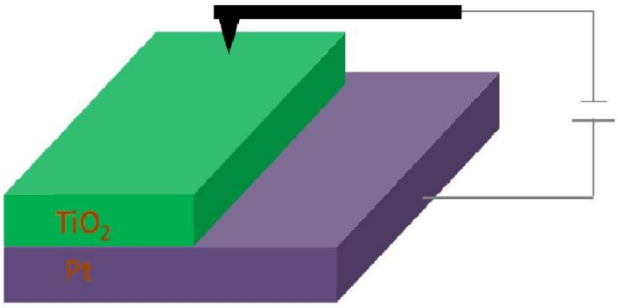

Figure 3.1: Schematic diagram of the CAFM measurement setup.

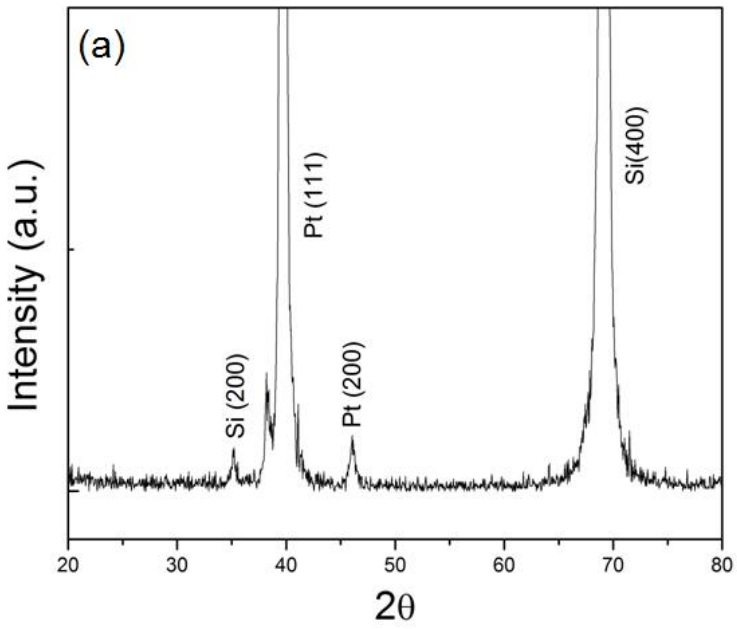

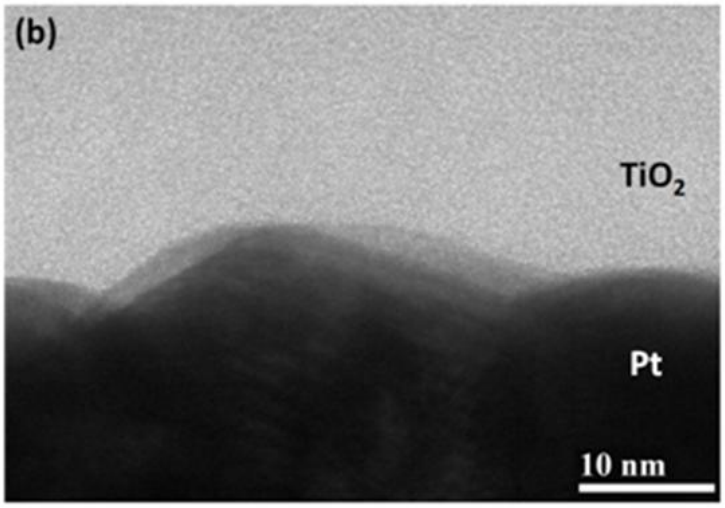

Figure 3.2: (a) XRD spectrum of the sample. (b) High-resolution TEM image of a TiO_2/Pt junction.

Using the CAFM system, we applied a +/- 5V bias on an area of $2.0 \times 2.0\ \mu m^2$ at 1 Hz in contact mode. All current mapping images were obtained with the cantilever moving across the thin film surface. With a positive bias, a more conducting surface was observed, while a more insulating surface was observed for a negative bias (Fig 3.3). A variation of between two to three orders of magnitude in current flow is observed. No significant change in topography (Fig 3.3(a)) is observed in the current mapping process. Under a positive bias of +5 V, a large number of nano-size conducting spots are observed (see Fig 3.3(b)). The observed spots mark the conducting paths that connect the surface with the bottom electrode (BE). The current mapping of the same area in 3D is shown in Fig 3.3(c). These conducting spots are distributed across the scanned area. The presence of the conducting spots is consistent with the widely accepted filament model for resistive switching [1-7, 16-18]. Each conducting spot shown in Figs 3.3(b) and 3.3(c) may correspond to one filament formed beneath. The conducting nanofilaments could come from oxygen deficient Magnéli phases [22, 23], or metallic atom chains [24, 25] formed in the bulk oxide. The large distinction between the states under different biases could be explained by the electro-migration of oxygen ions. Reduction and oxidation reactions may take place, and the resistance state goes to a lower or higher level respectively. Through oxidation and redox reactions, each filament [26] could act as a resistive switching unit.

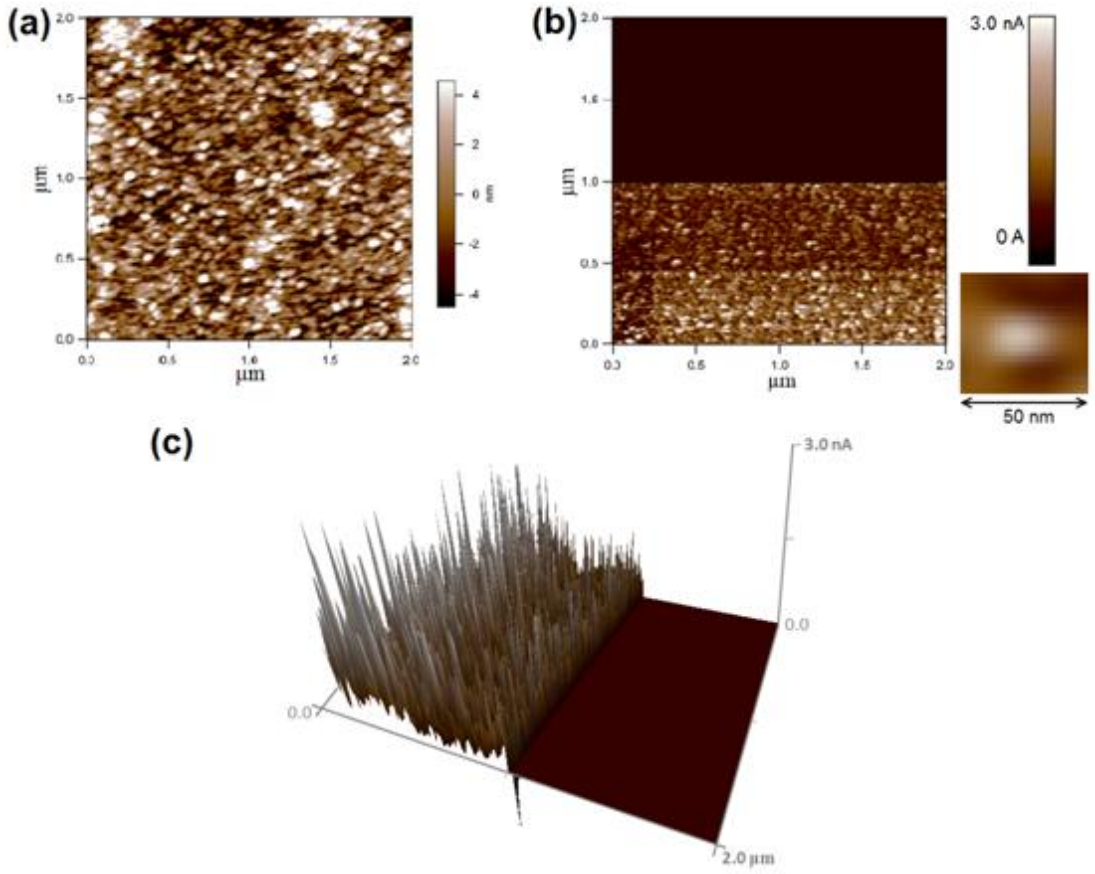

Figure 3.3: CAFM mediated surface conductivity modifications of the TiO_2 thin film. (a) Topography (b) More conducting and more insulating (than native surface) surface obtained by CAFM sweeping using -5 V (upper region) and 5 V biases (lower region). One conducting spot is shown on the lower right corner. (c) Current mapping images in 3D of the same area.

Fig 3.4 shows CAFM current mapping images of an area of $5.0 \times 5.0\ \mu m^2$ for a TiO_2 thin film under different bias voltages. By applying a negative bias (0 to -4.5 V), the current is kept at a low level (~ 10^{-12} - 10^{-10} A), as shown in Fig 3.4(a). Fig 3.4(b) shows the CAFM measurements by applying a positive bias (0 to 4.5 V). There is no significant change in the measured current until the voltage is increased to 1.5 V, after which conducting spots with high current start to appear. Localized redox reactions lead to condutive filaments formed in the oxide. Fig 3.4(c) shows 3D image of the same scan. The density of filaments increased with the voltage, indicating more filaments are formed at a higher voltage.

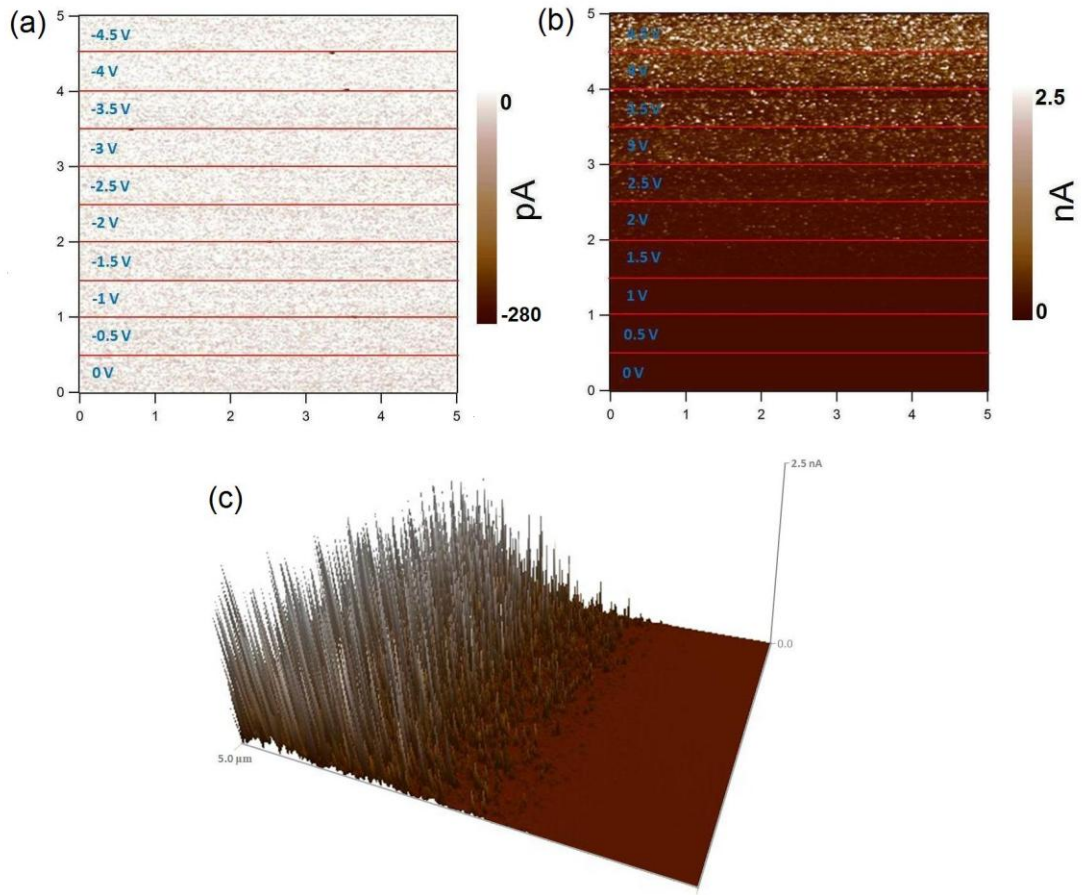

Figure 3.4: CAFM current mapping image under different bias voltages. (a) 0 to -4.5 V. The current kept between 10^{-12} - 10^{-10} A (-), except for a few points for a much higher current. (b) 0 to 4.5 V. The current increased with the voltage, up to 2.5 nA (+). (c) 3D current image of (b).

Compared with the filaments formed at lower voltages, improved conductivity was found for the filaments formed under a higher voltage. This could be due to the formation of more oxygen deficient TiO_2 phases when a higher voltage was applied. Fig 3.5(a) shows the CAFM measurements by applying 2 and 3 V (Fig 3.5(b) shows the 3D image).

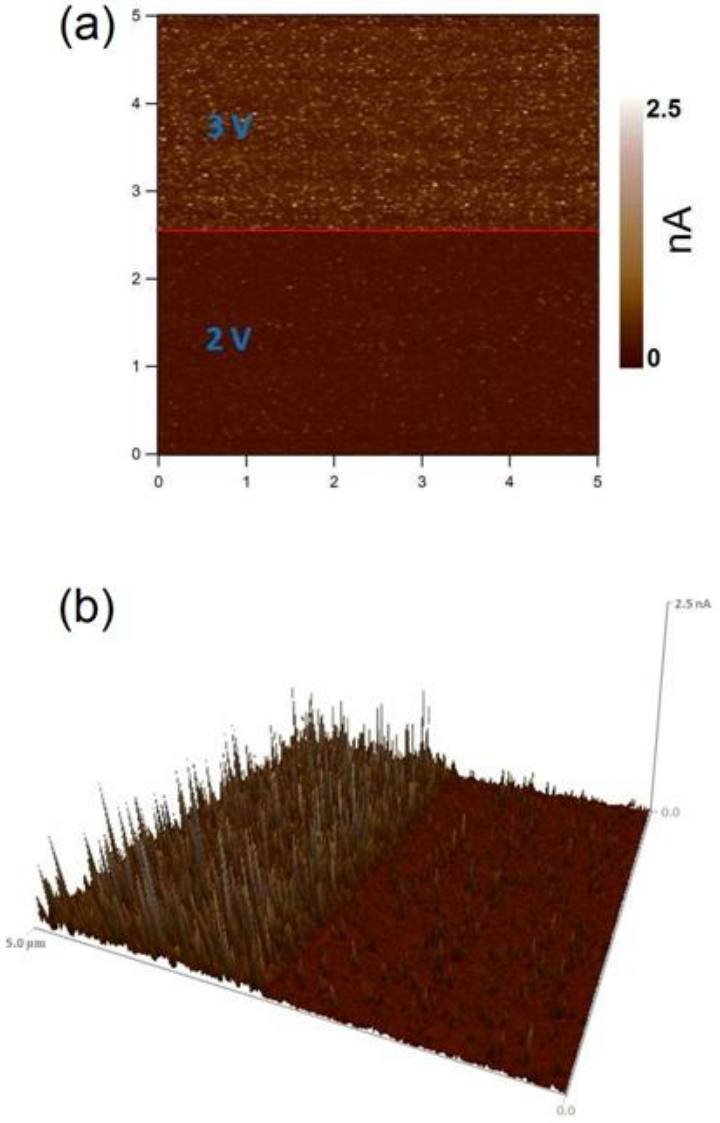

Figure 3.5: CAFM current mapping image under different bias voltages. (a) 2 V to the lower area and 3 V to the upper area. (b) 3D current image.

In comparison to a positive bias, a much higher negative voltage bias is needed to form conductive filaments in the oxide film. The application of a high voltage will lead to an electrical breakdown. Fig 3.6 shows a contrast between breakdown and non-breakdown, with -10 V on the upper area and -5 V on the lower area. Fig 3.6(a) shows the topography image and Fig 3.6(b) shows the 3D current image of the same area, respectively. Significant changes were found in the oxide thin film after a high electrical breakdown process. The current compliance was set at 10 nA.

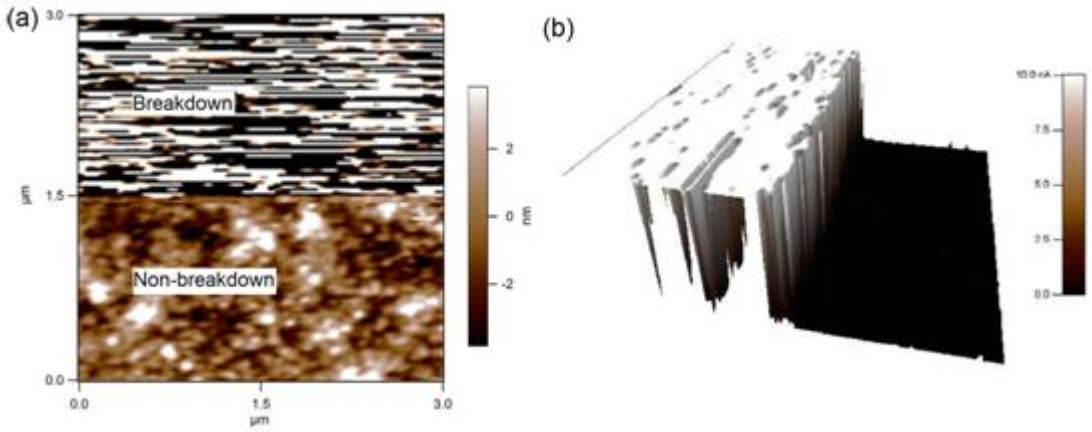

Figure 3.6: A contrast between breakdown and non-breakdown. (a) topography image; (b) 3D CAFM current image.

3.3 KPFM measurement of the surface potential

To investigate the surface potential change under an applied electric field, KPFM studies were performed with a Pt coated silicon cantilever (the same as the CAFM tip). The measurement setup is shown in Fig 3.7(a). A selected surface area was firstly scanned with different electrical bias applied on the Pt tip, that is, +/- 5 V respectively. KPFM measurements were conducted subsequently in the same area by applying an ac voltage of 3 V at a lift height of 40 nm. Fig 3.7(b) shows the black and white contrasts of the surface area scanned under negative and positive electrical biases, respectively. The positive bias produces an area with a higher surface potential than the negative bias. This is attributed to the injection of negative charges in the upper region under a negative bias, and the creation of positive charges in the lower region under a positive bias. In this study, the surface potential at the unbiased region is set to 0 V for a better comparison.

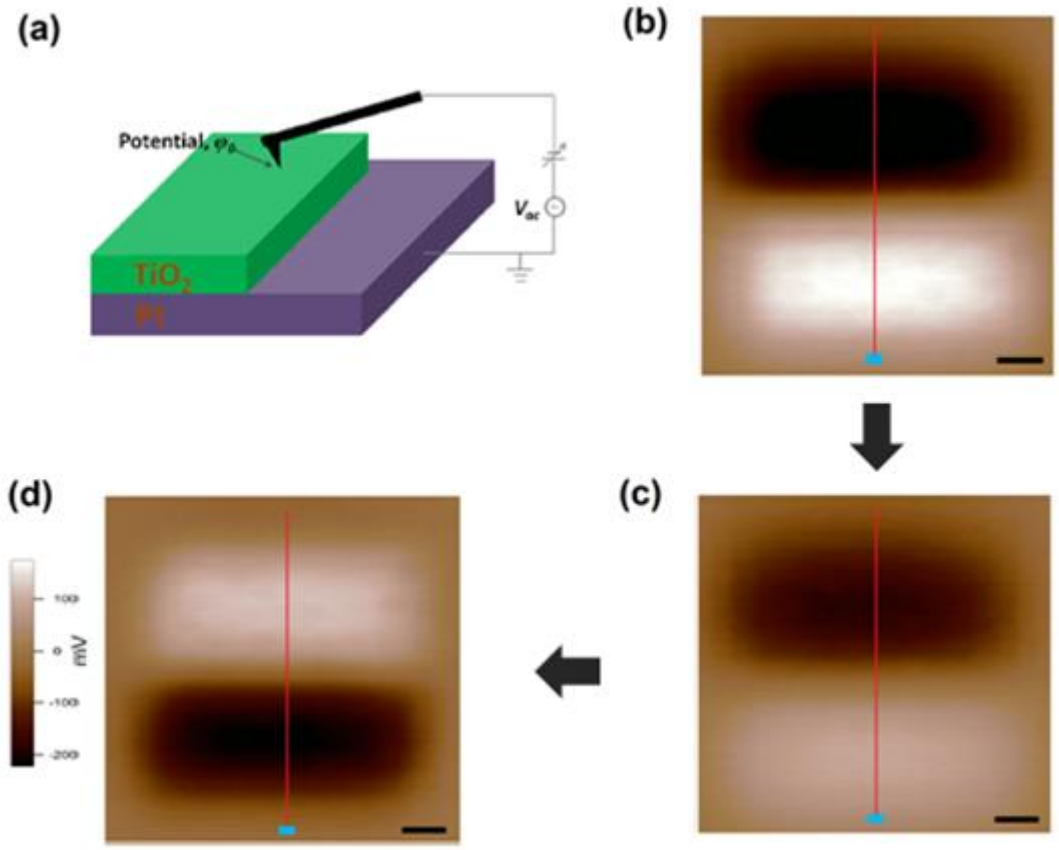

Figure 3.7: (a) The KPFM measurement setup. (b) KPFM surface potential distribution of the TiO_2 thin film. The area is scanned with the tip under a bias of -5 V on the upper region and 5 V on the lower region in contact mode. (c) and (d) KPFM surface potential distribution images of the same charged regions: (c) after surface grounded-tip scan; (d) after a bias of 5 V applied to the upper region and -5 V on the lower region respectively. The scale bars represent 0.5 μm.

As shown in Fig 3.7(b), the centre area in each zone demonstrates a much higher charge density compared with the surrounding areas and a region of charge neutrality is found at the boundary regions between the two different charge zones due to the migration of the injected charges from centre to outer area with the electrical field applied. At the boundary between the two zones, the negative and the positive charges form an area of neutrality. The potential profile across the charged zones is shown in Fig 3.8 (the black dotted line). A maximum surface potential of -0.22 V is obtained for the negative charge zone, compared to 0.17 V for the positive zone, implying a

higher density of negative charges at the negative region. This shows that the injection of negative charges could be more efficient than the creation of positive charges.

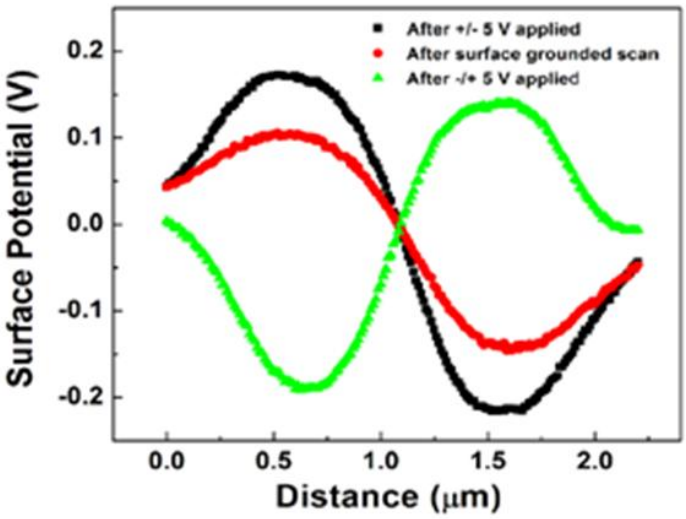

Figure 3.8: Surface potential profiles obtained based on the line (red) scans across the poling area, as shown in Figs 3.7 (b)-(d).

The stability of the surface charges induced by the electrical biases was investigated by scanning the same surface area, with the grounded Pt coated tip, in contact mode. Fig 3.7(c) shows the KPFM surface potential images after such a process. Both the negative and the positive charge densities decreased, with the maximum surface potential dropping to -0.14 V for the negative area and 0.10 V for the positive area respectively (Fig 3.8, the red dotted line). This process is to eliminate the free (and shallow-trapped) carriers in the top surface region. A significant drop was found in the positively charged area. A positive voltage may produce a large amount of charged oxygen vacancies in the surface region, by extracting oxygen ions from the lattice. Oxygen vacancy is a common defect in metal oxide materials. When the grounded tip is in contact at a specific spot, the positively charged oxygen vacancies tend to acquire electrons to become a neutralized state, causing the measured surface potential to show a significant change.

For the negative charge state, we attribute it to the injection of negative oxygen ions at the defect sites, in addition to electron injection into the oxide surface under a negative electrical bias. These two sources of negative charges together contribute to the high density of charged states in this region. In comparison to electron injection, the injection of negative oxygen ions at the defect sites could lead to a more stable state. The release of trapped electrons occurs when the tip is in contact at the spot, while it is more difficult for a detrapping process of trapped oxygen ions. It is proposed that a structure composed of oxygen interstitials could be formed after oxygen molecular ions were trapped at oxygen vacancies [27].

Under a positive bias, oxygen vacancies are formed, expressed in the Kröger-Vink notation

$$O_O^{\times} \rightarrow V_O^{\cdot\cdot} + \frac{1}{2}O_2 + 2e. \quad (1)$$

Negatively charged oxygen ions are then formed and dragged to the TE (Pt tip contact) and eventually ejected to air through a discharging process ($O^{2-} \rightarrow \frac{1}{2}O_2(g) + 2e$). Under a negative bias voltage, oxygen ions are injected into the lattice and the oxidation reaction results in a more insulating state.

The switching of the surface potential states can be realized by applying different electrical biases to the negative and positive charge regions separately. Fig 3.7(d) shows the surface potential distribution after a 5 V bias was applied to the upper region and a -5 V bias was applied to the lower region, for the same surface area after the grounded scan process. In comparison to that shown in Fig 3.7(b), a positive surface potential is observed in the upper region, while a negative potential is shown in the lower region. The surface potential profile is shown in Fig 3.8 (the green dotted line).

The decay of charges as time was also investigated. Fig 3.9(a) shows the surface

potential image after the application of +/- 5 V to a TiO_2 sample. The sample was then exposed to the air. Fig 3.9(b) shows the surface potential image for the same area after 16 hours. The surface potential for both regions were found to drop significantly during such a process, due to charge exchanging between the sample and the environment.

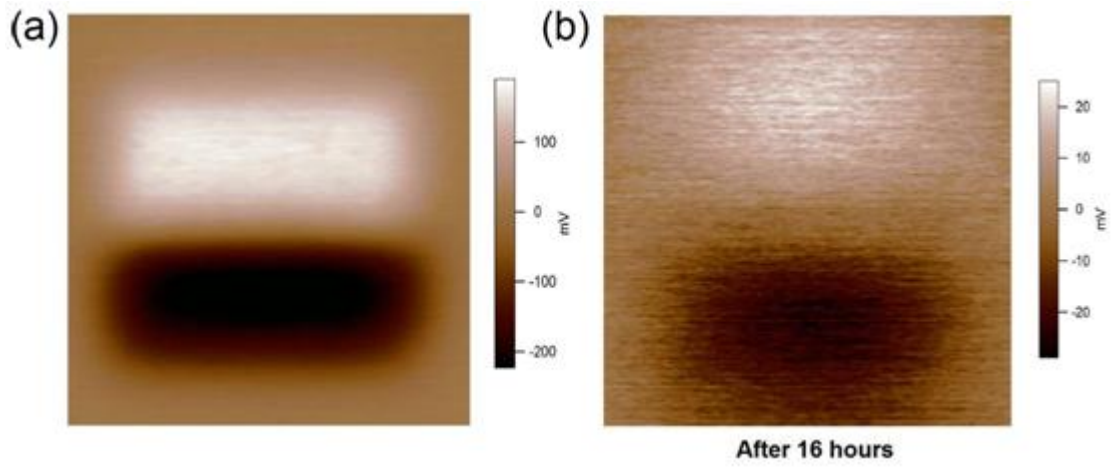

Figure 3.9: KPFM potential image of a TiO_2/Pt thin film: (a) immediate after +/-5 V applied; (b) after 16 hours exposing to the air.

For the region composing of positive charges, oxidation reactions between environment oxygen and surface oxygen vacancies take place. As a result, the density of the surface positive charges was dramatically reduced. Diffusion of trapped charges from the sub-surface to the top-surface could take place. For the region with negative charges, the release of negative charges occurred. The concentration of O^{2-} is both time and location dependent. The gradient of oxygen ions is the driving force behind their diffusion. The diffusion coefficient is given by,

$$D = D_0 \cdot exp(-E_a/kT), \quad (2)$$

where D_0 is a constant, and E_a is the activation energy of the oxygen diffusion.

3.4 The proposed switching mechanism

The KPFM measurements show charge injection and release into different surface potential states, which is consistent with the resistive switching mechanism proposed in the CAFM experiments. The behaviour shown in Figs 3.3 and 3.7 can be explained by the mechanism schematically shown in Fig 3.10, which we call a filament-interface model. Conducting filaments are formed in the oxide matrix, and an interfacial layer (IL) zone lies at the interface between TE and the bulk oxide. The filaments act as conducting bridges for current flow. The migration of oxygen ions under an electric field transfers the resistance state into a more insulating state and a more conductive state respectively. Pt is known for its electrocatalytic interaction with TiO_2 [28], and is reported to have good oxygen diffusivity [29]. The dislocations in the bulk oxide provide easy diffusion paths for oxygen [30, 31]. The migration of oxygen ions under an electric field mediates the switching process. Under the KPFM mode, a negative bias was applied for charge injection, followed by surface potential measurement. Negative oxygen ions are driven into the oxide surface layer (IL), and a high resistance state is formed, as shown in Fig 3.10(a). In comparison, Fig 3.10(b) shows the extraction of oxygen ions out of the IL zone. With the extraction of oxygen atoms from the local lattices, positively charged oxygen vacancies are created and the resistance state goes to a lower level.

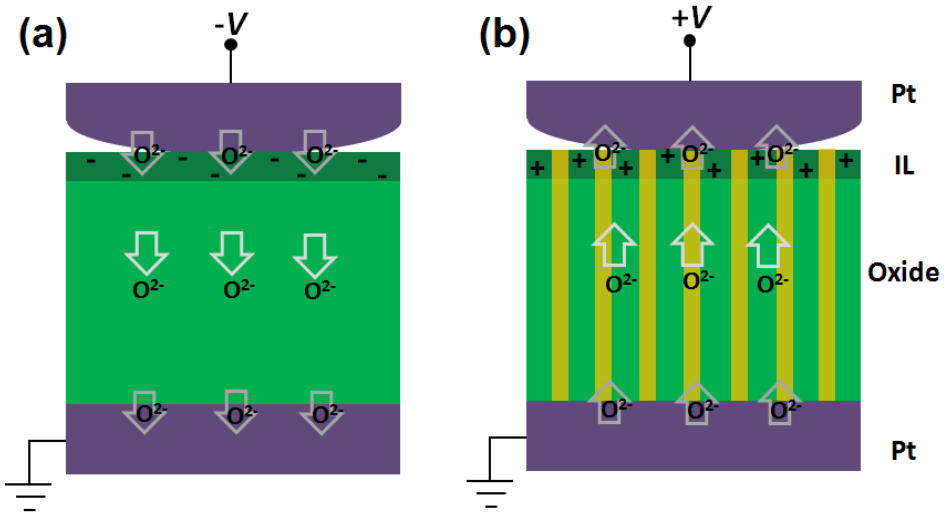

Figure 3.10: Schematic illustration of the conversion between a more insulating state and a more conductive state, and the oxygen movement under different bias polarities. (a) Oxygen ions are driven into the IL under a negative bias and a more insulating state state is formed. (b) Oxygen ions are driven out of the IL under a positive bias and a more conductive state is formed. The conducting filaments are formed in the bulk oxide. An interfacial layer (IL) zone lies at the interface between TE and the bulk oxide. The filaments are simply treated in a uniform shape.

With a positive electrical field applied to the AFM probe, multiple filaments are formed through an oxygen ion extraction process. Using the schematic model shown in Fig 3.11, we explain that observed in Fig 3.4. Increasing of the positive voltage leads to higher density of filaments formation in the oxide thin film (Fig 3.11(a)). In comparison, the application of a negative bias drives negative charges into the oxide thin film. Under an intermediate negative voltage, majority of the oxygen ions will pile up at the interface region, with a portion of the ions migrating out of the system through the defect sites in the oxide film. Fig 3.11(b) shows more negative charges are injected when increasing the negative bias voltage.

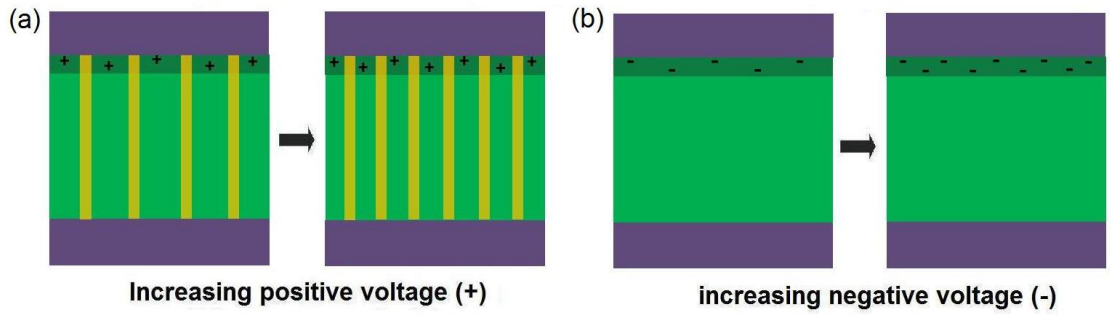

Figure 3.11: (a) Increasing of a positive bias voltage leads to more positive charges at the interface region, and higher density of filaments in the oxide. (b) Increasing of a negative bias voltage leads to more negative charges injection at the interface region.

3.5 Local current-voltage measurement

The tiny tip apex significantly concentrates the electric field around the tip-sample area. Fig 3.12 shows a typical current-voltage (I-V) characteristic of such a $Pt/TiO_2/Pt$ system, by positioning the Pt tip at an arbitrary location on the surface. The voltage was firstly increased from 0 under a negative bias. As the voltage increases, the current remained almost the same. A current jump was then observed when the voltage approached -10 V (compliance current was set at 10 nA) after a short current increasing stage. The current began to drop at ~ -6.5 V after a continuous scan with voltage decreasing from -10 V. The current emission dropped to a very low level at ~ -2.5 V during continuous scanning to a positive bias (up to ~ 2.5 V). The current started to increase again until a sudden drop occurred when the voltage approached 10 V. During this scan, a significant negative differential resistance (NDR) characteristic was observed at ~ 6.0 V. With voltage decreasing from 10 V, the current remained at a very low level (down to $\sim 10^{-12}$ A).

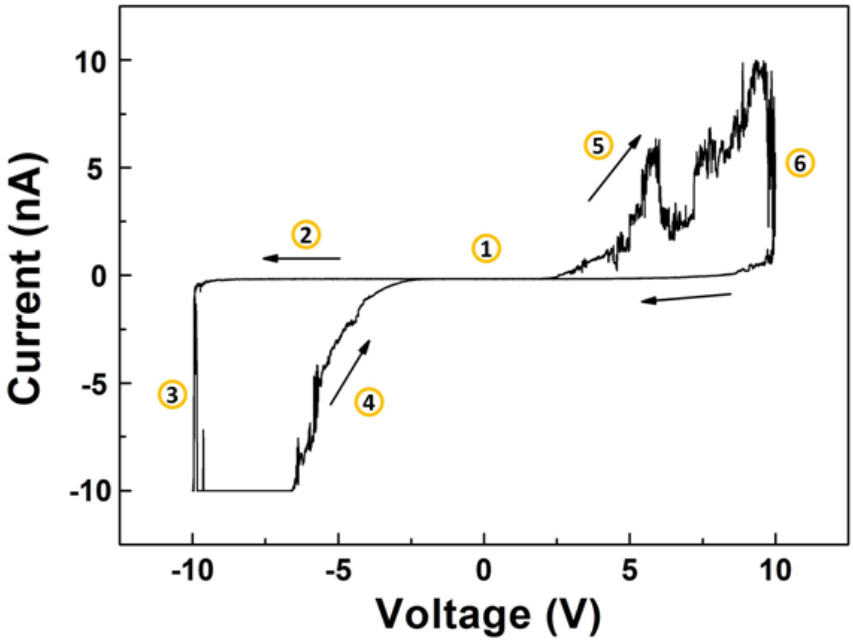

Figure 3.12: I-V characteristic measured by CAFM on a TiO_2/Pt surface, at a voltage sweep 0 → -10 V→ 0 → 10 V→ 0. Arrows indicate sweeping directions. The six circled numbers refer to the sweep stage at different voltages.

Charge injection and release assisted by electro-migration of oxygen ions results in different resistance states. Based on the mechanism proposed in Figs 3.10 and 3.11, the resistive switching illustrated in Fig 3.12 can be explained by the schematic model shown in Fig 3.13. Figs 3.13(a)-(f) refer to the six circled numbers, the sweeping of voltage at different stages. (i) Without an electrical field applied, the device structure is initially in a state shown in Fig 3.13(a). (ii) The application of negative voltages creates a negative charge zone at the interface (Fig 3.13(b)). (iii) When the bias is further increased to -10 V, an electrical breakdown takes place. The increase of current before the electrical breakdown could be due to heating effects or localized structure changes as a result of the high electrical field. Conductive filaments are then formed (Fig 3.13(c)). (iv) Oxidation of the filaments at the interfacial zone results in an insulating (or semiconducting) IL (Fig 3.13(d)). Electrons need to tunnel through the interfacial barrier with filaments as the conducting bridges. Oxygen ions are continuously injected into the IL regions. Modification of the IL zone conductivity

results in different resistance states. (v) Positive charges are created due to the extraction of oxygen ions under positive voltages (Fig 3.13(e)). An oscillation of current is observed at higher voltages. The extraction of oxygen ions from the IL could be accompanied by the injection of oxygen ions from the other side. The observed NDR phenomenon is due to the injection of oxygen ions (exceeding the extraction of oxygen ions at the same time), and a subsequent release of the trapped oxygen ions at a higher positive voltage. (vi) The oscillation of current with voltage continues, until a sudden current drop at ~ 10 V (Fig 3.13(f)). Oxidation reactions at the bulk oxide result in a high insulating state (different with the original state).

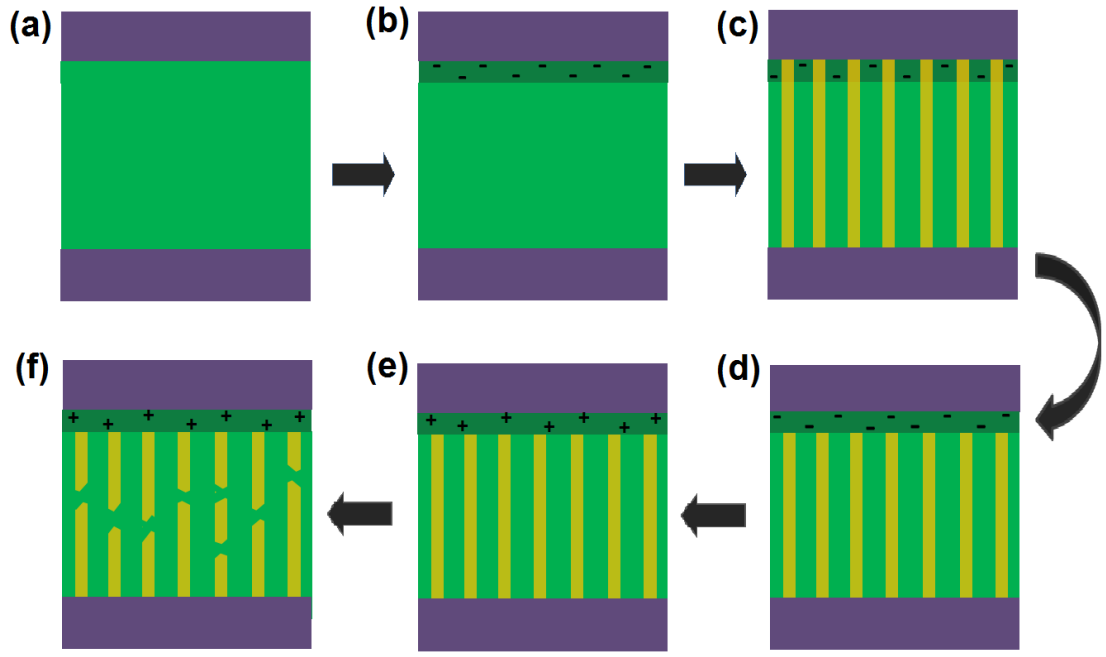

Figure 3.13: Schematic of the conversion between different resistance states. (a) - (f) the sweeping of voltage at different stages (the six circled numbers in Fig 3.12).

"Clockwise" polarity switching is defined as a positive voltage converting the device from a low resistance state (LRS) to a high resistance state (HRS), and a negative voltage converting the device from a HRS state to a LRS state. Fig 3.12 shows an overall "clockwise" resistive switching behavior, while a "counter clockwise" switching behavior is observed in Figs 3.3-3.5. Such "contradiction" is

frequently reported, even in the same material system [6, 32]. This can be explained by the electro-migration of oxygen ions under different voltages. Fig 3.4 shows that an intermediate voltage +/- 5 V is sufficient in a resistive switching. A negative voltage leads to a more insulating state, while too high a negative voltage (~ -10 V) will lead to an electrical breakdown, upon which the system is changed to a highly conducting state. Under a breakdown process, a significant reduction process occurs in the bulk oxide. The NDR behavior shown in Fig 3.12 is a typical example of resistance change under an electrical field. Control of the voltage (magnitude and polarity) results into different resistance states, as well as different resistive switching behaviors.

3.6 Chapter summary

In this chapter, the resistive switching characteristics of TiO_2 thin films were investigated using conductive atomic force microscopy (CAFM) and Kelvin probe force microscopy (KPFM). TiO_2 thin films with enhanced conductivity have been deposited. The as-prepared TiO_2 thin films were modulated into higher and lower resistance states by applying a local electric field. The resistive switching mechanism is shown to be related to charge injection and release assisted by electro-migration of oxygen ions under an electrical field. Although there are still many challenges in the fabrication of a switching device composing of a single filament, the observed high density nano-filaments show a good potential for high density RRAM applications. An integrated model combining both filamentary and interfacial effects is introduced to elucidate the observed phenomenon. This work sheds light on the understanding of the resistive switching mechanisms in oxide based switching devices.

References

[1] J. Y. Son and Y.-H. Shin, "Direct observation of conducting filaments on resistive switching of NiO thin films," *Appl. Phys. Lett*. **92**, 222106 (2008).

[2] K. Szot, R. Dittmann, W. Speier and R. Waser, "Nanoscale resistive switching in $SrTiO_3$ thin films," *Phys. Status Solidi RRL* **1**, R86-R88 (2007).

[3] J. J. Yang, F. Miao, M. D. Pickett, D. A. Ohlberg, D. R. Stewart, C. N. Lau and R. S. Williams, "The mechanism of electroforming of metal oxide memristive switches," *Nanotechnology* **20**, 215201 (2009).

[4] R. Müenstermann, J. J. Yang, J. P. Strachan, G. Medeiros-Ribeiro, R. Dittmann and R. Waser, "Morphological and electrical changes in TiO_2 memristive devices induced by electroforming and switching," *Phys. Status Solidi RRL* **4**, 16-18 (2010).

[5] C. Yoshida, K. Kinoshita, T. Yamasaki and Y. Sugiyama, "Direct observation of oxygen movement during resistance switching in NiO/Pt film," *Appl. Phys. Lett*. **93**, 042106 (2008).

[6] R. Müenstermann, T. Menke, R. Dittmann and R. Waser, "Coexistence of filamentary and homogeneous resistive switching in Fe-doped $SrTiO_3$ thin-film memristive devices*," Adv. Mater*. **22**, 4819-4822 (2010).

[7] B. J. Choi, D. S. Jeong, S. K. Kim, C. Rohde, S. Choi, J. H. Oh, H. J. Kim, C. S. Hwang, K. Szot, R. Waser, B. Reichenberg and S. Tiedke, "Resistive switching mechanism of TiO_2 thin films grown by atomic-layer deposition," *J. Appl. Phys*. **98**, 033715 (2005).

[8] X. Chen, N. J. Wu, J. Strozier and A. Ignatiev, "Direct resistance profile for an electrical pulse induced resistance change device," *Appl. Phys. Lett*. **87**, 233506 (2005).

[9] M. H. Lee, S. J. Song, K. M. Kim, G. H. Kim, J. Y. Seok, J. H. Yoon and C. S. Hwang, "Scanning probe based observation of bipolar resistive switching NiO films," *Appl. Phys. Lett*. **97**, 062909 (2010).

[10] M. Nonnemmacher, M. P. O'Boyle, and H. K. Wickramasinghe, "Kelvin probe force microscopy ," *Appl. Phys. Lett*. **58**, 2921-2923 (1991).

[11] W. Melitz, J. Shen, A. C. Kummel and S. Lee, "Kelvin probe force microscopy and its application," *Surf. Sci. Rep*. **66**, 1-27 (2011).

[12] Y. B. Nian, J. Strozier, N. J. Wu, X. Chen, and A. Ignatiev, "Evidence for an oxygen diffusion model for the electric pulse induced resistance change effect in transition-metal oxides," *Phys. Rev. Lett*. **98**, 146403 (2007).

[13] K. Szot, W. Speier, G. Bihlmayer, and R. Waser, "Switching the electrical resistance of individual dislocations in single-crystalline $SrTiO_3$," *Nat. Mater*. **5**, 312-320 (2006).

[14] M. J. Rozenberg, M. J. Sánchez, R. Weht, C. Acha, F. Gomez-Marlasca and P. Levy, "Mechanism for bipolar resistive switching in transition-metal oxides," *Phys. Rev. B* **81**, 115101 (2010).

[15] D. S. Jeong, R. Thomas, R. S. Katiyar, J. F. Scott, H. Kohlstedt, A. Petraru and C. S. Hwang, "Emerging memories: resistive switching mechanisms and current status," *Rep. Prog. Phys.* **75** 076502 (2012).

[16] R. Waser and M. Aono, "Nanoionics-based resistive switching memories," *Nat. Mater*. **6**, 833-840 (2007).

[17] R. Waser, R. Dittmann, G. Staikov and K. Szot, "Redox-based resistive switching memories – nanoionic mechanisms, prospects, and challenges," *Adv. Mater*. **21**, 2632-2663 (2009).

[18] A. Sawa, "Resistive switching in transition metal oxides," *Mater. Today* **11**, 28-36 (2008).

[19] A. Baikalov, Y. Q. Wang, B. Shen, B. Lorenz, S. Tsui, Y. Y. Sun, Y. Y. Xue and C. W. Chu, "Field-driven hysteretic and reversible resistive switch at the Ag–$Pr_{0.7}Ca_{0.3}MnO_3$ interface," *Appl. Phys. Lett*. **83**, 957-959 (2003).

[20] S. Tsui, A. Baikalov, J. Cmaidalka, Y. Y. Sun, Y. Q. Wang, Y. Y. Xue, C. W. Chu, L. Chen and A. J. Jacobson, "Field-induced resistive switching in metal-oxide interfaces," *Appl. Phys. Lett.* **85**, 317-319 (2004).

[21] K. M. Kim, B. J. Choi, Y. C. Shin, S. Choi and C. S. Hwang, "Anode-interface localized filamentary mechanism in resistive switching of TiO_2 thin films," *Appl. Phys. Lett*. **91**, 012907 (2007).

[22] D. H. Kwon, K. M. Kim, J. H. Jang, J. M. Jeon, M. H. Lee, G. H. Kim, X. S. Li, G. S. Park, B. Lee, S. Han, M. Kim and C. S. Hwang, "Atomic structure of conducting nanofilaments in TiO_2 resistive switching memory," *Nat. Nanotechnol.* **5**, 148-153 (2010).

[23] J. P. Strachan, M. D. Pickett, J. J. Yang, S. Aloni, A. L. D. Kilcoyne, G. Medeiros-Ribeiro and R. S. Williams, "Direct identification of the conducting

channels in a functioning memristive device," *Adv. Mater*. **22**, 3573-3577 (2010).

[24] H. D. Lee, B. Magyari-Köpe and Y. Nishi, "Model of metallic filament formation and rupture in NiO for unipolar switching," *Phys. Rev. B* **81**, 193202 (2010).

[25] G. –S. Park, X. –S. Li, D. –C. Kim, R. –J. Jung, M. -J. Lee and S. Seo, "Observation of electric-field induced Ni filament channels in polycrystalline NiO_x film," *Appl. Phys. Lett*. **91**, 222103 (2007).

[26] Using a much smaller size probe tip in a vacuum CAFM, filaments size in 2-4 nm diameter has also been reported [13], which means that each conducting spot could even be further composed of multiple conducting filaments in smaller sizes.

[27] Y. M. Du, H. Pan, S. J. Wang, T. Wu, Y. P. Feng, J. S. Pan and A. T. S. Wee, "Symmetrical negative differential resistance behavior of a resistive switching device," *ACS Nano* **6**, 2517-2523 (2012).

[28] A. Fujishima, X. Zhang and D. A. Tryk, "TiO_2 photocatalysis and related surface phenomena," *Surf. Sci. Rep*. **63**, 515-582 (2008).

[29] Y. Matsui, M. Suga, M. Hiratani, H. Miki and Y. Fujisaki, "Oxygen diffusion in Pt bottom electrodes of ferroelectric capacitors," *Jpn. J. Appl. Phys* **36**, L1239-L1241 (1997).

[30] K. Szot, W. Speier, R. Carius, U. Zastrow and W. Beyer, "Localized metallic conductivity and self-healing during thermal reduction of $SrTiO_3$," *Phys. Rev. Lett*. **88**, 075508 (2002).

[31] J. Philibert, *Atom Movements — Diffusion and Mass Transport in Solids*, Editions de Physique (1991).

[32] D. S. Jeong, H. Schroeder, U. Breuer, and R. Waser, "Characteristic electroforming behavior in Pt/TiO_2/Pt resistive switching cells depending on atmosphere," *J. Appl. Phys.* **104**, 123716 (2008).

Chapter 4

Symmetrical Negative Differential Resistance Behavior of a Resistive Switching Device

4.1 Introduction

Known as a switching effect, the negative differential resistance (NDR) behavior has been frequently reported for its potential device applications. The NDR

characteristic has been found in many physical systems such as double quantum wells [1], super lattices [2] and one dimensional systems [3-9].

More than 40 years ago, Simmons and Verderber (SV) fabricated an Au/SiO/Al sandwiched structure on a glass substrate [10]. After an electroforming process, they observed the I-V characteristics, as shown in Fig 4.1. SV described that if a voltage corresponding to the lowest point of the NDR region is applied and then reduced to zero, the I-V characteristic of a continuous sweep with the maximum of the voltage smaller than the V_T (threshold voltage) follows OE' (OB', OA') route, rather than OA route. These memory states can be stored without the application of electric power for a long time, that is, non-volatile memory states are formed.

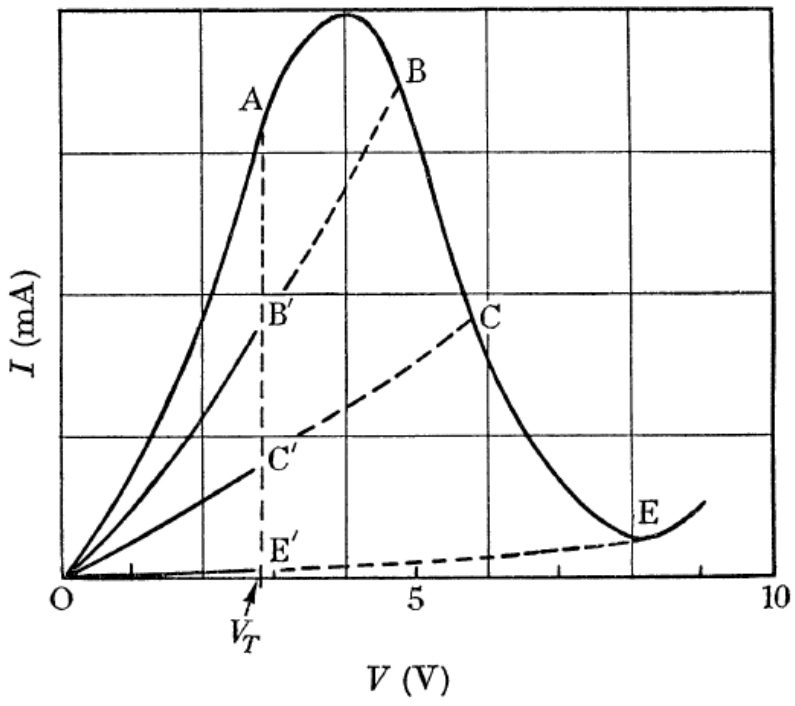

Figure 4.1: I-V characteristics observed in an Au/SiO/Al device. V_T – threshold voltage [10].

Since its discovery, the SV memory effect has attracted great interest in both fundamental studies and device applications. For a long time, this effect is mainly

discussed in thin film stacked structures. In recent years, the SV memory effect also found its application in organic materials based device structures. In 2004, Bozano *et al*. observed an NDR phenomenon in the devices of an Al (50 nm)/Alq_3 (50 nm)/Al (5nm)/Alq_3 (50nm)/Al (5nm) structure [4]. They demonstrated that the resistive switching phenomenon observed containing granular metal particles is consistent with the mechanism described by SV.

Based on the experimental observations, Bozano *et al*. concluded that the mechanism responsible for the NDR resistance switching behavior is a charge trapping effect involved with the space-charge field inhibition of electron injection [5]. They attributed the trapping sites to aluminum nanoparticles (NPs) from the electrode. The generality of the charge-storage mechanism in a wide variety of materials can be described as in Fig 4.2.

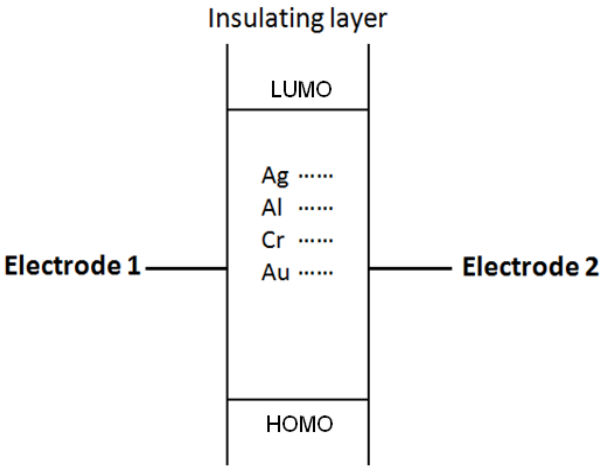

Figure 4.2: Energy-level representation for different metal nanoparticles (NPs), for a MIM structure composing of an organic insulating layer. LUMO – lowest unoccupied molecular orbital, HOMO – highest occupied molecular orbital.

There has been considerable discussion in the literature on the SV NDR effect [4, 5, 9, 11-14]. The lack of strong temperature dependence suggests that the current transport is based on tunneling. However, the mechanism they proposed is still

lacking of direct experimental evidences, especially for the band gap state they described. Great difficulties come from the *in-situ* characterization of the active regions for charge storage. Recent works on resistive switching show the formation of conductive filaments in bulk oxide through a reduction process [15-19]. It is possible for the formation of conductive filaments to provide low-resistance pathways between electrodes. In chapter 3, we investigated the resistive switching in the as-deposited TiO_2 thin films [20]. Multiple conductive filaments were observed through CAFM measurements. Furthermore, oxygen ions could play a key role in a charge storage process. Electro-migration of oxygen ions is also widely reported in a switching process [21-23].

Using passive circuit elements such as resistors, capacitors and inductors, a memristor model has been proposed in 1970s, to explain the resistive switching effect [24-26]. One of its typical characteristics is the symmetrical I-V behavior. Using the memristor model, Yang *et al*. recently explained this behavior by a circuit with two diodes back-to-back [27]. Alternatively, electron tunneling through a thin barrier can also describe such an I-V characteristic.

In this chapter, a resistive switching device with highly reproducible symmetrical NDR characteristic was investigated. The band gap state was determined by photoelectron spectroscopy measurements. To reveal the mechanism involved, first-principles calculations based on density functional theory (DFT) were also performed. The SV model was further discussed based on the experimental results. Instead of using a two-diode structure, we analyzed the observed electrical characteristics in the regime of tunneling, and proposed a new charge storage model combing both filamentary and interfacial effects, by introducing oxygen molecular ions as the active source.

4.2 Experimental observation of the symmetrical NDR phenomenon

A 20 nm thick amorphous TiO_2 thin film was deposited on a Pt/Ti/SiO_2/Si substrate by RF magnetron sputtering from a TiO_2 target at room temperature. Circular TiN top electrodes 100 μm in diameter were fabricated by sputtering using a metal shadow mask. The current-voltage measurements of the thin films were carried out at room temperature using an Agilent 4155C semiconductor analyzer. The sample was electroformed by performing I-V sweeps until stable resistive switching behavior was observed. Fig 4.3 shows the schematic structure of the device and the I-V set-up.

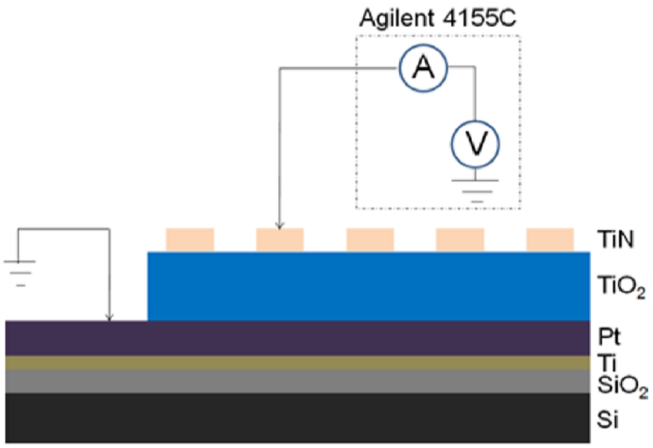

Figure 4.3: Schematic diagram of the device structure and the I-V measurement system.

The resistive switching behavior was measured by applying a bias voltage on the TE and with the bottom electrode (BE) grounded. After the electroforming process, a three-phase switching behavior with high repeatability is observed through a voltage sweep between -1.0 V and 1.0 V, as shown in Fig 4.4. The voltage sweep is at 50mV/step. As the applied voltage increases, the I-V trace of the device follows an exponential control function. When the voltage reaches a certain value (~ 0.65 V), the current begins to drop, showing a NDR characteristic. The resistance state is translated from a low resistance state to a high resistance state. Then with the decrease

of voltage, the I-V trace follows another exponential control function. As the voltage increases again under a negative voltage polarity, a sudden current jump (occurring randomly between -0.30 V to -0.55 V, centered at around 0.40 V) takes place before another NDR process (~ -0.65 V).

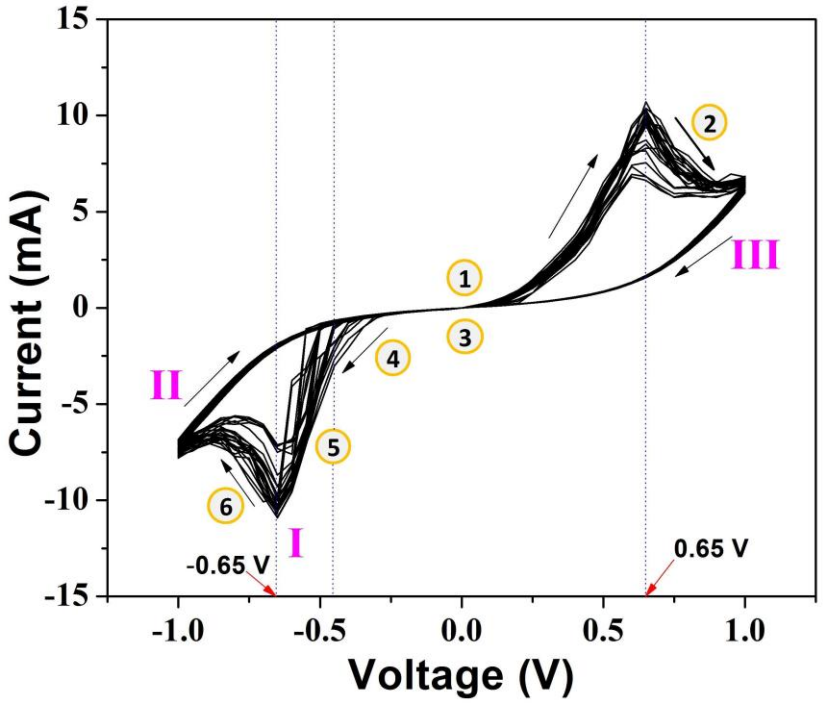

Figure 4.4: Experimental switching I-V curves. The curves represent 50 experimental switching loops, which show a high degree of repeatability. Phase I, II, III are defined as the resistance states from the lowest to the highest respectively. The six circled numbers refer to the sweep stage at different voltages.

The exponential I-V characteristic indicates electron tunneling and the NDR characteristic on the positive side can be explained by the charge storage mechanism, where the charge trapping at a specific band gap state is attributed to the NDR behavior in a resistive switching device.

4.3 The band gap state

It is known that a reduction process for single crystal TiO_2 creates the Ti3*d* state in the band gap [28-30]. Understanding the origin of the band gap state is important for improving or expanding the TiO_2-based systems for specific applications [28], for example, photocatalysis, photochemical water splitting, dye-sensitized solar cell, as well as memory devices. Despite the importance of the band state, the understanding of its structural characteristics is still incomplete.

4.3.1 Origin of the Ti3*d* state

The two common defects in TiO_2, oxygen vacancy [29] and Ti interstitial [30] are the two possible origins of the Ti3*d* state, which has been discussed extensively in recent years. TiO_2 can be made semiconducting upon reduction by ion sputtering or high temperature annealing. This sample preparation leads to the creation of oxygen vacancies, as well as Ti interstitials at the same time. Exposing the surface to O_2 could eliminate the band-gap state.

While the O-vacancy model has been widely accepted, Wendt *et al*. provide a different model in 2008 [30]. They reported that oxygen vacancies may not be the main origin of the band-gap state. Instead, they concluded that Ti interstitial atoms make the dominant contribution to the band-gap state. Since the publication of this work, an intense debate has been invoked. A representative work is from Yim *et al*. in 2010 [29]. They carried out a combined study using STM and photoemission spectroscopy to show that oxygen vacancy is still the origin of the Ti3*d* state. They used electron bombardment to vary oxygen vacancy densities, and directly showed that the peak area is in direct proportion to the oxygen vacancy density. They

concluded that the population of the band-gap state depends directly on the concentration of the oxygen vacancy.

4.3.2 PES measurements

To identify the band gap state, ultraviolet photoemission spectroscopy (UPS) experiments were carried out on the amorphous TiO_2 thin film. The UPS experiments were performed at room temperature, in an UHV end-station (base pressure 1×10^{-10} torr), at the SINS beamline at the synchrotron-radiation facility in SSLS (Singapore Synchrotron Light Source) [31]. Valence spectra were acquired with photon energy of 60 eV. E_F was determined by a Fermi edge cut-off from a multilayer Au film. The O_2 exposure was performed at room temperature.

In the stoichiometric form, TiO_2 is a wide band gap insulator. For a single crystal sample, the sample preparation procedure comprises of Ar^+ ion sputtering and high temperature annealing prior to UPS measurement [29, 30]. The sample structure TiO_2/Pt/Ti/SiO_2/Si in this experiment was prepared through an identical process prior to the deposition of the TiN top electrodes, with the 20 nm TiO_2 top layer deposited under the same conditions as the MIM device structures. Instead of an insulating behavior, the top thin film shows good conductivity, and can be used for UPS measurements directly. Fig 4.5 shows spectra corresponding to the sample without any treatment, after Ar^+ ion sputtering, and after an O_2 exposure of 1000 Langmuirs (L 1L=1×10^{-6} torr·sec) respectively. All the experiments are performed at room temperature.

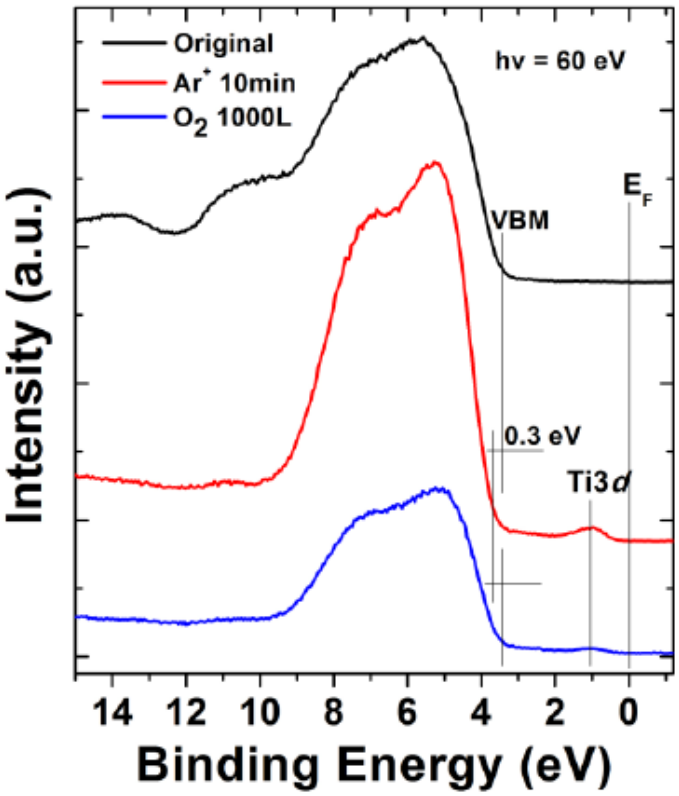

Figure 4.5: Photoelectron spectroscopy valence-band spectra. The as-deposited TiO_2 sample (black) was followed by 10 minutes' Ar^+ ion sputtering (red), and 1000 L oxygen exposure (blue) subsequently.

For the original sample, no band gap state was detected. A ~3.4 eV-wide band gap is determined from the measurement. After the sample was sputtered with 500 eV Ar^+ ion for ten minutes, a band gap state at ~1.02 eV below the Fermi-level is detected. This is consistent with the studies for single crystal samples based on electron energy loss spectroscopy (EELS) [32] and UPS [29, 30] measurements, with the gap feature observed at ~0.85 eV below the conduction band (CB), which is known as the Ti3*d* state. The Fermi-level position is close to the CB. The valence-band maximum (VBM) is shifted by ~0.3 eV away from the Fermi-level, with respect to the original sample. After an O_2 exposure of 1000 L, the intensity of the Ti3*d* state decreases dramatically, leaving a residual intensity. There is little change of Ti3*d* position between the sample after sputtering and after O_2 exposure. At the same time,

the VBM position shifts back to that of the original sample after oxygen exposure (Fig 4.8). For the original sample, the failure to detect the Ti3*d* state might be due to the low defect concentration, below the detection limit of UPS.

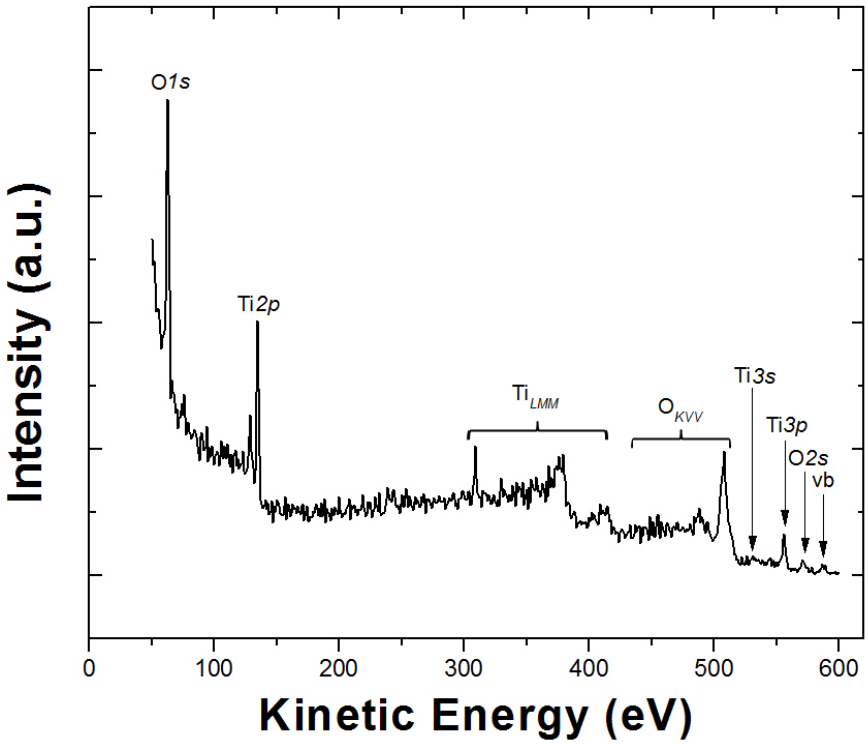

Figure 4.6: The overall XPS kinetic energy spectra.

The XPS survey spectra in Fig 4.6 gives evidence on the atomic species within the close surface ($hv = 600\ eV$). The photoelectrons and Auger peaks reveal the presence of titanium and oxygen.

The major peaks of deep binding energies in the XPS spectra are Ti*2p* and O*1s*. Fig 4.7 shows the XPS spectra of Ti*2p* and O*1s* of the same film respectively. The Ti*2p*3/2 peak position is at 458.6 eV and the O*1s* peak is at 530.7 eV.

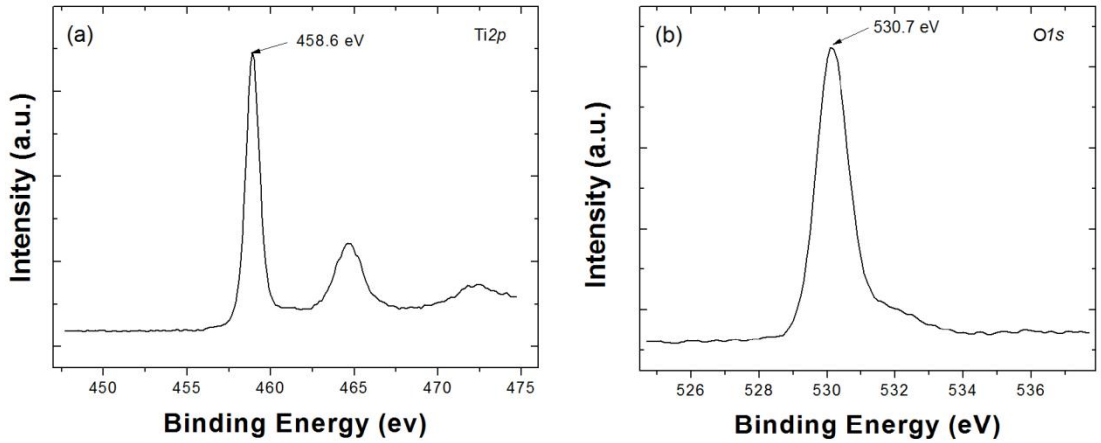

Figure 4.7: XPS binding energy spectra. (a) Ti*2p* and (b) O*1s*.

4.4 First-principles calculations

To understand the measured band gap state and provide further insight into the TiO_2-based NDR characteristics, we carried out first-principles calculations to investigate the electronic properties of TiO_2 with oxygen vacancy defects and interstitial negative charged oxygen atoms. Besides charge trapping, a charge detrapping process is necessary for a reversible switching. A sudden current jump at a negative bias around -0.40 V, could be attributed to such a process. With charge continuously trapping and detrapping under the electrical field, the two-sided NDR with symmetric characteristic forms. Oxidation and redox reactions at defect sites like oxygen vacancies may take place, due to the electro-migrated oxygen molecular ions at the interface. As a result, a structure with charged oxygen interstitials is proposed.

The first-principles calculation based on the density functional theory (DFT) [33] and the Perdew-Burke-Eznerhof generalized gradient approximation (PBE-GGA) [34] was carried out to find the mechanism. The projector augmented wave (PAW) scheme [35, 36] as incorporated in the Vienna *ab initio* simulation package (VASP) was used

in the study. The Monkhorst and Pack scheme of k point sampling was used for integration over the first Brillouin zone [37]. A 3×3×3 grid for k-point sampling for geometry optimization and an energy cut-off of 380 eV were consistently used in our calculations. The density of states (DOS) have been obtained with a 7×7×7 mesh. Good convergence was obtained with these parameters and the total energy was converged to 2.0×10^{-5} eV/atom. The bulk anatase TiO_2 structure (a-TiO_2) is modeled with a 3×3×1 supercell containing 36 Ti atoms and 72 O atoms. The GGA+*U* method was used to treat 3d electrons of Ti with the Hubbard on-site Coulomb interaction parameter U_{eff} (*U*-*J*) [38] to calculate the electronic structures of TiO_2 with and without doping. A value of 5 eV for the U_{eff} (*U*-*J*) is consistently used in our calculations to find the defect level in the band gap comparable with the experimental value.

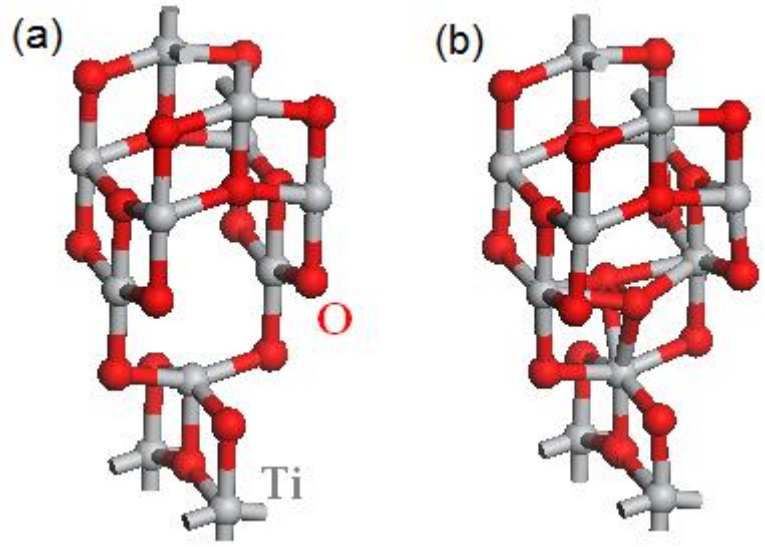

Figure 4.8: First-principles calculations of TiO_2 with oxygen vacancy and charged oxygen interstitial defects. (a) The local structure of TiO_2 with oxygen vacancy. (b) The local structures of TiO_2 with oxygen vacancy occupied by O_2^{2-}.

The oxygen vacancy (V_O) is created by removing one oxygen atom from the supercell (Fig 4.8(a)). The charged oxygen interstitial is realized by putting an O_2^{2-}

into the vacancy site (Fig 4.8(b)). The optimized structure (Fig 4.8(a)) shows that V_O has little effect on the local structure, indicating that V_O is the dominant defect in TiO_2. By inserting O_2^{2-} into the vacancy site, the local structure is slightly distorted (Fig 4.8(b)). The Ti-O bond near the defect is extended by 1%. The distance between Ti and interstitial O is about 2.14 Å and about 4 % larger than the Ti-O bond. The O-O bond is 1.49 Å, larger than that in an isolated molecule (1.24 Å). The calculated band gap of the pristine TiO_2 is about 2.7 eV [39-40] (Fig 4.9(a)). Defect states are formed within the band gap (0.67 eV above the middle of the band gap) by introducing V_O into TiO_2 (Fig 4.9(b)). The position of the defect band within the band gap is close to 0.65 eV value obtained from the I-V curves. With the vacancy site occupied by mobile charged O_2^{2-}, the V_O states disappear and the E_f shifts to CB (Fig 4.9(c)). Charge storage is realized by negative charges fixed at the trapped oxygen atoms, and the device resistance state transfers to another level, leading to the NDR effect.

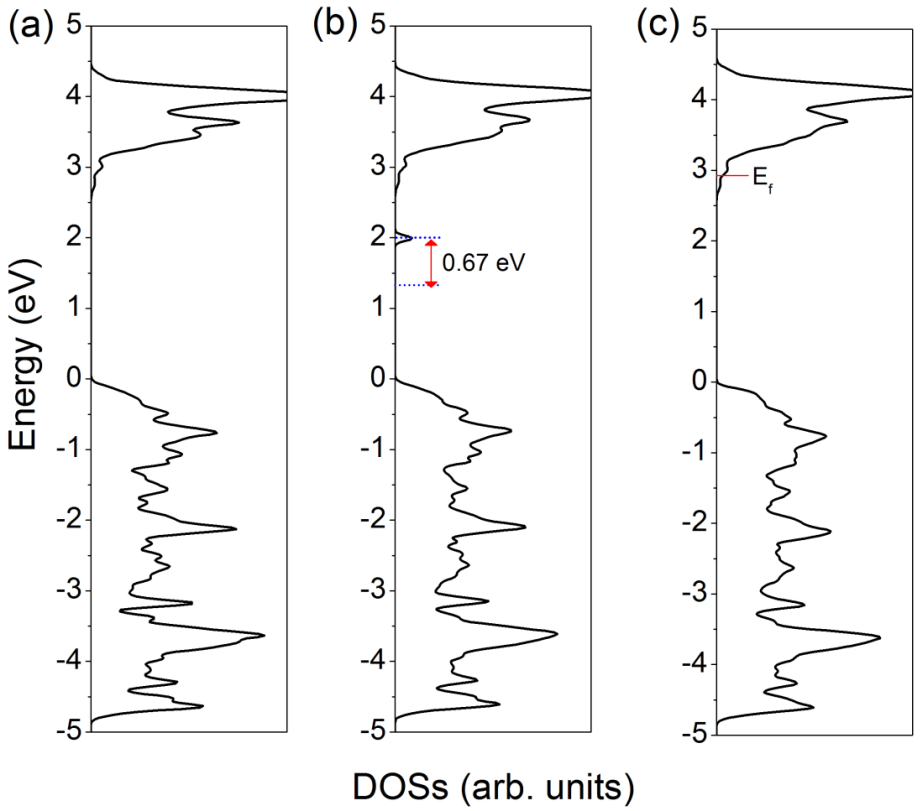

Figure 4.9: Total density of states of**:** (a) TiO_2, (b) TiO_2 with V_O, and (c) TiO_2 with V_O occupied with O_2^{2-}.

The sudden current jump observed at a negative voltage (Fig 4.4) is proposed to be the release of O_2^{2-} from vacancy sites. The energy barrier for the process is calculated from:

$$E_b(O_2^{2-}) = E_{tot}(TiO_2 + V_O + O_2^{2-}) - E_{tot}(TiO_2 + V_O) + E(O_2) - 2E_f \quad (2)$$

where $E_{tot}(TiO_2 + V_O)$ is the total energy of the cell containing a vacancy. $E_{tot}(TiO_2 + V_O + O_2^{2-})$ is the total energy of the cell with the vacancy occupied by O_2^{2-}, and $E(O_2)$ is the energy of oxygen molecule and E_f is the Fermi energy. The calculated energy barrier (E_b) is a function of E_f. For the charged system, the Fermi level shifts into the CB by electron doping after the oxygen molecular ion was

introduced into the neutral cell (Fig 4.9(c)). Therefore, E_b is about 0.36 eV, consistent with the threshold values (~ -0.40 eV) from the I-V curves (Fig 4.10).The random characteristic of the threshold voltage values may be due to the different oxygen environments at the interface, during each electrical sweep. On the other hand, the modeling is based on a crystalline interface which represents an ideal situation in contrast to the much more complex situation at the metal/oxide device heterostructures.

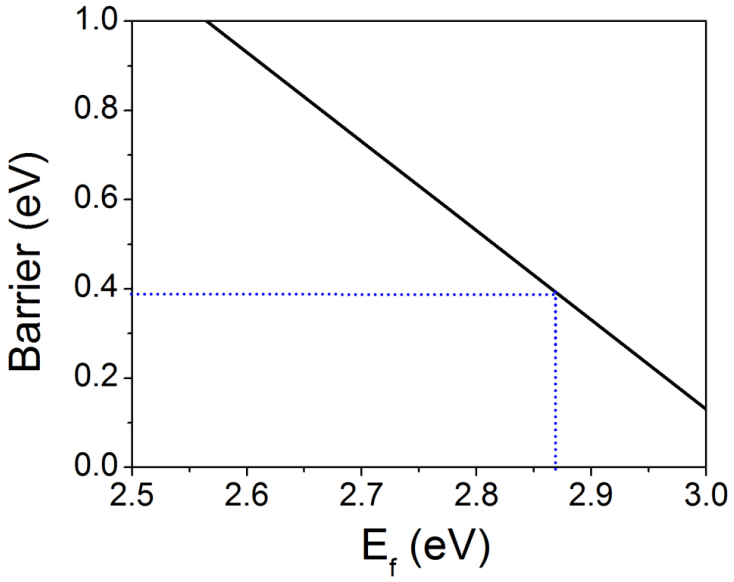

Figure 4.10: Formation energy of oxygen vacancy from the charged oxygen interstitial structure, as a function of the Fermi level (E_f). E_f is measured from the VBM.

The first-principles calculations show that oxygen vacancy is a deep band gap state in the band gap. This is consistent with the work [41] by Di Valentin *et al*. The strong electron localization of an isolated single oxygen vacancy indicates that the effect of vacancy on the conductivity is negligible. With oxygen ions trapping and detrapping at oxygen vacancies, the device is switched between different resistance states. Charge storage and release is realized through oxidation and redox reactions, as

shown in Fig 4.11. Fig 4.11(a) shows the state with an oxygen vacancy, and Fig 4.11(b) shows the injection of oxygen molecule ions leads to a structure that includes oxygen interstitials.

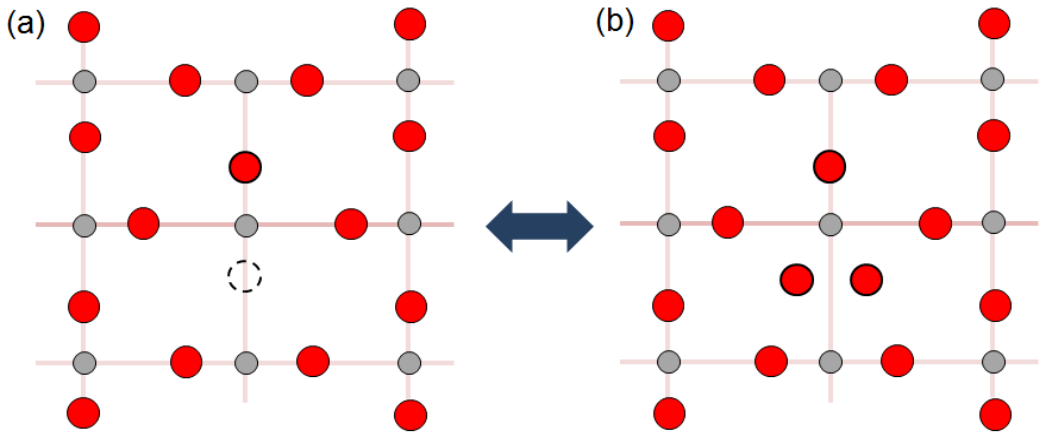

Figure 4.11: Charge storage and release through oxygen molecule ions. (a) Formation of an oxygen vacancy. (b) Formation of oxygen interstitial after an oxygen molecule ion trapping process. Red – O atom, grey – Ti atom.

4.5 Charge storage memory effect

The charge storage in thin-film dielectrics is known for its application in memory devices. The trapping sites could be defects, or metal nano-particles/nano-clusters introduced in the thin film. Charges are injected at high electric fields and become subsequently trapped within the insulator. Modification of the electrostatic barrier characteristic leads to a resistance state change. In chapter 3, we discussed that the injection and release of oxygen ions results in different resistance states. At the metal/oxide interface, the stored charges change the electrical barrier, and further chemical reactions lead to microstructural changes. For charge storage induced resistive switching, one well-known model is the SV charge storage mechanism

proposed in 1960s [10], and the other is the thee-domain model proposed by Rozenberg *et al*. in 2004 [42].

4.5.1 The SV mechanism

The mechanism described by SV is presented in Fig 4.12. Based on a Au/SiO/Al structure [10], SV proposed the mechanism as follows:

(i) The gold ions (from electrode) introduced into the SiO insulating film lead to the formation of a band gap state, that is, localized states within the forbidden band gap (Fig 4.12(a)).

(ii) For the case $qV < \phi_i$, the contribution to the total current is mainly due to electron tunnelling (Fig 4.12(b)). As the applied voltage V increases, the conduction current increases and reaches the peak value when $V = \phi_i/q$.

(iii) As the voltage increases to $qV > \phi_i$, the electrons from the electrode tunnel to the impurity sites (for example, point A) (Fig 4.12(c). These electrons do not contribute to the conduction current unless they receive sufficient thermal energy and jump to the conduction band. As a result, the current starts to drop after the threshold voltage point.

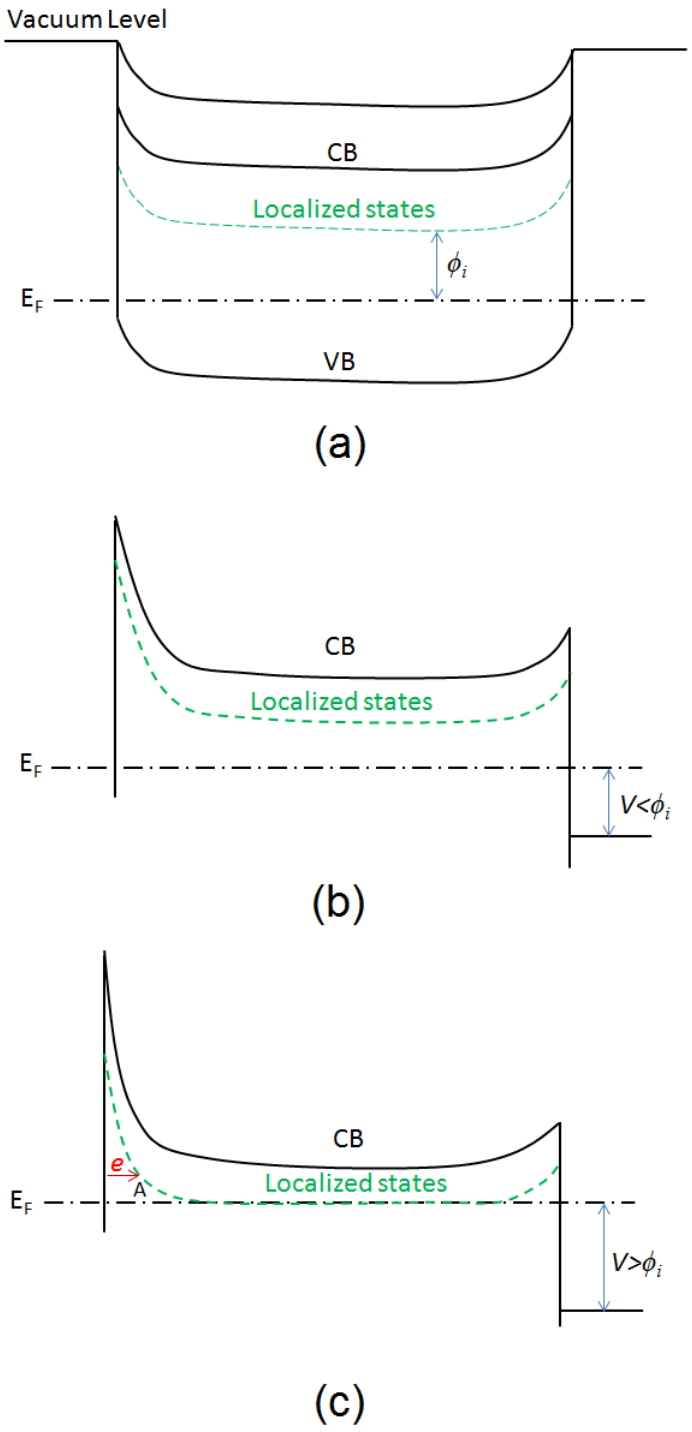

Figure 4.12: Energy band diagrams of a formed metal-insulator-metal system under different applied voltages: (a) $V = 0$; (b) $V < \phi_i$; (c) $V > \phi_i$.

Using this mechanism, SV explained the observed NDR phenomenon. They attributed the memory effect to trapped electrons at the impurity band within the

insulating thin film. SV further described the memory state after the electron trapping process, as shown in Fig 4.13.

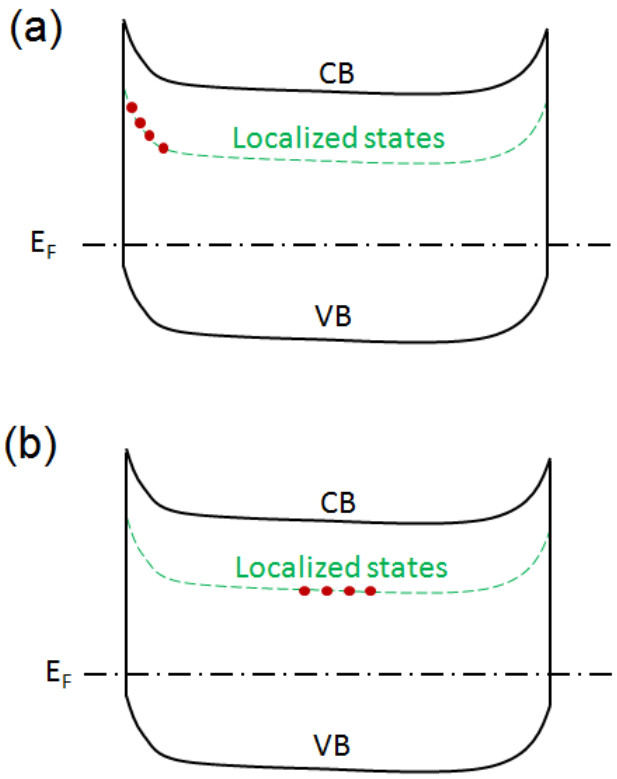

Figure 4.13: Energy band diagrams showing the position of the stored charges: (a) at a voltage bias of *V*; (b) after a time period $t > (\nu P)^{-1}$.

Fig 4.13(a) illustrates that electrons enter into the insulator after a bias voltage $V > \phi_i$ is applied. The electrons are stored at the localized impurity sites close to electrode. When the voltage is removed quickly, the stored electrons will remain undistributed in the sites they occupied, for a period of time equal to $(\nu P)^{-1}$, where ν is the attempt-to-escape frequency and P is the tunnelling probability. At a time $t > (\nu P)^{-1}$, the electrons begin to diffuse through the insulator by tunneling from one site to the other. SV described that the electrons will reach the vicinity of the centre of the insulator where they are permanently stored (Fig 4.13(b)).

4.5.2 The three-domain structure

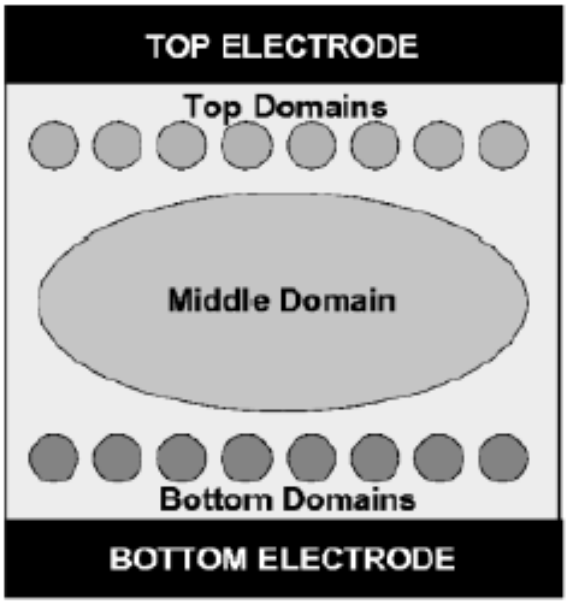

Figure 4.14: Schematic view of the model with top and bottom electrodes, insulating medium, smaller top and bottom domains, and large middle domains [42].

The rapid progress in the study of resistive switching has provided new understandings of the charge storage mechanism. In 2004, Rozenberg *et al*. [42] reported a three-domain model, as shown in Fig 4.14. They proposed a nonpercolating domain structure. The memory state is formed through charge storage in the domains. In their descriptions, three kinds of metal domains are in the film between the top and the bottom electrodes. The current is controlled by charge injection into the domains, and finally tunneling to another electrode. This model is very successful in explaining many kinds of phenomena in resistive switching. However, similar to the SV model, this model is like another hypothesis due to the lack of direct evidences from experimental measurements. The three-domain structure needs more detailed microstructure descriptions.

4.6 The switching mechanism

Understanding and controlling of the conductivity is important in resistive switching. As a comparison to the variable n-type sources under discussion, conducting nanofilaments inside amorphous TiO_2 films could also be the source of the good conductivity. The recent report by Kwon *et al.* shows direct evidence of conducting nanofilaments with oxygen-deficient Magnéli phases inside TiO_2 films for resistive switching [18]. Strachan *et al*. also reported that localized reductions lead to the formation of metallic conducting channels in TiO_2 [43]. Comparably, using density functional theory, a microscopic model for electrically active filaments composed of metallic nickel atoms chains was presented by Lee *et al*., based on oxygen-deficient NiO structures [44]. Studies on oxide coated cathode have been reported for a long time. From the literature review by Dearnaley [45], Mutter [46] studied emission and conductivity of such structure and revealed that the oxide conductivity is ohmic and independent of the current flow direction. The model [47] by Dearnaley *et al*. proposed that conducting filaments with molecular dimensions develop through the oxide coating. Extended into the oxide matrix, the filaments are directly responsible for the electrical conductivity and the high thermionic emission of the oxide. Based on filamentary theory and the model proposed in chapter 3, a model to explain the observed electrical phenomenon in Fig 4.4 is shown in Fig. 4.15(b). Distinct from the host matrix of the oxide, the filamentary conducting paths work as a bridge between the two electrodes. The insulating TiO_2 layer lies at the interface between TE and the bulk oxide layer. During electroforming process of the devices, a linear I-V characteristic attributed to filamentary conduction has been observed. TiN is widely used as a “diffusion barrier” in semiconductor manufacturing. Under an electro-migration process, oxygen ions tend to pile up at the TE/oxide interface and

migrate out through BE. At the top interface, oxidation of the filaments may take place. As a result, a thin interface insulating layer is formed. Electrons need to tunnel through the interfacial layer with filaments as the conducting bridges. An electrode-filament-IL-electrode junction is then formed. With a voltage applied, the current flow is determined by the interface layer thickness and barrier height. As a comparison to the top interface, the TiO_2/Pt(BE) interface is attributed as an ohmic contact [48-50].

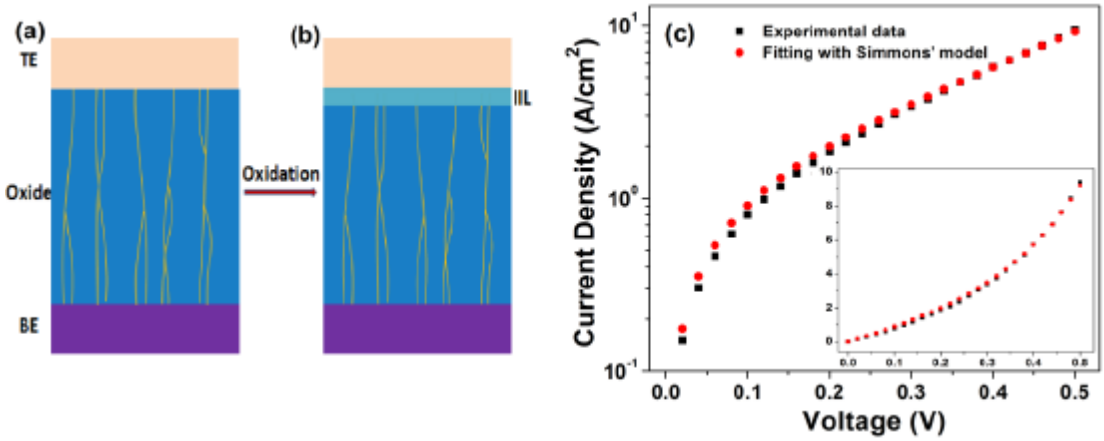

Figure 4.15: (a) and (b) Sketch of the model: the top interface is an interface insulating layer (IIL) formed after an oxidation process of the conducting filaments at the interface area; the bulk oxide consists a number of conducting filaments, as a comparison to the surrounding insulator matrix. (c) Plots of average current density *versus* voltage in a semi-log scale**:** Black dotted line shows the raw data sampled from the I-V curves, and the red dotted line shows the fitting results based on the current tunneling model by Simmons. The inset shows the same curves in a linear scale. The IIL thickness is fitted at ~1.84 nm.

Based on the Wentzel-Kramers-Brillouin (WKB) approximation, tunneling currents in the direct tunneling regime can be described by the Simmons model (1963) [51, 52].

$$J = \frac{e}{2\pi h d^2}\left\{\left(e\varphi_0 - \frac{eV}{2}\right)\times\exp\left[-\frac{4\pi d}{h}(2m)^{1/2}\alpha\left(e\varphi_0 - \frac{eV}{2}\right)^{1/2}\right]\right.$$
$$\left.-\left(e\varphi_0 + \frac{eV}{2}\right)\times\exp\left[-\frac{4\pi d}{h}(2m)^{1/2}\alpha\left(e\varphi_0 + \frac{eV}{2}\right)^{1/2}\right]\right\} \quad (1)$$

This equation expresses current density as a function of voltage V with barrier height φ_0 and insulator thickness d being the key parameters that affect the electron direct tunneling through a barrier; h is Planck's constant, α is a unitless parameter [52, 53] used for fitting, m is the rest mass of electron and e is the elementary charge. The fitting parameter α =1 refers to a rectangular barrier. For a non-rectangular barrier, the α value needs to be further adjusted.

Based on expression (1), a good fit between experiment data and Simmons' model has been obtained, as shown in Fig 4.15(c). Using this method, the interfacial layer thickness was estimated to be 1.84 nm, with the barrier height and the α parameter at 1.04 eV and 0.98 respectively. The data were sampled from the I-V curves of the device shown in Fig 4.4.

In the UPS measurements, the Fermi level was moved up to be close to the CB, in contrast to that of an insulator oxide. Based on the first-principles calculations, we attribute the 1.02 eV Ti3*d* state to oxygen vacancies, that is, a deep band gap state for the CB. There has been considerable discussion in the literature about the n-type dopant source for TiO_2. In particular, hydrogen (a ubiquitous impurity in many oxides) has [41, 54, 55] been reported to produce shallow donor electrons below the CB. Ti interstitial could be another n-type source for TiO_2. This is similar to the case of ZnO, another wide band gap oxide, for which hydrogen and Zn interstitial have become to be recognized as the n-type source in recent years (the discussion on oxygen vacancy is controversial and still a matter of debate) [56]. With TiO_2 as an insulator and the Fermi level in the middle of the band gap, the 0.65 eV (0.67 eV in calculation) state

coincides well with that of the 1.02 eV Ti3*d* state observed in the band gap. The sum of 1.67 eV is very close to the half band gap value 1.7 eV based on the UPS experiments.

The interface insulator layer comes from the oxidation of the filaments at the top interface and acts as the primary area for charge trapping. With electrons trapping at the band gap state introduced by native oxygen vacancies, the NDR characteristic on the positive side occurs.

With the above analysis, we summarize the resistive switching phenomenon shown in Fig 4.4, of which the simplified energy band diagrams corresponding to each step of the I-V traces are illustrated in Fig 4.16. The band bending effect at the interface between the insulating layer and the contact is not shown in the energy diagrams. The different resistance states are defined as Phase I, II, and III respectively. With electrons trapped to one side of the top insulating layer during earlier electroforming processes, the device memory state is at Phase II (Fig 4.16(a)). Then with the voltage increasing on the positive side, electrons start to be trapped into the defect sites on the other side, when *V* is above 0.65 V (Fig 4.16(b)). After this stage, the memory state is switched to Phase III (Fig 4.16(c)). Fig 4.16(d) shows the band state when voltage is under a negative polarity. With the voltage increased on the negative side, trapped charges are released from the defect sites at a voltage around -0.40 V, after which the memory state is switched back to phase I (Fig 4.16(e)). With further increase of voltage above -0.65 V, electrons start to be trapped again and the memory state is switched to Phase II (Fig 4.16(f)). With continuous voltage sweeps between -1.0 V and 1.0 V, this behavior shows high repeatability. Besides TiN as the TE material, we have also made structures with Pt and Ni as the TE. The symmetric NDR characteristic shown in Fig 1b was only observed for a TiN/TiO_2/Pt structure.

This may be due to the difference in oxygen diffusion ability. As a comparison to that of TiN, a good oxygen diffuse ability was reported for Pt and Ni [57, 58]. Oxygen ions pile up at the TE/oxide interface under a positive bias and migrate out of the structure through Pt under a negative bias. For this reason, the trapped charges are easier to be released under a negative bias, compared with a positive bias. Under a negative bias, the charged oxygen interstitials tend to be removed, and the temporarily trapped oxygen atoms might be dragged out at the same time, upon which oxygen vacancies are then formed.

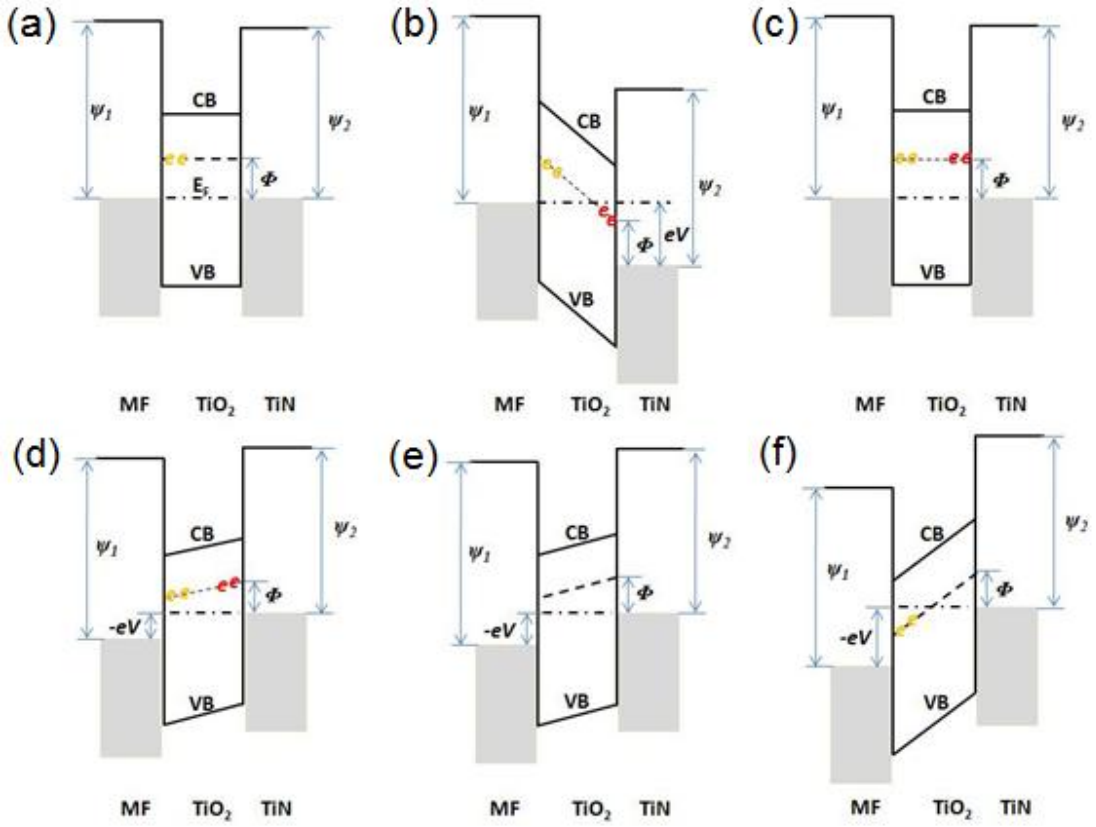

Figure 4.16: Energy band diagrams of the TiN/TiO_2/Pt resistive switching device for various voltages (a-f referring to the six circled numbers depicted in Fig 4.4). MF – the layer with metallic filaments. ψ_1, ψ_2 - work functions. Φ – oxygen vacancy energy level.

The interface energy barrier for electrons to tunnel through is changed, due to the piling up of negative charges at the interface. The low and high resistance states are

formed, depending on the charge trapping states at the interface insulator layer respectively. Charges tend to trap from the outer into the inner region of the insulator layer. With oxygen molecular ions trapping into the neutral regions, the Fermi-level will be shifted by electron doping, as compared to the other regions of the interface layer without trapped charges. The charge trapping at different regions of the interface insulator oxide is similar to the nonpercolating domain structure proposed by Rozenberg *et al*. [42] where charge injection and release take place at the specific domains. Moreover, since the negative charges are fixed at the trapped oxygen atoms, it is difficult for the charges to spread through the insulator layer after an electron "traveling" process, according to the theory described by SV [10].

SV attributed the observed non-volatile resistance states to electron trapping to the specific sites introduced by the diffusion of gold atoms into the oxide [10]. Instead of using electrons as the source in charge trapping, we interpreted the switching behavior in Fig 4.4 based on first-principles modeling, by introducing oxygen molecular ions into the TiO_2 cells. Upon microstructure changes, the trapped electrons are fixed at the specific sites. On the other hand, it could also be of a dual-process composed of electron trapping and a subsequent reaction between oxygen vacancies (with trapped electrons) and non-lattice oxygen molecules. Trapped electrons are fixed with the oxygen atoms at the defect sites of the insulator layer. This leads to using oxygen molecules for charge storage.

4.7 Chapter summary

We have demonstrated symmetrical NDR effects with high repeatability in a resistive switching device. A thin interfacial layer of a few monolayers is attributed as the origin of the observed electrical phenomenon. The oxygen vacancy is proposed as the band gap state and correlated to the Ti3*d* state. The defect state obtained from the

current-voltage curves complies well with that from the photoelectron spectroscopy measurements. The electronic phenomena observed are in agreement with theoretical calculations based on first-principles modeling. In the electron tunneling regime, with oxygen molecular ions as the active source, a new model based on charge trapping and detrapping is proposed for the observed resistive switching phenomenon. The results suggest that charge storage can be realized by introducing specific defects in a very thin insulating layer.

In comparison to the SV model, we proposed a new charge storage mechanism by introducing oxygen molecular ions. Through microstructure changes, charges are stored at the lattice. It is different with the electron trapping model by SV, in which they assumed the diffusion of gold atoms into the oxide layer to form localized states. In the direct tunneling regime, we attribute the high current to electron tunneling through a thin interface layer. Instead of a bulk-effect, the short-range oxidation and redox reactions at the interface region lead to the change of resistance states. By introducing conductive filaments in the bulk oxide, we proposed a new model with a thin interfacial layer as the active region for charge storage. We proposed that trapped carriers are stored and released in a domain-like structure at the interface region. The space charge field effect at a thin interface insulator layer modulates the current flow.

The results and mechanism demonstrated here in a thin layer could be extended to other systems approaching molecular dimensions for device applications. We expect the ability to pattern high repeatability reversible NDR characteristic to present a new direction for high density information storage and processing.

References

[1] L. L. Chang, L. Esaki and R. Tsu, "Resonant tunneling in semiconductor double barriers," *Appl. Phys. Lett.* **24**, 593-595 (1974).

[2] L. Esaki and L. L. Chang, "New transport phenomenon in a semiconductor 'superlattice'," *Phys. Rev. Lett.* **33**, 495-498 (1974).

[3] J. D. Le, Y. He, T. R. Hoye, C. C. Mead and R. A. Kiehl, "Negative differential resistance in a bilayer molecular junction," *Appl. Phys. Lett.* **83**, 5518-5520 (2003).

[4] L. D. Bozano, B. W. Kean, V. R. Deline, J. R. Salem and J. C. Scott, "Mechanism for bistability in organic memory elements," *Appl. Phys. Lett*. **84**, 607-609 (2004).

[5] L. D. Bozano, B. W. Kean, M. Beinhoff, K. R. Carter, P. M. Rice and J. C. Scott, "Organic materials and thin-film structures for cross-point memory cells based on trapping in metallic nanoparticles," *Adv. Funct. Mater*. **15**, 1933-1939 (2005).

[6] C. Zhou, J. Kong, E. Yenilmez and H. Dai, "Modulated chemical doping of individual carbon nanotubes," *Science* **290**, 1552-1555 (2000).

[7] T. Rakshit, G. –C. Liang, A. W. Ghosh and S. Datta, "Silicon-based molecular electronics," *Nano Lett*. **4**, 1803-1807 (2004).

[8] J. Chen, M. A. Reed, A. M. Rawlett and J. M. Tour, "Large on-off ratios and negative differential resistance in a molecular electronic device," *Science* **286**, 1550-1552 (1999).

[9] W. Tang, H. Shi, G. Xu, B. S. Ong, Z. D. Popovic, J. Deng, J. Zhao, G. Rao, "Memory effect and negative differential resistance by electrode-induced two dimensional single-electron tunneling in molecular and organic electronic devices," *Adv. Mater.* **17**, 2307-2311 (2005).

[10] J. G. Simmons and R. R. Verderber, "New conduction and reversible memory phenomena in thin insulating films," *Proc. R. Soc. London, Ser. A.* **301**, 77-102 (1967).

[11] Y. Yang, J. Ouyang, L. Ma, R. J. –H. Tseng and C. –W. Chu, "Electrical switching and bistability in organic/polymeric thin films and memory devices," *Adv. Funct. Mater.***16**, 1001-1014 (2006).

[12] J. C. Scott and L. D. Bozano, "Nonvolatile memory elements based on organic materials," *Adv. Mater.* **19**, 1452-1463 (2007).

[13] R. R. Sutherland, "A theory for negative resistance and memory effects in thin insulating films and its application to Au-ZnS-Au devices," *J. Phys. D: Appl. Phys.* **4**, 468-479 (1971).

[14] C. Rossel, G. I. Meijer, D. Brémaud and D. Widmer, "Electrical current distribution across a metal–insulator–metal structure during bistable switching," *J. Appl. Phys*. **90**, 2892-2898 (2001).

[15] R. Waser and M. Aono, "Nanoionics-based resistive switching memories," *Nat. Mater*. **6**, 833-840 (2007).

[16] R. Waser, R. Dittman, G. Staikov and L. Szot, "Redox-based resistive switching memories – nanoionic mechanisms, prospects, and challenges," *Adv. Mater*. **21**, 2632-2663 (2009).

[17] A. Sawa, "Resistive switching in transition metal oxides," *Mater. Today* **11**, 28-36 (2008).

[18] D. H. Kwon, K. M. Kim, J. H. Jang, J. M. Jeon, M. H. Lee, G. H. Kim, X. S. Li, G. S. Park, B. Lee, S. Han, M. Kim, and C. S. Hwang, "Atomic structure of conducting nanofilaments in TiO_2 resistive switching memory," *Nat. Nanotechnol.* **5**, 148-153 (2010).

[19] G. –S. Park, X. –S. Li, D. –C. Kim, R. –J. Jung, M. –J. Lee and S. Seo, "Observation of electric-field induced Ni filament channels in polycrystalline NiO_x film," *Appl. Phys. Lett.* **91**, 222103 (2007).

[20] Y. M. Du, A. Kumar, H. Pan, K. Y. Zeng, S. J. Wang, P. Yang and A. T. S. Wee, "The resistive switching in TiO_2 films studies by conductive atomic force microscopy and Kelvin probe force microscopy." (Submitted)

[21] C. Yoshida, K. Kinoshita, T. Yamasaki and Y. Sugiyama, "Direct observation of oxygen movement during resistance switching in NiO/Pt film," *Appl. Phys. Lett.* **93**, 042106 (2008).

[22] D. S. Jeong, H. Schroeder, U. Breuer, and R. Waser, "Characteristic electroforming behavior in Pt/TiO_2/Pt resistive switching cells depending on atmosphere," *J. Appl. Phys.* **104**, 123716 (2008).

[23] Y. B. Nian, J. Strozier, N. J. Wu, X. Chen and A. Ignatiev, "Evidence for an oxygen diffusion model for the electric pulse induced resistance change effect in transition-metal oxides," *Phys. Rev. Lett.* **98**, 146403 (2007).

[24] L. O. Chua, "Memristor – the missing circuit element," *IEEE Trans. Circuit Theory CT-18*, 507-519 (1971).

[25] D. B. Strukov, G. S. Snider, D. R. Stewart and R. S. Williams, "The missing memristor found," *Nature* **453**, 80-83 (2008).

[26] A. Adamatzky and L. Chua, "Memristive excitable cellular automata," *Int. J. Bifurcation Chaos* **21**, 3083-3102 (2011).

[27] J. J. Yang, M. D. Pickett, X. Li, D. A. A. Ohlberg, D. R. Stewart and R. S. Williams, "Memristive switching mechanism for metal/oxide/metal nanodevices," *Nat. Nanotechnol.* **3**, 429-433 (2008).

[28] A. Fujishima, X. Zhang and D. A. Tryk, "TiO_2 photocatalysis and related surface phenomena," *Surf. Sci. Rep*. **63**, 515-582 (2008).

[29] C. M. Yim, C. L. Pang and G. Thornton, "Oxygen vacancy origin of the surface band-gap state of TiO_2 (110)," *Phys. Rev. Lett.* **104**, 036806 (2010).

[30] S. Wendt, P. T. Sprunger, E. Lira, G. K. H. Madsen, Z. Li, J. O. Hansen, J. Matthiesen, A. Blekinge-Rasmussen, E. Laegsgaard, B. Hammer and F. Besenbacher, "The role of interstitial sites in the Ti3*d* defect state in the band gap of titania," *Science* **320**, 1755-1759 (2008).

[31] X. J. Yu, O. Wilheimi, H. O. Moser, S. V. Vidyarai, X. Y. Gao, A. T. S. Wee, T. Nyunt, H. Qian and H. Zheng, "New soft X-ray facility SINS for surface and

nanoscale science at SSLS," *J. Electron Spectrosc. Relat. Phenom*. **144–147**, 1031-1034 (2005).

[32] W. S. Epling, C. H. F. Peden, M. A. Henderson and U. Diebold, "Evidence for oxygen adatoms on TiO_2 (110) resulting from O_2 dissociation at vacancy sites," *Surf. Sci.* **412-413**, 333-343 (1998).

[33] P. Hohenberg and W. Kohn, "Inhomogeneous electron gas," *Phys. Rev.* **136**, B864-B871 (1964).

[34] J. P. Perdew, K. Burke and M. Ernzerhof, "Generalized gradient approximation made simple," *Phys. Rev. Lett.* **77**, 3865-3868 (1996).

[35] P. E. Blöchl, "Projector augmented-wave method," *Phys. Rev. B* **50**, 17953-17979 (1994).

[36] G. Kresse and D. Joubert, "From ultrasoft pseudopotentials to the projector augmented-wave method," *Phys. Rev. B* **59**, 1758-1775 (1999).

[37] H. J. Monkhorst and J. D. Pack, "Special points for Brillouin-zone integrations," *Phys. Rev. B* **13**, 5188-5192 (1976).

[38] S. L. Dudarev, G. A. Botton, S. Y. Savrasov, C. J. Humphreys and A. P. Sutton, "Electron-energy-loss spectra and the structural stability of nickel oxide: An LSDA+U study," *Phys. Rev. B* **57**, 1505-1509 (1998).

[39] GGA approach always underestimates the band gap of material. The calculated band gap is ~2.7 eV with the Coulomb interaction parameter U_{eff} (U-J) = 5 eV. We do not expect to be able to open up the band gap using any "reasonable" U value [40], nor is this our goal here.

[40] Z. Hu and H. Metiu, "Choice of *U* for DFT+*U* calculations for titanium oxides," *J. Phys. Chem. C* **115**, 5841 – 5845 (2011).

[41] C. Di Valentin, G. Pacchioni and A. Selloni, "Reduced and n-type doped TiO_2: nature of Ti^{3+} species," *J. Phys. Chem. C* **113**, 20543-20552 (2009).

[42] M. J. Rozenberg, I. H. Inoue and M. J. Sànchez, "Nonvolatile memory with multilevel switching: a basic model," *Phys. Rev. Lett*. **92**, 178302 (2004).

[43] J. P. Strachan, M. D. Pickett, J. J. Yang, S. Aloni, A. L. D. Kilcoyne, G. Medeiros-Ribeiro and R. S. Williams, "Direct identification of the conducting channels in a functioning memristive device," *Adv. Mater*. **22**, 3573-3577 (2010).

[44] H. D. Lee, B. Magyari-Köpe and Y. Nishi, "Model of metallic filament formation and rupture in NiO for unipolar switching," *Phys. Rev. B* **81**, 193202 (2010).

[45] G. A. Dearnaley, "Theory of the oxide-coated cathode," *Thin Solid Films* **3**, 161-174 (1969).

[46] W. E. Mutter, personal communication quoted by A. S. Eisenstein, "Oxide coated cathodes," *Advan. Electron. Electron Phys*. **1**, 1-64 (1948).

[47] G. Dearnaley, A. M. Stoneham and D. V. Morgan, "Electrical phenomena in amorphous oxide films," *Rep. Prog. Phys.* **33**, 1129-1191 (1970).

[48] D. J. Dwyer, S. D. Cameron and J. Gland, "Surface modification of platinum by titanium dioxide overlayers: A case of simple site blocking," *Surf. Sci.* **159**, 430-442 (1985).

[49] N. Zhong, H. Shima and H. Akinaga, "Rectifying characteristic of Pt/TiO_x/metal/Pt controlled by electronegativity," *Appl. Phys. Lett.* **96**, 042107 (2010).

[50] Linear I-V behavior [49], indicating filamentary conductance, has also been observed during the electroforming process of the devices.

[51] J. G. Simmons, "Generalized formula for electric tunnel effect between similar electrodes separated by a thin insulating film," *J. Appl. Phys.* **34**, 1793-1803 (1963).

[52] R. E. Holmlin, R. Haag, M. L. Chabinyc, R. F. Ismagilov, A. E. Cohen, A. Terfort, M. A. Rampi and G. M. Whitesides, "Electron transport through thin organic films in metal−insulator−metal junctions based on self-assembled monolayers," *J. Am. Chem. Soc.* **123**, 5075-5085 (2001).

[53] Definition of the fitting parameter [52], α varies. It might be caused by a nonrectangular barrier shape, the effective mass of the electron tunneling through the barrier, or a combination of both.

[54] D. A. Panayotov and J. T. Yates Jr., "n-type doping of TiO_2 with atomic hydrogen-observation of the production of conduction band electrons by infrared spectroscopy," *Chem. Phys. Lett.* **436**, 204-208 (2007).

[55] E. Finazzi, C. Di Valentin, G. Pacchioni and A. Selloni, "Excess electron states in reduced bulk anatase TiO_2: comparison of standard GGA, GGA+*U*, and hybrid DFT calculations" *J. Chem. Phys.* **129**, 154113 (2008).

[56] Ü. Özgür, Y. I. Alivov, C. Liu, A. Teke, M. A. Reshchikov, S. Doğan, V. Avrutin, S. –J. Cho and H. Morkoç, "A comprehensive review of ZnO materials and devices," *J. Appl. Phys*. **98**, 041301 (2005).

[57] Y. Matsui, M. Suga, M. Hiratani, H. Miki and Y. Fujisaki, "Oxygen diffusion in Pt bottom electrodes of ferroelectric capacitors," *Jpn. J. Appl. Phys.* **36**, L1239-L1241 (1997).

[58] J. –W. Park and C. J. Altstetter, "The diffusion and solubility of oxygen in solid nickel," *Metall. Trans. A.* **18**, 43-50 (1987).

Chapter 5

Filamentary Characteristics in TiO_2 Thin-Film Resistive Switching Devices

5.1 Introduction

In filamentary resistive switching, current in the low resistance state (LRS) flows through the conductive path in the insulating matrix while current in the high

resistance state (HRS) drops significantly due to the rupture of the conductive path [1-3]. The study of the micro-origin of conductive filament has attracted great interest in recent years. In the electrochemical metallization (ECM) system, the metallic filament arises from the migration of active metal atoms from the electrode (for example, Ag and Hg) [4-8]. Another type of conductive filament is buried within the oxide matrix and attributed to certain oxygen deficient phases of the bulk oxide. The second type of filaments was frequently reported in recent years, based on various measurement systems [9-16]. As a result of atom rearrangement, the size of such filaments could be down to the atomic scale.

In the search for promising oxide materials for resistive switching memories, special attention has been paid to their scaling capabilities. The filament mechanism shows that a switching device can be realized through a simple process of filament formation and rupture. In this context, too large dimensions, insufficient density, and the irregular distribution of filaments are among the challenges to device scaling. For CMOS compatible material and processing, the second type of filament has significant advantages. In this study, we use TiO_2 as the bulk oxide, TiN, Al, Ni and Pt as the electrodes. Conductive filaments composing of oxygen deficient phases have been reported in TiO_2 [13, 14]. Our device system belongs to the second type of filamentary switching.

Uniformly distributed filaments with high density are required in RRAM based device scaling. The resistive switching oxides always show electrically insulating behavior, with a high resistance in the gigaohm range. Typically, an initial high electrical field electroforming step composing of a breakdown process is needed for the virgin sample [10, 15, 17]. By applying a significantly high voltage or current, the resistance can be reduced by many orders of magnitude. A single filament or a few

randomly localized conductive filaments are believed to be formed during such a process [15, 18, 19].

In chapter 3, we investigated the resistive switching in the as-deposited TiO_2 thin films which show enhanced conductivity [20]. Without a high electrical breakdown initialization process, high density multiple conductive filaments were observed through CAFM under an intermediate voltage. Instead of within a small crater area, the filaments were found to form homogeneously across the oxide thin film. This work indicates that the fabricated TiO_2 thin films have good potential for high density memory applications.

Understanding the various filamentary characteristics is important in the development of RRAM based memory devices. Using the mechanism of charge injection and release, we explained the observed switching behavior in Chapter 3. We also investigated the negative differential resistance (NDR) behavior in a switching device in chapter 4, in which a charge storage mechanism using oxygen ions as the active source was successfully proposed [21]. In both chapters, we discussed a filament-interface model based on the amorphous TiO_2 thin film structures fabricated by the sputtering technique. This model is an integration of the two categories of resistive switching mechanisms, that is, the filament mechanism and the interface mechanism. Besides the filamentary effect, the interface between metal and oxide could also perform an important function. Instead of treating these two categories of mechanisms separately, an integrated model combining both effects is proposed. We have discussed examples of this model in chapter 3 and 4.

Electroforming has been reported to play an important role in resistive switching based devices [1, 3, 17]. In resistive switching, electroforming could refer to a process composing of high electrical breakdown to an insulating film before the switching

device works. In general, electroforming refers to an electrical process under an electrical field or current. For an electroforming process, a change of the applied voltage/current magnitude (including the compliance current/voltage) could lead to different electrical characteristics. The thin film composition (and structure), as well as the charge distribution could change during such a process, and as a result, the electrical resistance state is changed [17].

In this chapter, multiple-filamentary characteristics in TiO_2 thin films were further studied. Various I-V characteristics during an electroforming process were investigated. The CAFM was used to study the conductance, virtually forming localized nano-scale devices with a small distance between the CAFM tip and the bottom electrode. Field emission (FE) measurements, known as a tunneling effect in which electrons pass from an emitted material to the anode in the presence of a high electric field, were also performed. Unipolar and bipolar resistive memory effects were demonstrated. The mechanisms of the various switching behaviors are discussed using the integrated model incorporating both filamentary and interfacial effects.

5.2 Multiple filamentary characteristics

5.2.1 The current-voltage characteristics

A 7-nm-thick TiN layer was deposited on a $Pt/Ti/SiO_2/Si$ substrate by reactive sputtering. After that, an amorphous 20-nm-thick TiO_2 thin film was deposited by RF sputtering from a TiO_2 target, with the RF power at 250 W and Ar flow rate at 30 sccm (standard cubic centimeters per minute). Circular Al top electrodes 100 μm in diameter were fabricated by sputtering using a metal shadow mask. The current-voltage (I-V) measurements were performed at room temperature using an Agilent

4155C semiconductor analyzer. The device structure and the measurement setup is shown in Fig 5.1. The voltage current level and polarity were the parameters controlled in the electroforming process of the devices.

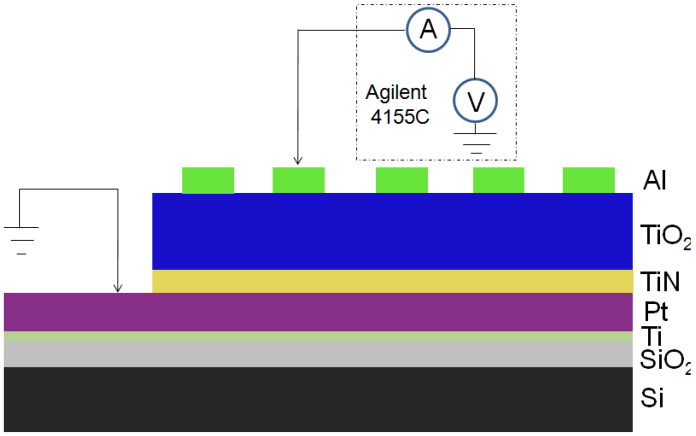

Figure 5.1: The schematic diagram of the device structure Al/TiO_2/TiN/Pt, and the simplified measurement setup.

The as-prepared TiO_2 thin films show good conductivity and an initial high electric breakdown electroforming process is not required. All the bias voltages were applied on the Al TE, with the Pt electrode grounded. During electroforming of the device, a bipolar switching behavior in linear ohmic characteristic with high repeatability in an Al/TiO_2/TiN/Pt device was observed, as shown in Fig 5.2. The voltage was swept between -1.0 and 1.0 V, at 0.2 V/step. It shows that the device was repeatedly switched from LRS to HRS at a negative voltage (~ -0.72 V). The switch from HRS to LRS started at ~ 0.52 V and completely finished at ~ 0.74 V, for which a switching tail can be clearly observed. The linear electrical characteristic is typically a filamentary behavior, and can be explained by conductive filaments formed in the oxide matrix. We attribute the switching tail to a multiple filamentary formation process. Formation and rupture of conductive filaments induced by the electrical field results in different resistance states.

Fig 5.3 shows the I-V curves in the electroforming process of another device. Both voltage magnitude level (range) and polarity are the parameters controlled in the electroforming process. The resistance of each level clearly presents a linear characteristic. Multiple filaments together contribute to the current flow.

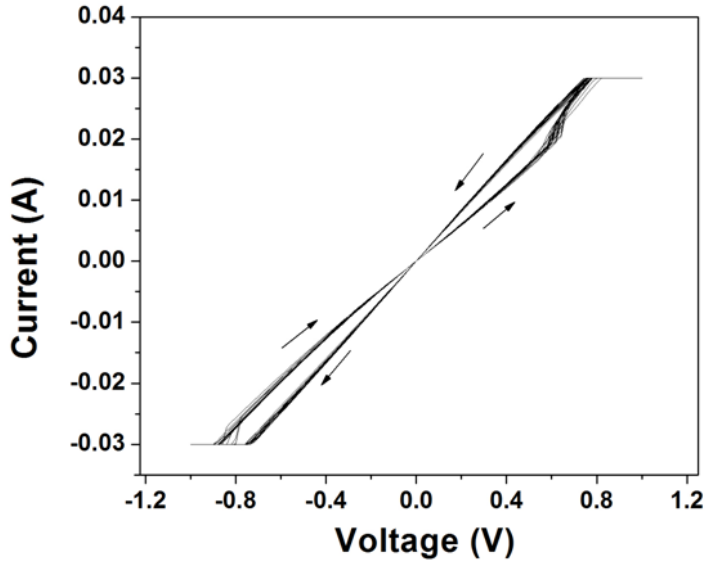

Figure 5.2: I-V curves in bipolar switching of a device between -1 and 1 V. The curves represent 50 experimental switching loops.

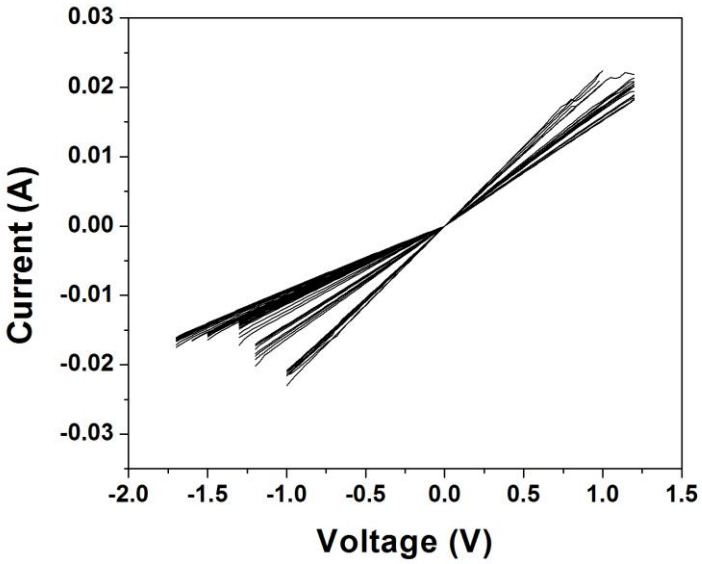

Figure 5.3: Electroforming I-V curves with linear characteristics in a switching device. Change of voltage range and polarity leads to different resistance states.

We also observed the electroformed I-V characteristic shown in Fig 5.4. With the current compliance firstly at 40 mA, the I-V curves with linear behavior were observed in the first scans (1^{st} to 7^{th}). Then the current compliance was increased to 60 mA. The subsequent scan (8^{th}) shows the current increasing in a linear characteristic at lower voltages (0 to ~ -0.8 V), but starting to drop as the voltage was further increased. The current dropping tail at higher voltages indicates a transition stage in resistance states. This could be due to oxidation reactions under a negative bias, which leads to the increase of the resistance state to a higher level. Then the device was continuously scanned from 0 to -1.2 V (9^{th} to 26^{th}). The linear behavior was consistently observed in the subsequent scans, and the resistance was found to slightly increase after each scan. With multiple filaments formed in the oxide, we postulate that a portion of the filaments were ruptured during the voltage sweeps. Fracturing of conductive filament could take place at the interface region or at the bulk oxide. Compared with the short-range process at the interface, the oxygen ion migration effect in the bulk oxide is more complicated.

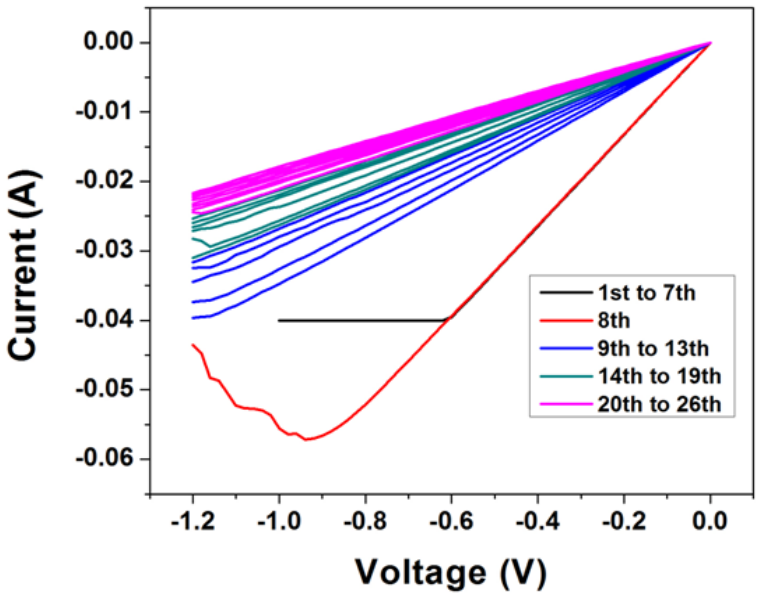

Figure 5.4: Electroforming of a device by continuously applying a negative bias.

Besides the electro-migration of oxygen ions in a resistive switching process, oxygen vacancies generated at the TiO_2/Pt interface were also reported to play a key role in resistive switching [17, 18]. TiN is widely used as a diffusion barrier in semiconductor industry. The insertion of a thin TiN barrier layer prevents such migration (oxygen vacancies) from the bottom interface. The migration of oxygen ions controlled by an electrical field applied to the top electrode contributes to the resistance change.

5.2.2 CAFM modification of the thin-film conductivity

With oxide thin films deposited on Pt electrode, the metallic AFM tip serves as a nano-size TE in the MIM structure. Using CAFM, the nanoscale current distribution and switching properties of the stacked thin film structure can be elucidated. A commercial atomic force microscope with a Pt coated silicon cantilever was used. Figs 5.5(a) and (b) show the CAFM morphology and the current map of the electrically formed surface, with a positive bias applied to a $5 \times 5\ \mu m^2$ area at 1 Hz in contact mode. The voltage bias varied from 1 to 10 V (current compliance was set at 10 nA). At lower voltages (1 to 9 V), the AFM writing had almost no effect on the topographic image, until a bias of 10 V was applied, that is, an electrical breakdown in the upper region of the scanned area. Conducting spots with high currents were formed. The observed spots mark the conducting paths that connect the surface with the bottom electrode (BE). The presence of the conducting spots shows that multiple filaments are formed in the thin film. The current mapping in 3D is shown in Fig 5.5(c). The density of filaments increased with the voltage and an improved conductivity was also observed at higher voltages. Electrical breakdown at 10 V significantly changed the thin film property in the upper region of the AFM image.

Conductive filaments formed at lower voltages shows that a high electrical breakdown electroforming process is not necessary in a switching process. The localized phase transition at lower voltages leads to the formation of conductive filaments in the bulk oxide.

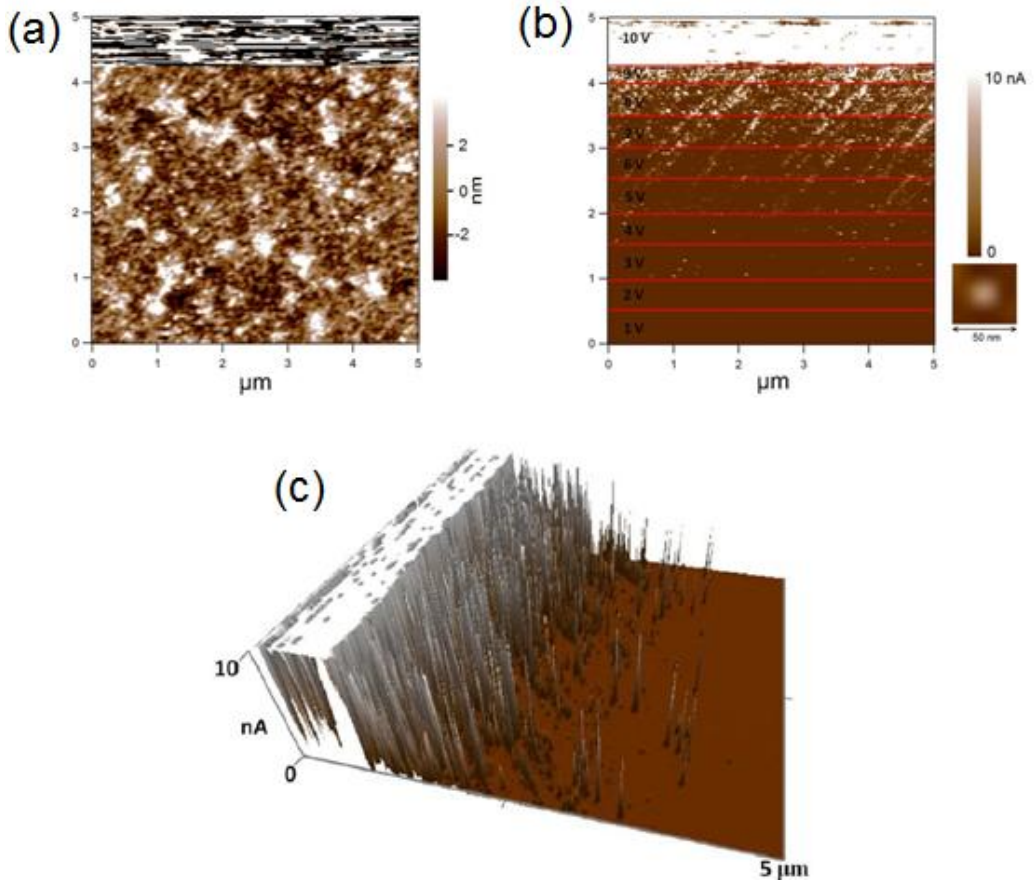

Figure 5.5: AFM measurements (CAFM) on TiO_2 films. (a) Topography and (b) current image under a positive bias (1 to 10 V). One conducting spot is shown on the lower right corner. (c) Current mapping image in 3D of the same area.

To evaluate the reproducibility of the AFM bipolar writing, a writing process by applying +/- 5 V bias to another area was performed, as shown in Fig 5.6 (current mapping image in 3D). A bias voltage of +5 V results in a more conducting surface, and a bias voltage of -5 V leads to a more insulating surface, with a variation of current flow between two to three orders of magnitude. Through oxidation and redox reactions, each filament could work as a resistive switching unit.

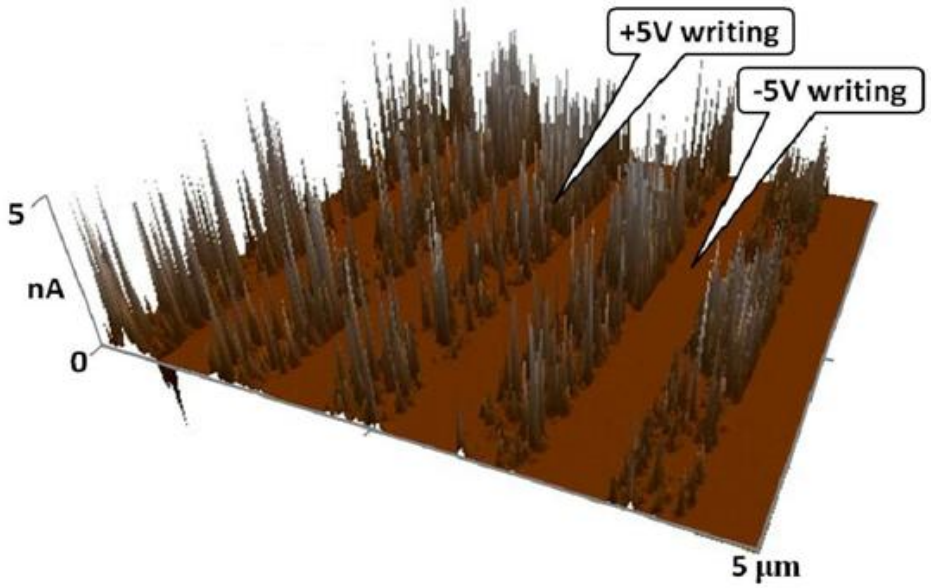

Figure 5.6: Current mapping image in 3D of another area with +/-5 V voltages applied.

Filaments could arise from an oxygen deficient phase of the oxide. Kwon *et al.* recently reported direct identification of electroformed nanofilaments with Magnéli phases inside TiO_2 films [13, 14]. According to the report by Weber *et al.* [22], Ohm's law still works in the atomic scale. Although the generality of this work to other materials needs to be further evidenced, we use Ohm's law for a simple calculation in our devices. With the assumption of Magnéli phase filaments formed in the oxide, we estimate the number of filaments working in a switching device, based on the data shown in Fig 5.2. Also for a simple calculation, we refer the resistivity of Magnéli phase filament to 2 mΩ cm [23]. Using

$$R = \rho \frac{l}{s}, \tag{1}$$

the resistance of a single filament is then calculated as 5×10^5 Ω. Each filament is simply treated in a cylinder shape 10 Å in diameter, and 20 nm in length (the oxide

thickness). The number of the filaments for current flow in Fig 5.2 is estimated at ~10^4.

The work by Kwon *et al*. [13] is a good example for the study of conductive filament in oxide. However, understanding of the micro-origin of conductive filament is still limited, which is due to the great difficulties and challenges in both experimental analysis and theoretical calculations. Besides the electroformed conductive filament in the oxide reported by Kwon *et al*., the conductive filament could also exist in the as-deposited thin film. In the next section, we will show the unipolar switching behavior, which shows linear ohmic I-V characteristic in the as-deposited oxide film. The simple calculations here are to show the multiple filamentary properties of the switching device.

5.3 Unipolar switching behavior

Unipolar switching shows the resistive switching at two values of applied voltage of the same polarity. After an electroforming process, the unipolar switching behavior was observed, as shown in Fig 5.7. Fig 5.7(a) shows the unipolar switching behavior in a linear scale, while Fig 5.7(b) shows the same curves in a semilogarithmic scale. The current compliance was set at 30 mA. The device was firstly at an intermediate resistance state (IRS). As the external voltage increased from zero to a threshold voltage (2.0 V), a sudden increase of current was observed. The resistance state was switched to a LRS state. As voltage increased again from zero, a sudden current drop occurred at ~ 0.68 V. A HRS state was then formed. This is consistent with the work by Liu *et al*. [24] for a TiO_2 based device, in which a ~ 0.7 V switching voltage from LRS to HRS and a ~ 2.0 V switching voltage from HRS to LRS were also reported.

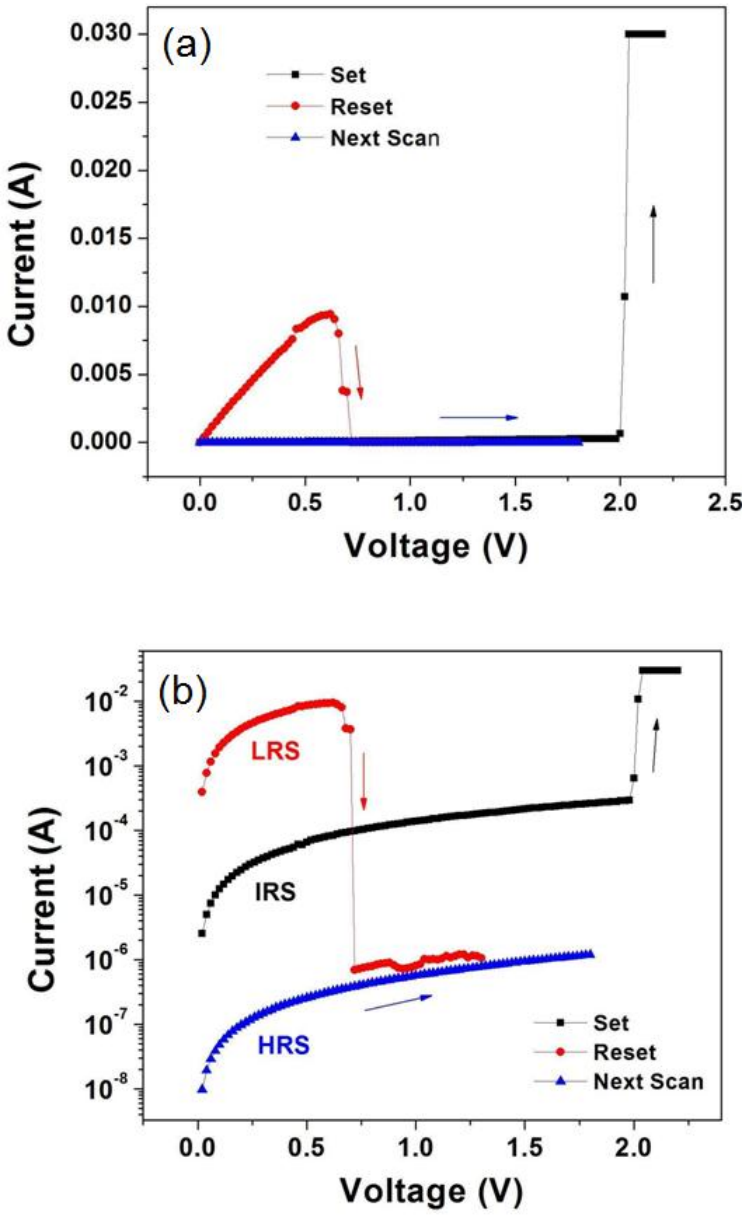

Figure 5.7: (a) I-V curves in unipolar switching of an Al/TiO_2/TiN/Pt device under a positive bias. (b) The same curves in a semilogarithmic scale.

Instead of an insulating state, the IRS curve indicates good conductivity of the thin film. The I-V curve of the IRS state is further depicted in Fig 5.8(a). The curve is divided into three segments, with each segment displaying a typical linear characteristic. The first segment was from 0 to 0.48 V. A shift of current was found at ~ 0.44 V, followed by a fluctuation of current to 0.48 V. The second segment was

from 0.50 to 1.44 V. The third segment was from 1.46 to 1.98 V, with a shift of current at 1.92 V. The three-segment I-V characteristic presents a shift of resistance to a lower level after each stage (R1→R2→R3). Extraction of oxygen ions under a higher positive voltage results in more filaments formed in the oxide. The linear ohmic behavior of the initial IRS state indicates that conductive paths or filaments could be inherently formed in the as-deposited oxide thin film before an electrical process. In the future works, a combined study using *in situ* HRTEM and variable temperature measurement systems will be carried out for this purpose.

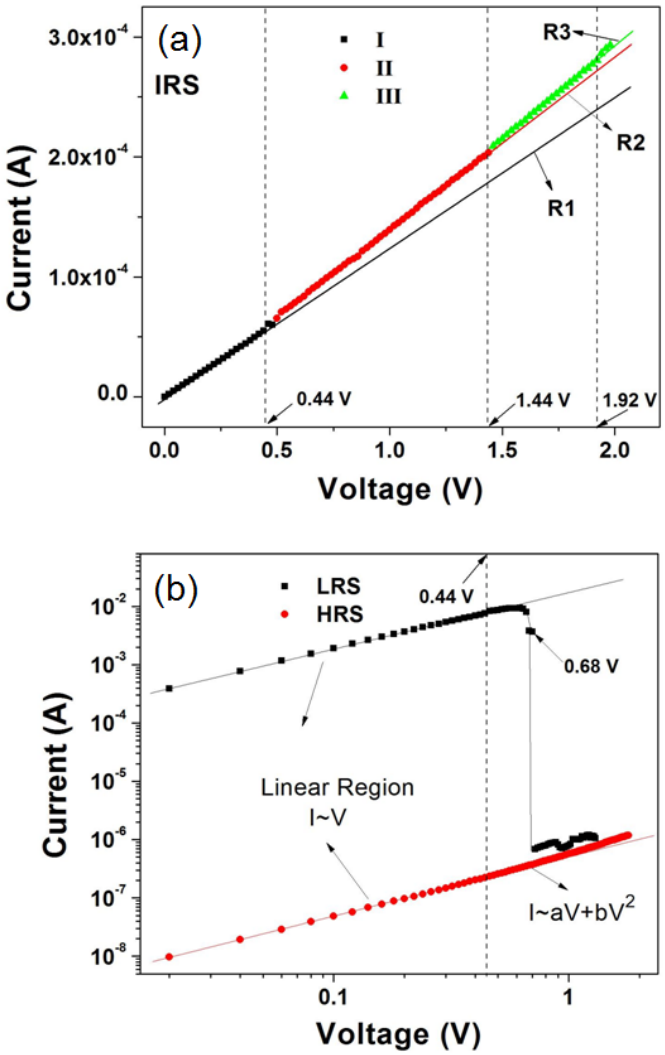

Figure 5.8: (a) I-V characteristic under the intermediate resistance state (IRS). (b) I-V characteristics under the low resistance state (LRS) and the high resistance state (HRS), in double-logarithmic scale.

To further understand the conduction and switching mechanism, the I-V curves in the LRS and HRS states were replotted in a log-log scale, as shown in Fig 5.8(b). The I-V characteristics followed a linear ohmic behavior at low voltages, indicating filamentary conductance. For the LRS state, a shift of current occurred at 0.44 V, and current quickly dropped at 0.68 V. For the HRS state, the ohmic characteristic ($I \propto V$) at low voltage was followed by a quadratic term at higher voltage, that is, $I \propto aV + bV^2$, which indicates space-charge-limited current (SCLC) injection [25, 26]. Charge capture and release at defect sites contributes to the current flow.

5.3.1 Space charge effect

Redox and oxidation reactions result into different resistance states. In terms of the SCLC controlled by the trapped charge density, the leakage current at higher voltages follows the equation:

$$J = \frac{9}{8}\epsilon_0\epsilon_r\mu_p\frac{V^2}{d^3}, \quad (2)$$

where J is the current density, ϵ_0 the permittivity of free space, ϵ_r the permittivity of the thin film, μ_p the mobility of the charge carriers, V the bias voltage, and d the thickness [26].

At lower voltages, the I-V curve follows a linear characteristic, indicating a filamentary conducting behavior. As the voltage increases, the current due to space charge effect starts to increase and finally dominate the current flow at the higher voltage range. For the purpose to investigate the space charge current under different scan rates, CAFM I-V scans of the thin films were performed.

Fig 5.9 and Fig 5.10 show the shapes of the CAFM I-V curves of the thin film by changing the scan rate. At a slower scan rate (0.1 V S^{-1}), the curve exhibited an oscillating characteristic. Sharp increase and decrease of currents were found during

the scan from 0 to 9 V (Fig 5.9). In comparison, the curve obtained at a higher scan rate (10 V S^{-1}) was free of such a characteristic (Fig 5.10). The shape of the I-V curves varied with the scan rate. At a higher scan rate, a small amount of locally injected charges will be involved [27, 28]. While at a lower scan rate, significant charge injection and release at defect sites takes place. At the higher scan rate, the majority carrier (electrons) dominates the current flow.

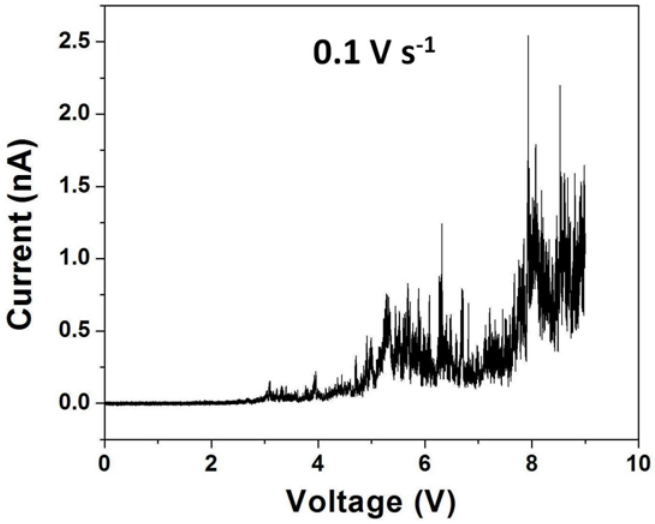

Figure 5.9: Sample/Tip I-V characteristics (CAFM) of TiO_2/Pt thin film stacked structure at a sweep rate 0.1 V S^{-1}.

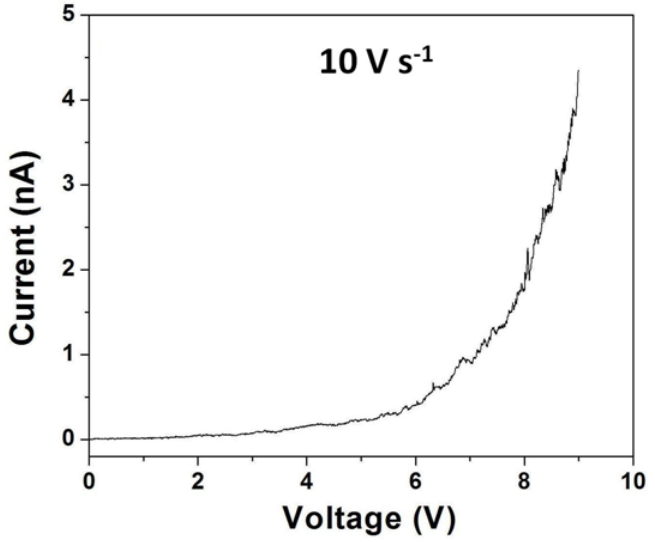

Figure 5.10: Sample/Tip I-V characteristics (CAFM) of TiO_2/Pt thin film stacked structure at a sweep rate 10 V S^{-1}.

The behavior shown in Figs 5.9 and 5.10 can be explained by the effect of charge injection and release. Oxygen vacancy is a common defect in TiO_2. Trapping and detrapping of oxygen ions at oxygen vacancies are involved in a charge injection and release process. The sharp increase and decrease of current could be due to such a process. In the Kröger-Vink notation, the trapping of oxygen ions can be expressed as,

$$V_O^{\cdot\cdot} + \frac{1}{2}O_2 + 2e \rightarrow O_O^{\times}. \quad (3)$$

A charge injection involved with negative oxygen ions occurs. On the other hand, the extraction of oxygen ions from the lattice leads to a charge release process,

$$O_O^{\times} \rightarrow V_O^{\cdot\cdot} + \frac{1}{2}O_2 + 2e. \quad (4)$$

Charge injection and release (oxidation and redox reactions) assisted by electro-migration of oxygen occurs in the resistive switching process.

5.3.2 FE measurement

While it is difficult for an oxide insulator to display electron field emission, the enhanced conductivity of the oxide and the metallic properties of conductive filaments in the thin film structures illustrate that field emission (FE) could take place under an electrical field. We carried out FE measurements to further investigate the filamentary characteristic of the oxide thin films, as well as the charging effect during the emission process. The FE experiment was carried out using a two-parallel-plate configuration in a vacuum chamber with the pressure about 5×10^{-7} Torr at room temperature. The distance between the electrodes was kept at 20 μm. A Keithley 237 voltage source measurement unit (SMU) was used to measure the emission current.

Fig 5.11(a) shows a current density *versus* voltage (J-V) curve for a TiO_2/Pt thin film stacked structure. The current density changed slowly with voltage at lower voltages. Then the current emission was "turned on" at ~ 980 V, after which an

oscillating characteristic was observed at the higher voltage range. In comparison, Fig 5.11(b) shows a FE measurement for a TiO_2/TiN structure. A similar characteristic was also observed, with the "turn on" voltage at ~ 850 V. At higher voltages, the current emission oscillated with the electric field, but in a more frequent fluctuating behavior.

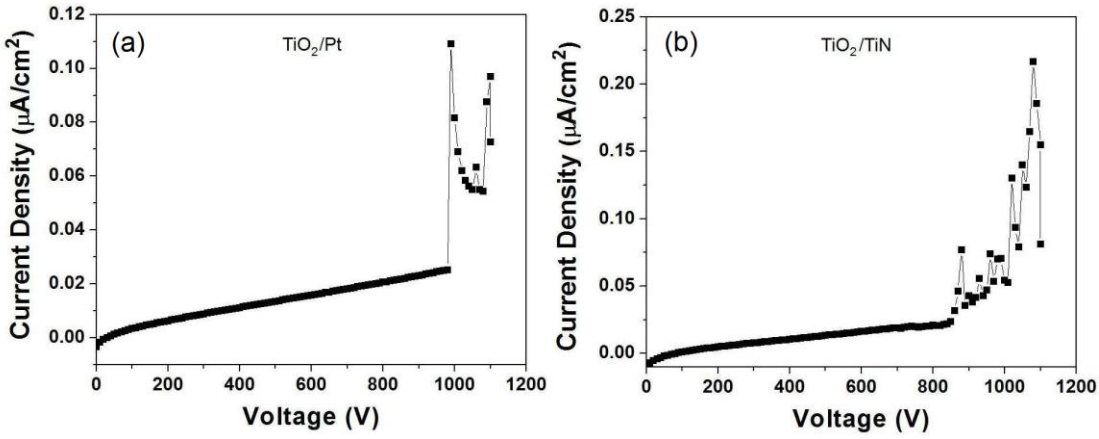

Figure 5.11: (a) Field emission (FE) J-V characteristic of a TiO_2/Pt thin film stacked structure. (b) FE J-V characteristic of a TiO_2/TiN thin film stacked structure.

In comparison to the localized formation of conductive filaments by a CAFM probe electroforming process, the FE experiments provide a method to form a large number of filaments across the oxide thin film. The lower emission current at the low voltage range could be due to the filaments formed in the as-deposited sample. Increasing of voltage to a threshold value leads to much more filaments formed under a high electrical field. At the same time, "fracturing" of filaments also occurs, and the J-V curve presents an oscillating characteristic. The electrical field under high voltages in the FE experiment is comparable to that of the I-V measurement of a switching device using an I-V probe station system.

Similarly to an electroforming process using a normal I-V setup, continuous electroforming using the FE method could lead to different J-V characteristics,

including the “turn on” voltages, as shown in Fig 5.12. Such difference could be due to the bulk (or localized) composition or structure changes induced in the first voltage sweep process. Fig 5.12(a) shows a “turn on” voltage at 960 V, and a lower emission current for TiO_2/Pt, as a comparison to that shown in Fig 5.11(a). For the structure of TiO_2/TiN, the J-V curve in Fig 5.12(b) shows a “turn on” voltage at 930 V (850 V in Fig 5.11(b)). A shift of “turn on” voltage (up to 100 V) was observed in all the measurements.

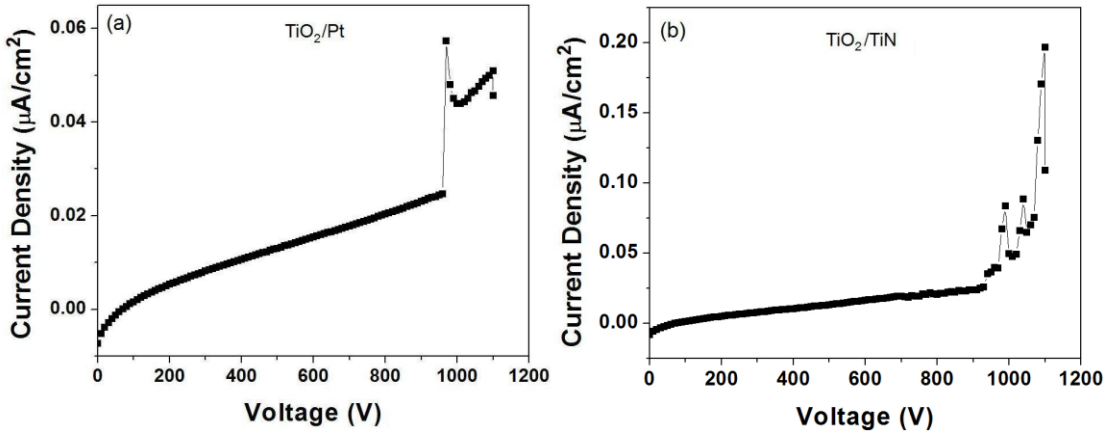

Figure 5.12: Continuous FE J-V measurements of the stacked structures: (a) TiO_2/Pt (b) TiO_2/TiN.

The FE J-V characteristics (Figs 5.11 and 5.12) present an oscillating behavior, which is consistent with that observed in an electroforming process of an Al/TiO_2/TiN/Pt device, as shown in Fig 5.13. A current jump was observed at ~ 0.5 V, and followed by a fluctuation of current with voltage at the higher voltages. With a positive voltage applied, the extraction of oxygen ions could be accompanied by the injection of oxygen ions. Frequent formation and rupture of filaments due to charge trapping and detrapping assisted with oxygen ions is attributed to the observed oscillating characteristic.

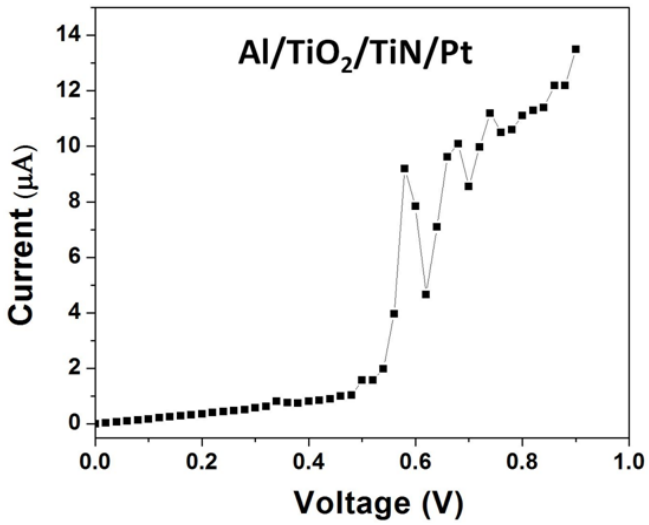

Figure 5.13: Electroforming I-V characteristic of an Al/TiO_2/TiN/Pt device under a positive bias.

5.4 Interface charging effect

Besides the various linear characteristics shown in the electroforming process (e.g. Figs 5.3 and 5.4), the I-V characteristics in an exponential behavior was also observed. Fig 5.14(a) shows the I-V curves during an electroforming process of a device. A typical exponential characteristic is observed. In the electron tunneling regime, this phenomenon can be explained by the model shown in Fig 5.14(b). With oxygen ions continuously injected into the IL regions, modification of the interface barrier leads to different resistance states. The device was firstly scanned from 0 to -1.0 V and the compliance current was set at 30 mA (1^{st} to 4^{th}). The resistance state was at Phase I (①). Then the compliance current was increased to 90 mA. The subsequent scan shows that the I-V curve shifts from the first scans at the higher voltage range (5^{th}). The transforming stage was marked as ①. The resistance state was then kept at Phase II (6^{th} to 11^{th}). Then the maximum voltage was increased from -0.9 to -1.2 V. After another transforming stage (②, 12^{th}), the I-V curves overlapped again with each other

(13th to 23rd), indicating the resistance state went to a higher level (Phase III). Finally, the voltage was further increased to -1.4 V in the 24th scan. A sudden current jump was observed and continuous scans show the I-V curves in a linear characteristic (25th to 30th). This transforming stage was marked as ③.

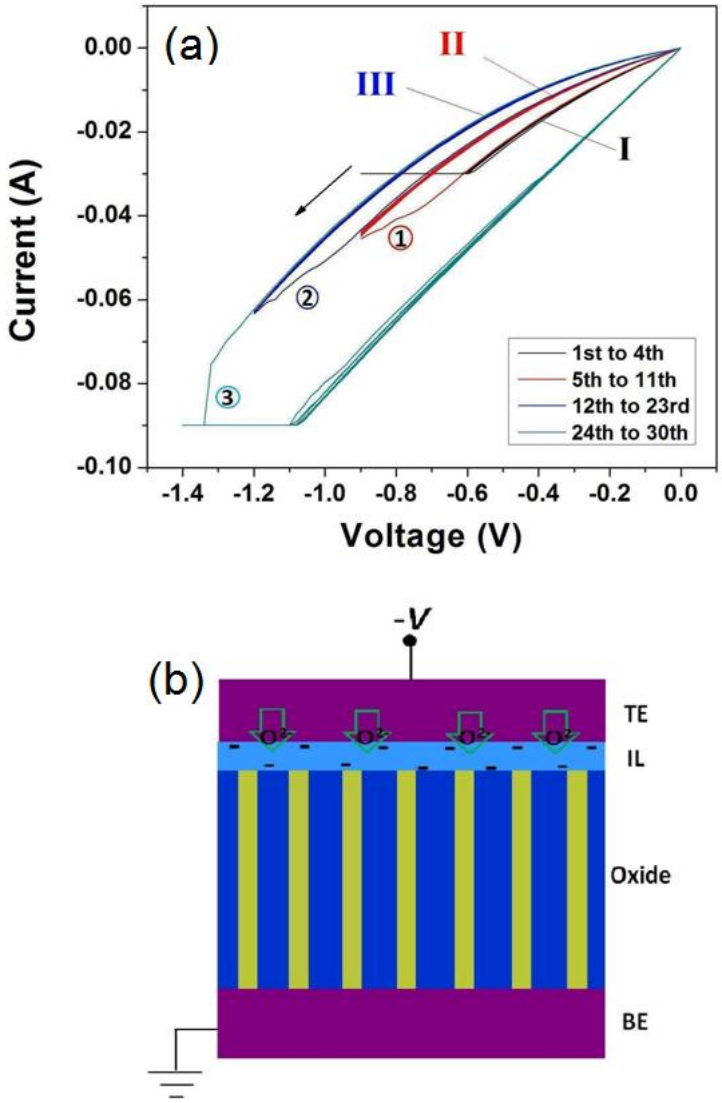

Figure 5.14: (a) I-V electroforming characteristic of an Al/TiO_2/TiN/Pt device by continuously applying a negative bias. Phase I, II and III are resistance states from the lowest to the highest. ①, ②and ③ are the transforming stages between different resistance states. (b) Schematic illustration of a filament-interface model and injection of negative ions under a negative bias. Conductive filaments are formed in the bulk oxide matrix. An interfacial layer (IL) lies at the interface between TE and the bulk oxide. The filaments are simply treated in a uniform shape.

Oxidation of the conductive filaments could result in an insulating layer (IL) at the metal/oxide interface. Electrons need to tunnel through the IL with filaments as the conducting bridges. Charge injection of oxygen ions under a negative bias transforms the resistance state to a higher level. Injection of oxygen ions at the first stage (①) pushes up the trapping barrier, and a higher electrical field is needed for a further charge injection (②). With an insulating layer at the interface, electrons need to tunnel through to the other side. The tunneling current in a metal-insulator-metal system can be described by the Simmons model [29, 30],

$$J = \frac{e}{2\pi h d^2}\left\{\left(e\varphi_0 - \frac{eV}{2}\right)\times\exp\left[-\frac{4\pi d}{h}(2m)^{1/2}\alpha\left(e\varphi_0 - \frac{eV}{2}\right)^{1/2}\right]\right.$$
$$\left.-\left(e\varphi_0 + \frac{eV}{2}\right)\times\exp\left[-\frac{4\pi d}{h}(2m)^{1/2}\alpha\left(e\varphi_0 + \frac{eV}{2}\right)^{1/2}\right]\right\} \quad (5)$$

where h is Planck's constant, α is a unitless parameter used for fitting, m is the rest mass of electron, e is the elementary charge, φ_0 is the barrier height and d is the insulator thickness. Based on Eq. (4), the I-V curves representing different resistance states (Phase I and II) in Fig 5.14(a) are fitted with the Simmons' model, as shown in Figs 5.15 and 5.16 respectively. A fitting parameter α =1 is used [31]. With the thickness in a constant value, a higher barrier height 1.66 eV is found for the Phase II resistance state, compared to a 1.60 eV barrier of Phase I.

Unlike ①and ②, the transforming stage ③ is an electrical breakdown process, after which a linear behavior indicating filamentary conductance is observed. The trapped charges are released, and conducting filaments become direct contact with the electrode through significant redox reactions. Besides a titania layer formed layer formed at the interface, the thin interfacial layer (~1.2 nm) could also be composed of Al(Ti)O_x, as a result of the reaction between the TE and underlying bulk oxide layer.

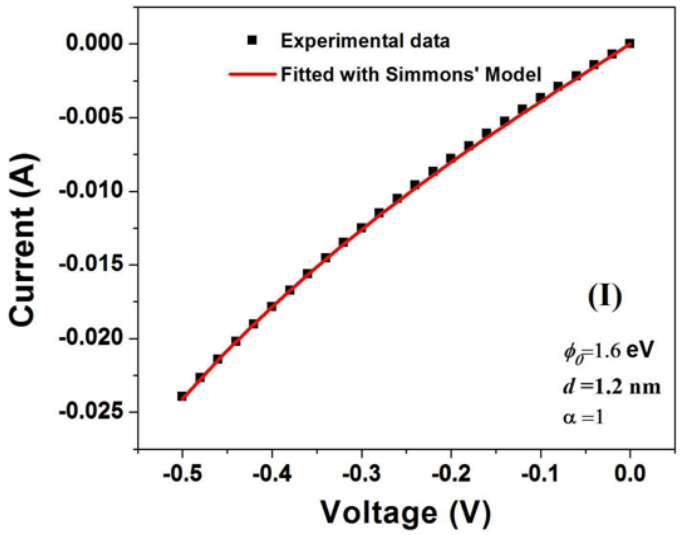

Figure 5.15: Fitting of current *versus* voltage using Simmons' model at resistance state Phase I. The parameters used in calculation are indicated on the plots.

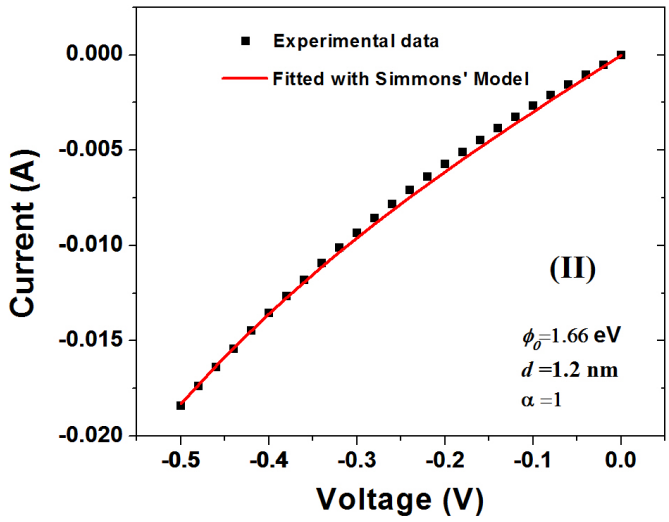

Figure 5.16: Fitting of current *versus* voltage using Simmons' model at resistance state Phase II. The parameters used in calculation are indicated on the plots.

5.5 First-principles modeling of the filament

In chapter 4, we have investigated the TiO_2 structure with a single vacancy. The calculations show that oxygen vacancy is a deep band gap state and the effect of

vacancy on the conductivity is negligible, due to the strong electron localization. The recent report by Kwon *et al*. shows that conductive filaments are composed of Magnéli phase [13]. The Magnéli phase is known to have an order of successive oxygen vacancies. Based on theoretical modelling, Lee *et al*. proposed a metallic atom chain structure by using ordered oxygen vacancy structures in NiO [32]. On the basis of a rutile TiO_2 structure, Park *et al*. reported that the configuration of two oxygen vacancies could lead to a stable structure [33]. With oxygen vacancies in the nearest distance, most of the excess charges in the defect states are localized at the neighbouring Ti atoms [33]. These Ti atoms could form an electron flow path which is expected to increase the conductivity of TiO_2.

The formation of a metallic atom chain can be described by the configuration shown in Fig 5.17. Fig 5.17(a) shows the cell is in an insulating state. Through a reduction process, a metallic chain composed of Ti atoms is formed and the structure is transformed to a conducting state (Fig 5.17(b)). In this section, we will use first-principles modelling to explain the observed unipolar switching behavior, for which we attribute to a metallic-insulating transition under a controlled electrical field.

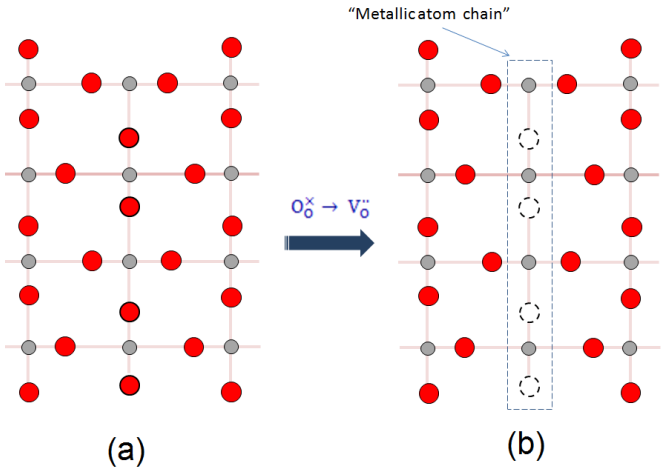

Figure 5.17: Formation of a metallic atom chain through a reduction process. The removal of oxygen ions leaves oxygen vacancies behind (from (a) to (b)). Red – O atom, grey –Ti atom.

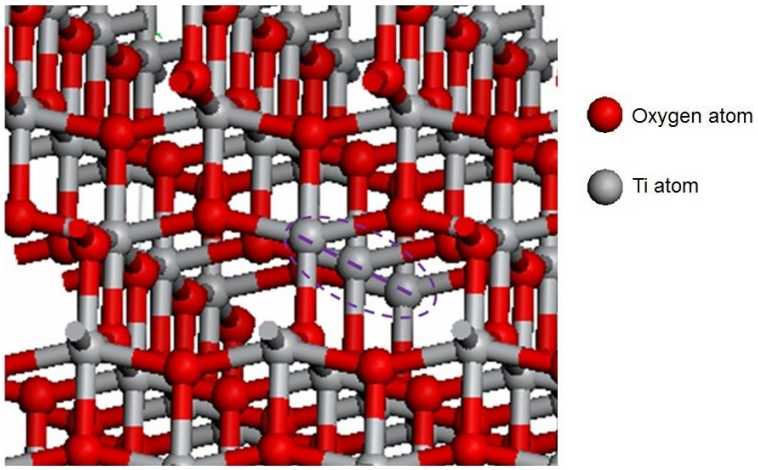

Figure 5.18: Atomic structure of anatase TiO_2 with a Ti-atom chain after oxygen-atom removal. All oxygen vacancies are on the [100] direction.

Fig 5.18 shows the atomic structure after ordered oxygen vacancies are formed on the [100] direction. Density functional calculations using the Vienna *ab initio* simulation package (VASP) [34] were carried for anatase TiO_2. A supercell of 3×3×1 with a total of 36 Ti atoms and 72 O atoms was used. The calculation setting details are consistent with that described in Chapter 4 [21]. The Ti-atom chain was created by removing two oxygen atoms in the [100] direction. (Besides the theoretical modelling, more experimental works will be followed in the future works - chapter 6).

The release of O_2^{2-} from a TiO_2 neutral cell leaves two oxygen vacancies and a charge state +2 is then formed. The formation energy barrier for the process is calculated from:

$$E_b = E_{tot}(TiO_2 + 2V_o - 2e) - E_{tot}(TiO_2) + E(O_2) + 2E_f \quad (6)$$

where $E_{tot}(TiO_2 + 2V_o - 2e)$ is the total energy of the cell containing two vacancies (Ti-atom chain), $E_{tot}(TiO_2)$ is the total energy of the cell without vacancy and $E(O_2)$ is the energy of oxygen molecule and E_f is the Fermi energy. The Fermi level E_f is

the energy of the electron reservoir, with reference to the valence band maximum (VBM).

The formation energy is also related to the chemical potential of oxygen (μ_O). The actual value of μ_O is related to the oxygen environment. In the extreme O-rich limit, $\mu_O = 0$. The oxygen chemical potential varies with the different oxygen environment at each single electrical measurement, which leads to different formation energies. Fig 5.19 shows the formation energy barrier as a function of the oxygen chemical potential. The unipolar switching behavior shown in Fig 5.7 illustrates that the application of 2 V leads the device from an insulating state to a metallic state. It is consistent with the formation energy (Point A) shown in Fig 5.19. After the detrapping of a O_2^{2-} form a TiO_2 cell, a Ti atom chain is then formed.

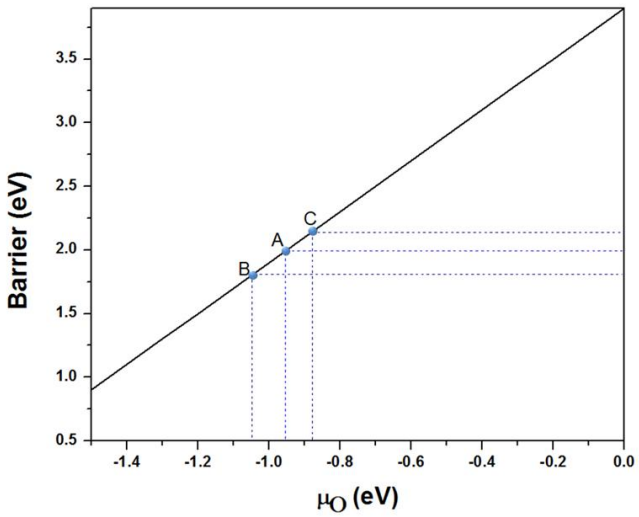

Figure 5.19: Formation energy as a function of oxygen chemical potential. A – formation energy of 2.0 eV; B – formation energy of 1.8 eV; C – formation energy of 2.1 eV.

Based on the report by Liu *et al*. [24], Fig 5.20 shows the unipolar resistive switching curves of a TiO_2 based device. It shows the change of resistance states from HRS to LRS at ~ 1.8-2.1 V. Compared with the threshold voltage 2 V in Fig 5.7, a random characteristic threshold voltage was observed for the transition from HRS to

LRS. Such random characteristic of the formation energy barrier behavior has also been reported by Kim *et al*. [35]. We plotted the formation energy as a function of the oxygen chemical potential in Fig 5.19.

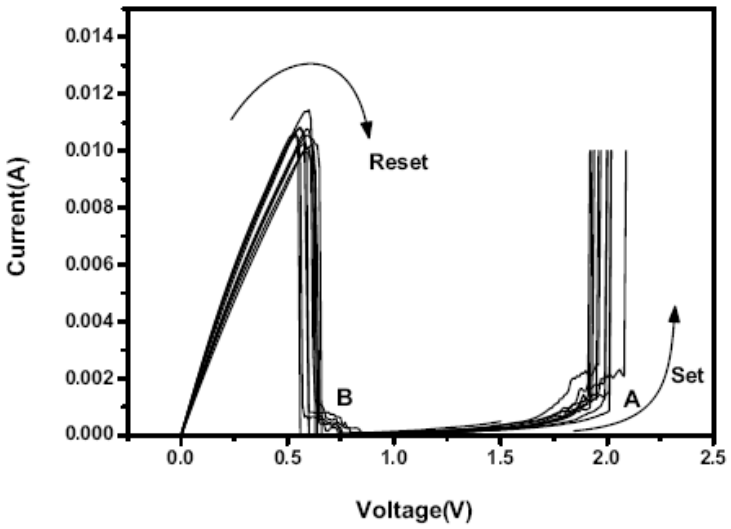

Figure 5.20: (a) Unipolar resistive switching I-V curve of a TiO_2 based device [24].

Fig 5.20 shows the transition from LRS to HRS at ~ 0.7 V, which value is close to the 0.68 V in Fig 5.7. Fig 5.21(a) shows the total density of state of the ($TiO_2 + 2V_o - 2e$) cell. Compared with a pristine TiO_2 cell, a defect state 0.76 eV above the middle of the band gap is introduced. This is consistent with the 0.68 and 0.7 V achieved in the unipolar switching I-V curves. Using the SV charge storage mechanism, this can be understood as a charge trapping process involved with oxygen molecular ions. Opposite to a O_2^{2-} release process, the charge capturing involved with oxygen ions leads to an oxidation process, and finally to an insulating state. The random characteristic of the threshold voltage from LRS to HRS could be due to the different charge states (and effects) formed during the voltage sweeping process, as well as the multiple filamentary characteristics of the device structure. In contrast, the rupture of filament as a result of Joule heating effect due to current flow has also been discussed [36-38]. By assuming a conductive filament with certain dimensions, the

threshold voltage as a function of the filament dimension has been reported by Ielmini *et al*. [38]. However, this model has great difficulties in explaining the random characteristics of the threshold voltages in the reports, as well as the transition from HRS to LRS.

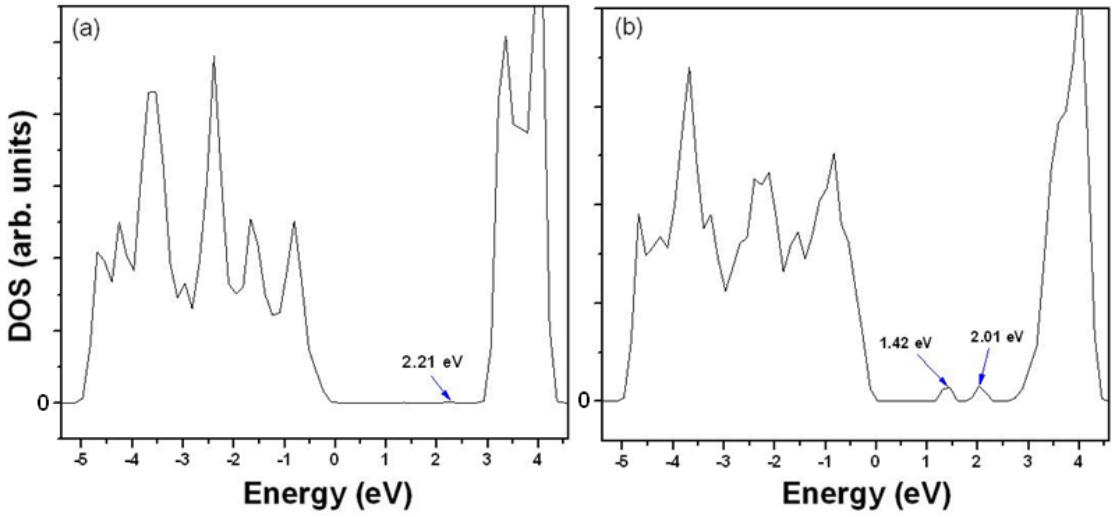

Figure 5.21: Total density of states of TiO_2 with: (a) $2V_o - 2e$, and (b) 2 V_o.

The neutral charge state of the di-vacancy structure is also investigated, for which a much higher formation energy barrier is needed. The +2 charge state is more stable. With an electrical field applied, electrons flow through the Ti atom chain with a +2 charge state. Unlike Fig 5.21(a), Fig 5.21(b) shows the total density of state without the +2 charge state. Compared with the valence band, there is a more significant change at the conduction band which is mainly contributed by the Ti3*d* orbitals. For the neutral di-vacancy structure, two band gap states 1.42 eV and 2.01 eV can be clearly observed above the VBM, which are from different Ti3*d* states. At the +2 charge state, both the two peaks are strongly suppressed. Only a weak intensity can be found for the upper peak, with the position shifting to a higher energy value (the lower peak is very weak, and difficult to display).

The metallic behavior of the di-vacancy structure may come from the t_{2g} and e_g character of the Ti3*d* orbitals, as shown in Fig 5.22. Fig 5.22 shows the schematic pictures of Ti3*d* orbitals in TiO_2 octahedral structure. The e_g orbital are pointing toward oxygen atoms. The creation of oxygen vacancies leads to the depletion of electron density in e_g orbitals. The excess electrons in equatorial di-vavancy are drawn from e_g orbitals and reside in t_{2g} orbitals, which results to the increase of the metallic interaction between the Ti atoms (formation of the Ti-atom chains). Such kind of Ti-Ti bonds, which are composed of degenerate t_{2g} orbitals, have been reported in $LiTiO_2$, known for its superconducting properties [39, 40]. The charge ordering in a certain direction plays an important role in determination of the conductivity.

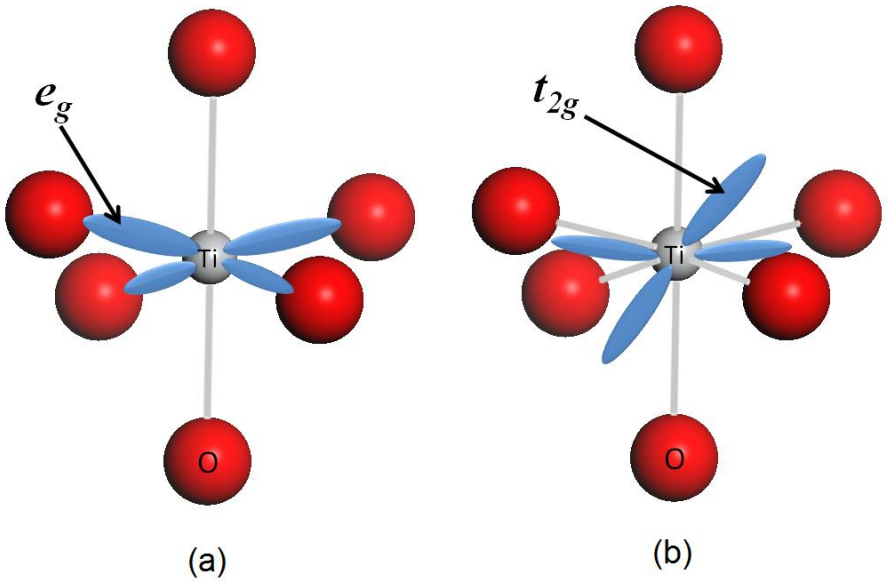

Figure 5.22: Schematic of Ti3*d* orbitals (a) e_g orbitals, (b) t_{2g} orbitals.

5.6 The integrated model

The charge effect in the unipolar switching can be further depicted by the I-V characteristics shown in Fig 5.23. The subsequent scan in a higher voltage range leads

the device to a LRS state. A significant fluctuation of current was observed before the device was finally switched to a HRS state. The oscillating characteristic implies that it comes from a charge injection and release process. As the voltage increased from zero to a threshold value (~ 0.48 V), the current started to shift from the trend, until a sudden current drop at 0.68 V. Based on the fist-principles calculations, we attribute the 0.68 V to a charge trapping process involved with oxygen molecular ions.

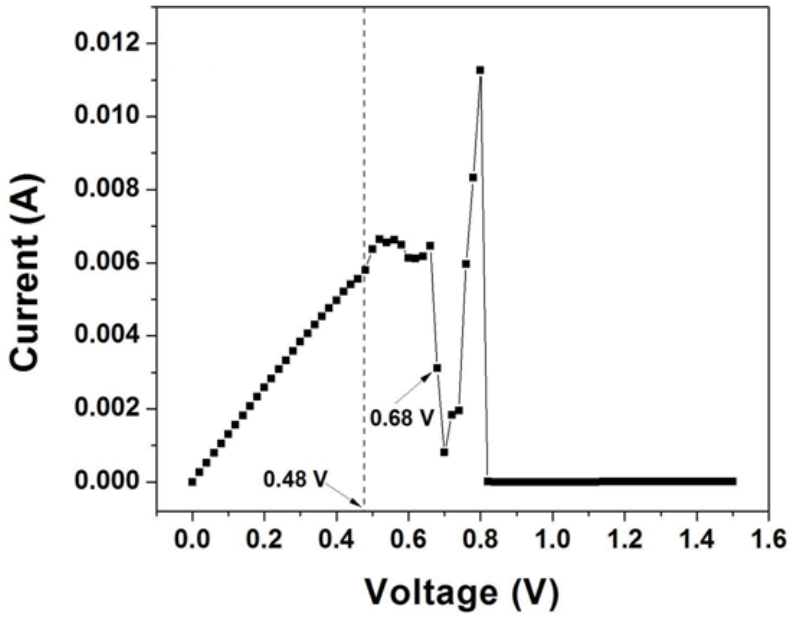

Figure 5.23: I-V curve of an Al/TiO_2/TiN/Pt device within a unipolar switching process.

We attribute the threshold 0.48 V (~ 0.46 V in Fig 5.7) to a charge release process. Using impedance spectroscopy, Lee *et al.* recently reported a 0.46 eV activation energy in TiO_2 thin films [41]. This is also consistent with the formation energy barrier obtained in chapter 4 [21]. Oxidation through an oxygen ion capturing process results to a HRS state, and reduction through an oxygen release process leads to a LRS state. Fig 5.24 shows the total energy of the system as a function of the generalized lattice coordinate. Capture and release of oxygen ions between different

solid state phases leads to the observed oscillating characteristic. Different resistance states are formed through microstructure changes.

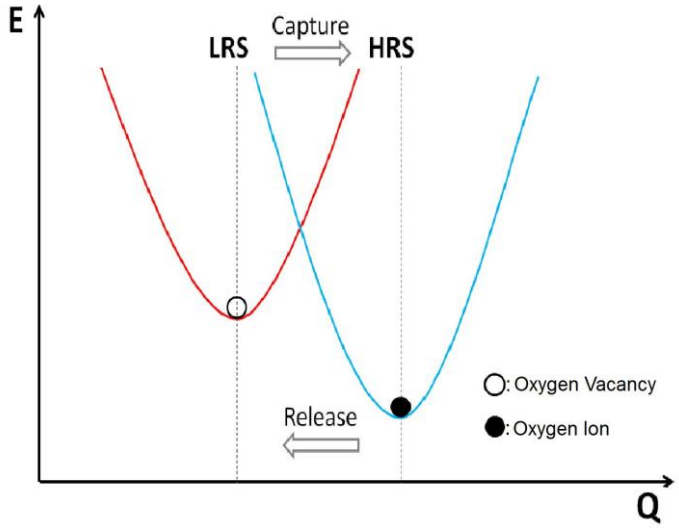

Figure 5.24: Schematic configuration coordination diagram of charge transfer assisted by oxygen ions between different solid phases (resistance states).

By changing the electroforming processes, different I-V resistive switching behaviors were observed even in the same material system [17, 42]. In principle, a RRAM device works by fixing the resistance state at a high voltage and then measuring the current at a much lower voltage. In this context, there are many different resistance states for a thin film structure. A HRS state is defined relatively to another LRS state. Summarizing the results for the measurements, the observed filamentary characteristics can be explained by the switching mechanism schematically shown in Fig 5.25. Fig 5.25(a) shows an insulating (or semiconducting) IL formed at the interface. Current flows through an electrode-filaments-IL-electrode structure. Conductive filaments formed in the bulk oxide act as bridges for current flow. Electrons need to tunnel through a thin barrier. Through charge injection and release assisted by oxygen ions, different interface barriers are then formed. Besides

the change of barrier height, the injection of oxygen ions could result to different barrier shapes (Fig 5.14). Using the same fitting parameter, a better fitting performance was achieved in Phase I resistance state (Fig 5.15), compared to that of Phase II (Fig 5.16). This is due to the non-rectangular barrier shape formed at the interface, for which a further adjustment of the fitting parameter α is required.

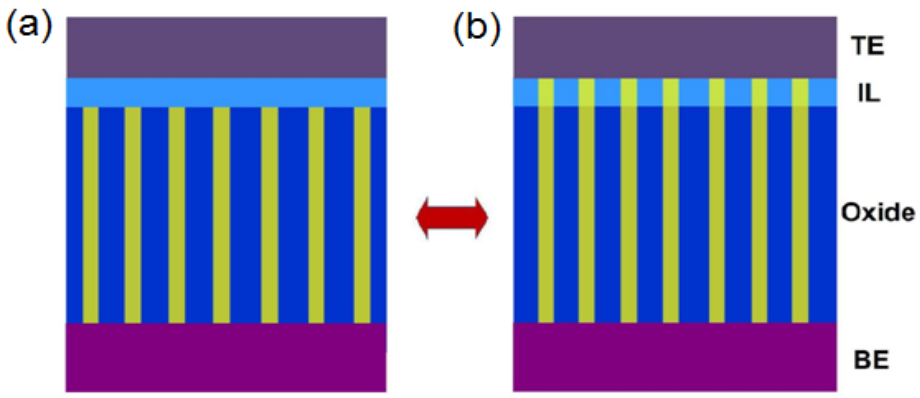

Figure 5.25: A schematic diagram for mechanism of resistive switching effects: (a) An insulating (or semiconducting) interfacial layer (IL) zone is formed at the interface between TE and the bulk oxide; (b) Conductive filaments are in direct contact with the two electrodes.

A symmetrical barrier will lead to a symmetrical I-V characteristic (Fig 5.26). The I-V characteristic for the resistance states presented in Fig 5.25(a) is typically in an exponential control function. We define the different resistance states in this mode as E states, that is, E_1, E_2 … E_n. Fig 5.14 shows three such states (Phase I, II, and III). Modification of the IL properties under an electrical field results in different resistance states.

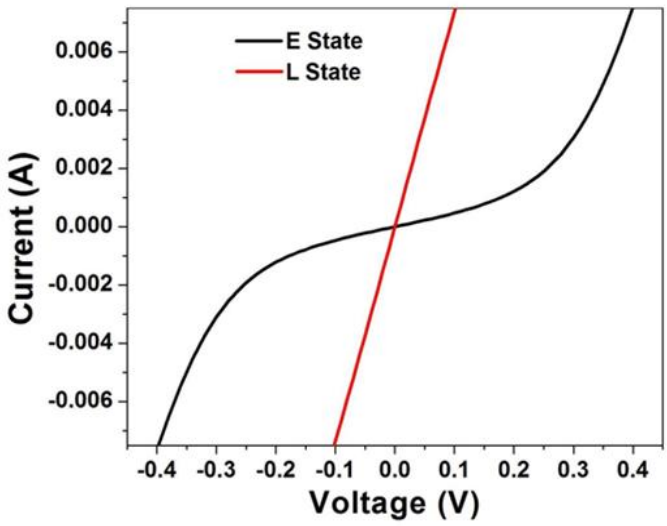

Figure 5.26: I-V characteristics of a device working at two different resistance states during an electroforming process.

Fig 5.25(b) shows conductive filaments are in direct contact with the TE. The number of filaments in conductance determines the current flow. Formation and rupture of filaments leads to different resistance states. The I-V characteristic in this mode is typically in a linear ohmic behavior, as shown in Figs 5.2, 5.3 and 5.4. We define the different resistance states in this mode as L states, that is, L_1, L_2 … L_n. Fig 5.4 shows that rupture of filaments under a negative bias will result into different resistance states. Migration of oxygen ions could result in a charge zone at the metal/oxide interface [20, 21]. The charge zone could be positive or negative. An additional potential (ΔV_{eff}) could be added to current flow, and change the I-V shape. The charge distribution, as well as the variation of the charge density at the interface region in an electrical sweeping process could lead to different characteristics. Instead of a linear behavior, a slightly sublinear behavior is also observed for the LRS in Figs 5.7, 5.20 and 5.23, which we attribute to the charge effect [43]. Typical examples of the interface charge effect are shown in Figs 3.11 and 3.13.

A single filament could have a high resistance. In comparison to a large number of filaments for conductance in the LRS state, much fewer filaments contribute to the current flow for the HRS state in Fig 5.8. At low voltage, current comes from a small number of filaments in the oxide. At higher voltage, defect involved space charge limited current from the bulk oxide contributes to the current flow and the I-V curves shifts from the linear characteristic.

Control of the external voltage could lead to the switching between the E state and the L state, through redox and oxidation reactions. We also fabricated Ni/TiO_2/Pt structural devices [44]. By controlling the electroforming processes, different I-V characteristics were observed, as shown in Fig 5.27. Fig 5.27(a) shows the transition of an L state to an E state, while Fig 5.27(b) shows the transition of an E state to an L state. The transition from an L state to another L state was shown in Fig 5.27(c). The strictly linear I-V characteristic under high current indicates that the temperature effect due to Joule heating in current flow might not be so significant in the process. Fig 5.27(d) shows the transition from an E state to another E state.

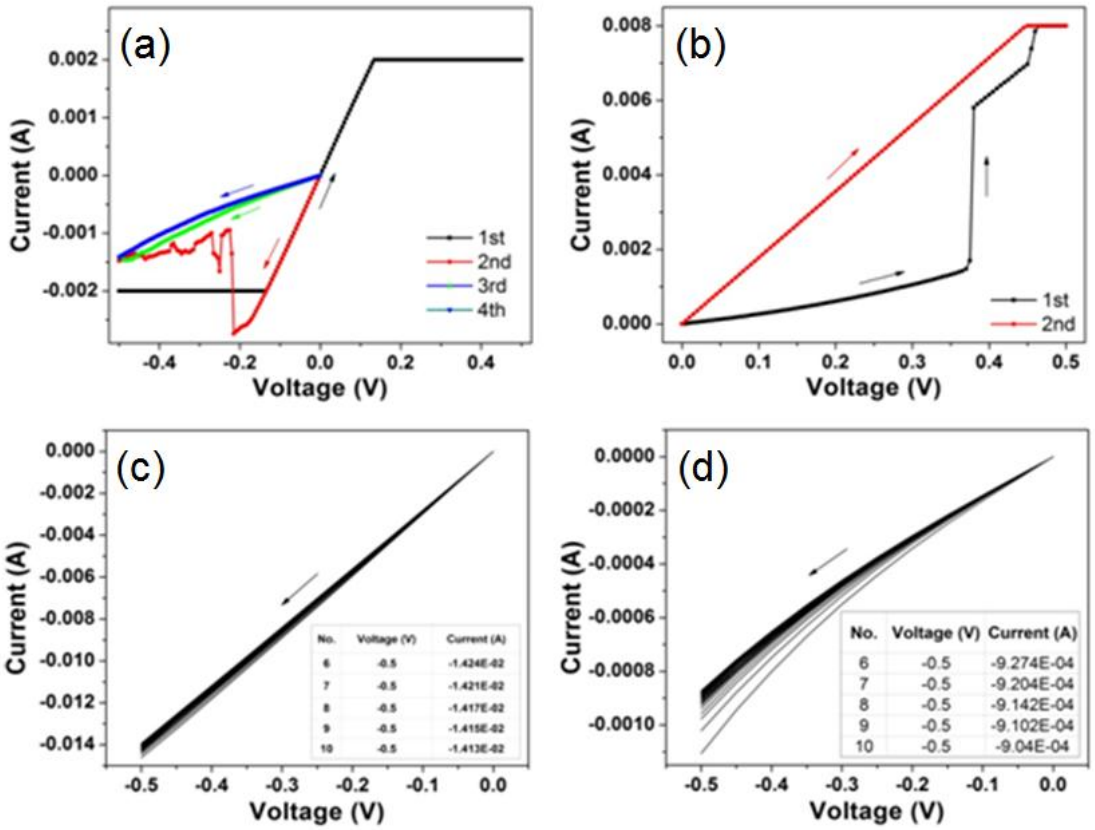

Figure 5.27: I-V curves of a Ni/TiO_2/Pt device. (a) 1st scan, 0 to 0.5 V; 2nd to 4th scans, 0 to -0.5 V. Switching from an L state to an E state occurs at the 2nd scan (after change the current compliance). (b) 1st and 2nd scans, 0 to 0.5 V. Switching from an E state occurs at the 1st scan. (c) 20 times continuous scans: 0 to -0.5 V. The resistance state shifts a higher L state after each scan. (d) 20 times continuous scans: 0 to -0.5 V. The resistance shifts to a higher E state after each scan.

5.7 Chapter summary

In this chapter, we studied the filamentary characteristics in TiO_2 thin films. High repeatable bipolar switching filamentary switching behavior was observed. An integrated model combining both filamentary and interfacial effects is further discussed. The filament-interface model is a summary and integration of the reported works by many other groups, and further supported by our experimental results. We expect this integrated model could be extended to other material systems.

The resistive switching effect is attributed to a reversible oxidation and redox process in the oxide. Charge trapping and detrapping assisted by electro-migration of

oxygen ions plays a key role such a process. CAFM studies shows that control of a local electric field could lead to repeatable transition between different resistance states. The FE measurements suggest electroforming of filaments in a large area with the absence of a top electrode. The good agreement between experimental results and theoretical modelling based on first-principles calculations provides a fundamental understanding of the unipolar switching behavior. We expect the ability to pattern high density of filaments in an oxide thin film to open up new opportunities in high density memory devices.

References

[1] R. Waser and M. Aono, "Nanoionics-based resistive switching memories," *Nat. Mater*. **6**, 833–840 (2007).

[2] A. Sawa, "Resistive switching in transition metal oxides," *Mater. Today* **11**, 28–36 (2008).

[3] R. Waser, R. Dittman, G. Staikov and K. Szot, "Redox-based resistive switching memories - nanoionic mechanisms, prospects, and challenges," *Adv. Mater*. **21**, 2632– 2663 (2009).

[4] Y. Hirose and H. Hirose, "Polarity-dependent memory switching and behavior of Ag dendrite in Ag-photodoped amorphous As_2S_3 films," *J. Appl. Phys.* **47**, 2767-2772 (1976).

[5] Q. Liu, S. B. Long, H. B. Lv, W. Wang, J. B. Niu, Z. J. Huo, J. N. Chen and M. Liu, "Controllable growth of nanoscale conductive filaments in solid-electrolyte based ReRAM by using a metal nanocrystal covered bottom electrode," *ACS Nano* **4**, 6162-6168 (2010).

[6] B. J. Cho, J. –M. Yun, S. H. Song, Y. S. Ji, D. –Y. Kim and T. H. Lee, "Direct observation of Ag filamentary paths in organic resistive memory devices," *Adv. Funct. Mater.* **21**, 3976–3981 (2011).

[7] Q. Liu, J. Sun, H. B. Lv, S. B. Long, K. B. Yin, N. Wan, Y. T. Li, L. T. Sun and M. Liu, "Real-time observation on dynamic growth/dissolution of conductive filaments in oxide-electrolyte-based ReRAM," *Adv. Mater.* **24**, 1844–1849 (2012).

[8] Y. Yang, P. Gao, S. Gaba, T. Chang, X. Pan and W. Lu, "Observation of conducting filament growth in nanoscale resistive memories," *Nat. Commun*. **3**, 732 (2012).

[9] G. –S. Park, X. –S. Li, D. –C. Kim, R. –J. Jung, M. –J. Lee and S. Seo, "Observation of electric-field induced Ni filament channels in polycrystalline NiO_x film," *Appl. Phys. Lett.* **91**, 222103 (2007).

[10] B. J. Choi, D. S. Jeong, S. K. Kim, C. Rohde, S. Choi, J. H. Oh, H. J. Kim, C. S. Hwang, K. Szot, R. Waser, B. Reichenberg and S. Tiedke, "Resistive switching mechanism of TiO_2 thin films grown by atomic-layer deposition," *J. Appl. Phys*. **98**, 033715 (2005).

[11] K. Fujiwara, T. Nemoto, M. J. Rozenberg, Y. Nakamura, and H.Takagi, "Resistance switching and formation of a conductive bridge in metal/binary oxide/metal structure for memory devices," *Jpn. J. Appl. Phys*. **47**, 6266-6271 (2008).

[12] R. Yasuhara, K. Fujiwara, K. Horiba, H. Kumigashira, M. Kotsugi, M. Oshima, and H. Takagi, "Inhomogeneous chemical states in resistance-switching devices with a planar-type Pt/CuO/Pt structure," *Appl. Phys. Lett*. **95**, 012110 (2009).

[13] D. H. Kwon, K. M. Kim, J. H. Jang, J. M. Jeon, M. H. Lee, G. H. Kim, X. S. Li, G. S. Park, B. Lee, S. Han, M. Kim and C. S. Hwang, "Atomic structure of conducting nanofilaments in TiO_2 resistive switching memory," *Nat. Nanotechnol*. **5**, 148-153 (2010).

[14] J. P. Strachan, M. D. Pickett, J. J. Yang, S. Aloni, A. L. D. Kilcoyne, G. Medeiros-Ribeiro and R. S. Williams, "Direct identification of the conducting channels in a functioning memristive device," *Adv. Mater*. **22**, 3573-3577 (2010).

[15] R. Müenstermann, T. Menke, R. Dittmann and R. Waser, "Coexistence of filamentary and homogeneous resistive switching in Fe-doped $SrTiO_3$ thin-film memristive devices*," Adv. Mater*. **22**, 4819-4822 (2010).

[16] J. Yao, L. Zhong, D. Natelson and J. M. Tour, "*In situ* imaging of the conducting filament in a silicon oxide resistive switch," *Sci. Rep*. **2**, 242 (2012).

[17] D. S. Jeong, H. Schroeder, U. Breuer, and R. Waser, "Characteristic electroforming behavior in Pt/TiO_2/Pt resistive switching cells depending on atmosphere," *J. Appl. Phys.* **104**, 123716 (2008).

[18] B. J. Choi, D. S. Jeong, S. K. Kim, C. Rohde, S. Choi, J. H. Oh, H. J. Kim, C. S. Hwang, K. Szot, R. Waser, B. Reichenberg and S. Tiedke, "Resistive switching mechanism of TiO_2 thin films grown by atomic-layer deposition," *J. Appl. Phys*. 98, 033715 (2005).

[19] R. Müenstermann, J. J. Yang, J. P. Strachan, G. Medeiros-Ribeiro, R. Dittmann and R. Waser, "Morphological and electrical changes in TiO_2 memristive devices induced by electroforming and switching," *Phys. Status Solidi RRL* **4**, 16-18 (2010).

[20] Y. M. Du, A. Kumar, H. Pan, K. Y. Zeng, S. J. Wang, P. Yang and A. T. S. Wee, "The resistive switching in TiO_2 films studies by conductive atomic force microscopy and Kelvin probe force microscopy." (Submitted)

[21] Y. M. Du, H. Pan, S. J. Wang, T. Wu, Y. P. Feng, J. S. Pan and A. T. S. Wee, "Symmetrical negative differential resistance behavior of a resistive switching device," *ACS Nano* **6**, 2517-2523 (2012). In comparison to that described in Ref. 21, the interface layer could also be a composition of $Al(Ti)O_x$.

[22] B. Weber, S. Mahapatra, H. Ryu, S. Lee, A. Fuhrer, T. C. G. Reusch, D. L. Thompson, W. C. T. Lee, G. Klimeck, L. C. L. Hollenberg and M. Y. Simmons, "Ohm's law survives to the atomic scale," *Science* **335**, 64-67 (2012).

[23] C. Acha, M. Monteverde, M. Nunez-Regueiro, A. Kuhn and M. A. A. Franco, "Electrical resistivity of the Ti_4O_7 Magnéli phase under high pressure," *Eur. Phys. J. B* **34**, 421-428 (2003).

[24] L. F. Liu, H. Tang, Y. Wang, W. Wang, D. Y. Tian, X. Y. Liu, X. Zhang, R. Q. Han and J. F. Kang, " Reversible resistive switching of Gd-doped TiO_2 thin films for nonvolatile memory applications", *8th Int. Conf. on Solid-state and Integrated Circuit Tech.* (2006).

[25] Y. C. Yang, F. Pan, F. Zeng and M. Liu, "Switching mechanism transition induced by annealing treatment in nonvolatile Cu/ZnO/Cu/ZnO/Pt resistive memory: from carrier trapping/detrapping to electrochemical metallization," *J. Appl. Phys.* **106**, 123705 (2009).

[26] M. A. Lampert and P. Mark, *Current injection in solids*, New York (1970**)**.

[27] A. Moradpour, O. Schneegans, S. Franger, A. Revcolevschi, R. Salot, P. Auban-Senzier, C. Pasquier, E. Svoukis, J. Giapintzakis, O. Dragos, *et al*. "Resistive switching phenomena in Li_xCoO_2 thin films," *Adv. Mater*. **23**, 4141-4145 (2009).

[28] O. Schneegans, A. Moradpour, L. Boyer and D. Ballutaud, "Nanosized electrochemical cells operated by AFM conducting probes," *J. Phys. Chem. B* **108**, 9882-9887 (2004).

[29] J. G. Simmons, "Generalized formula for electric tunnel effect between similar electrodes separated by a thin insulating film," *J. Appl. Phys.* **34**, 1793–1803 (1963).

[30] R. E. Holmlin, R. Haag, M. L. Chabinyc, R. F. Ismagilov, A. E. Cohen, A. Terfort, M. A. Rampi and G. M. Whitesides, "Electron transport through thin organic films in metal-insulator-metal junctions based on self-assembled monolayers," *J. Am. Chem. Soc*. **123**, 5075–5085 (2001).

[31] Definition of the fitting parameter varies [30]. It might be caused by a nonrectangular barrier shape, the effective mass of the electron tunneling through the barrier, or a combination of both.

[32] H. D. Lee, B. Magyari-Köpe and Y. Nishi, "Model of metallic filament formation and rupture in NiO for unipolar switching," *Phys. Rev. B* **81**, 193202 (2010).

[33] S. –G. Park, B. Magyari-Köpe and Y. Nishi, "Impact of oxygen vacancy ordering on the formation of a conductive filament in TiO_2 for resistive switching memory," *IEEE Electron Device Lett*. **32**, 197-199 (2011).

[34] G. Kresse and J. Furthmuller, "Efficiency of *ab-initio* total energy calculations for metals and semiconductors using a plane-wave basis set," *J. Comput. Mater. Sci*. **6,** 15-50 (1996).

[35] K. M. Kim, B. J. Choi, S. Choi, D. S. Jeong and C. S. Hwang, "Resistive switching in Pt/Al_2O_3/TiO_2/Ru stacked structures," *Electrochem. Solid-State Lett. **9**,* G343-G346 (2006).

[36] U. Russo, D. Ielmini, C. Cagli and A. L. Lacaita, "Self-accelerated thermal dissolution model for reset programming in unipolar resistive-switching memory (RRAM) devices," *IEEE Trans. Electron Devices* **56**, 193–200 (2009).

[37] D. Ielmini, F. Nardi and C. Cagli, "Physical models of size-dependent nanofilament formation and rupture in NiO resistive switching memories," *Nanotechnology* **22**, 254022 (2011).

[38] S. H. Chang, S. C. Chae, S. B. Lee, C. Liu, T. W. Noh, J. S. Lee, B. Kahng, J. H. Jang, M. Y. Kim, D. -W. Kim and C. U. Jung, "Effects of heat dissipation on unipolar resistance switching in Pt/NiO/Pt capacitors," *Appl. Phys. Lett*. **92**, 183507 (2008).

[39] J. A. Campa, M. Velez, C. Cascales, E. P. Gutierrez Puebla, M. A. Monge, "Cystal growth of superconducting $LiTi_2O_4$," *J. Crystal Growth* **142**, 87-92 (1994).

[40] L. Benco, J.-L. Barras, and C. A. Daul, "Theoretical study of the intercalation of Li into TiO_2 structures," *Inorg. Chem*.38, 20-28 (1999).

[41] M. H. Lee, K. M. Kim, G. H. Kim, J. Y. Seok, S. J. Song, J. H. Yoon and C. S. Hwang, "Study on the electrical conduction mechanism of bipolar resistive switching TiO_2 thin films using impedance spectroscopy," *Appl. Phys. Lett.* **96**, 152909 (2010).

[42] D. S. Jeong, H. Schroeder and R. Waser, "Coexistence of bipolar and unipolar resistive switching behaviors in a Pt/TiO_2/Pt stack," *Electrochem. Solid-State Lett.* **10**, G51-G53 (2007).

[43] An alternative to explain the sub-linear (bending up) I-V characteristic is the Joule heating effect in current flow. In contrast, the strictly linear I-V characteristic is observed at even high current (e.g. Figs 5.2 to 5.4, Fig 5.27(c)), indicating Joule heating effect might not be so significant in the devices.

[44] For the Ni/TiO_2/Pt structure devices, the resistive switching could also come from a Ni(Ti)O_x layer formed at the interface, for which different threshold voltages were observed during the electroforming processes.

Chapter 6

Conclusion

6.1 Contributions

In this thesis, we have studied TiO_2 based resistive switching devices. The resistive switching mechanisms were investigated through both experimental and theoretical methods. The main experimental methods involved were sputtering,

current-voltage measurements, scanning probe/atomic force microscopy and photoelectron microscopy. The first-principles study using density functional theory (DFT) was performed for theoretical modeling.

Firstly, TiO_2 thin films with enhanced conductivity were investigated by conductive atomic force microscopy (CAFM) and Kelvin probe force microscopy (KPFM). The high density nano-filaments were observed during the CAFM measurements. Surface modifications using the AFM tip change the overall film conductivity. By applying a local electrical field, the as-prepared TiO_2 thin films can be modulated into higher and lower resistance states. A combined study using CAFM and KPFM shows that the resistive switching mechanism is due to charge injection and release assisted by electro-migration of oxygen ions under an electrical field.

Secondly, the symmetrical negative differential resistance (NDR) behavior with high repeatability in a resistive switching device was observed and reported. Through first-principles modeling, a structure composing of oxygen interstitial is proposed. A good agreement between experimental results and theoretical modeling has been achieved. With conductive filaments in the bulk oxide, a thin interfacial layer is attributed as the origin of the observed switching behavior. In the electron tunneling regime, a new model based on charge trapping and detrapping is proposed for the observed resistive switching phenomenon. By introducing specific defects in a very thin insulating layer, the results and the mechanisms demonstrated here could be extended to other systems approaching molecular dimensions for device applications.

With oxygen as the active source, a new understanding of the Simmons and Verderber (SV) mechanism has been achieved. This could be the first time using oxygen molecule for charge storage in the SV mechanism. By introducing conductive filaments in the bulk oxide, the SV mechanism is further extended to a new model

with a thin interfacial layer at the metal/oxide interface. Known for its assumptions in the mechanism description, the SV mechanism is rather a hypothesis due to the lack of direct evidences. The measurement of the band gap state using the photoelectron microscopy, and the good agreement to the theoretical modeling provide a support to the mechanism.

Finally, we investigated the filamentary characteristics in TiO_2 thin films. We summarized the various current-voltage characteristics in the measurements, including both bipolar and unipolar resistive switching behaviors. Multiple filamentary current-voltage characteristics were observed and further confirmed by the CAFM experiments. This is a contrast to the popular single filament model for resistive switching. The high repeatable filamentary bipolar switching behavior presents an example for multiple filamentary switching. Instead of using a high electrical breakdown process for filament electroforming, the result shows that high density filaments with good uniformity could be achieved at much smaller voltages. The further field emission experiments suggest a method of electroforming filaments in a large area. The ability to pattern high density nano-filaments shows a good potential for RRAM applications.

Instead of treating the filamentary and interfacial effects separately, an integrated model combining both effects is proposed. Based on the various current-voltage characteristics, we summarized a filament-interface model. The resistive switching is attributed to a reversible process involving oxidation and redox processes. The first-principles modeling of metallic atom chains in TiO_2 provides a fundamental understanding of the ON state mechanism. It shows that the role of vacancy ordering leads to the formation of conductive filaments in the bulk oxide. The theoretical modeling complies well with the experimental results. Charge trapping and

detrapping assisted by electro-migration of oxygen ions leads to different resistance states.

6.2 Future works

The CAFM and KPFM experiments were performed at atmospheric condition. The existence of unwanted contamination on the sample surface may block the current path and affect the electric field applied. A contaminated tip would also affect the conductivity measurement. Besides oxygen, the decomposition of water molecules and carbon dioxide in the atmosphere could also affect the measurements. In vacuum, a much higher lateral resolution could be achieved. Therefore the study of the resistive switching in a vacuum condition would give more information of the mechanisms involved. Furthermore, a temperature dependent measurement using both CAFM and KPFM is also helpful in providing the dynamics in resistive switching.

All theoretical calculations based on DFT were performed based on periodic supercell structures, which represent ideal situations compared with the much more complicated situations in real applications. Besides the theoretical modeling of conductive filaments, the experimental works such as HRTEM (combined with EELS), XAFS and Femtosecond laser spectroscopy measurements will be implemented in the future works, for more details of the conductive filament microstructure, the oxygen vacancy ordering and the charge states involved. Furthermore, all the calculations were performed at 0 K. The temperature effect is important for RRAM based device applications. Temperature could significantly affect the dynamics of oxygen ions. Therefore future theoretical works will also consider the temperature effects.

In this study, we have studied the various current-voltage characteristics of TiO_2 thin films. Due to the limitation of the used techniques, the fabricated device has a rather large size (~ 100 μm). For integrated device applications, it is necessary to fabricate devices in the range of tens of nanometers. Thus more works on functionalized integrated devices in a large area will be involved in the future works. Besides TiO_2, other materials such as ZnO, Ta_2O_5, NiO, SiO, ZrO_2, $SrTiO_3$, as well as stacked oxides structures are also reported to have good performances in resistive switching. Therefore, a comparative study using different materials would also be an interesting subject.